PULSE COMPRESSION AND DISPERSION CONTROL IN ULTRAFAST OPTICS

A Dissertation
Presented to
The Academic Faculty

by

Vikrant Chauhan

In Partial Fulfillment
of the Requirements for the Degree
Doctor of Philosophy in the
School of Physics

Georgia Institute of Technology
December 2010

PULSE COMPRESSION AND DISPERSION CONTROL IN ULTRAFAST OPTICS

Approved by:

Dr. Rick P. Trebino, Advisor
School of Physics
Georgia Institute of Technology

Dr. John A. Buck
School of Electrical Engineering and
Computer science
Georgia Institute of Technology

Dr. Jennifer Curtis
School of Physics
Georgia Institute of Technology

Dr. Chandra Raman
School of Physics
Georgia Institute of Technology

Dr. Jiang Zhigang
School of Physics
Georgia Institute of Technology

To my mother Mrs. Sadhana Singh and my father Dr. Veer Singh

ACKNOWLEDGEMENTS

I would like to thank my parents first, as without their love, care, and constant guidance I wouldn't be here. I am greatly thankful to my adviser, Rick, for giving me challenging and interesting projects to work on. I also thank him for his encouragement, helpful advice, and for teaching me all of the ultrafast optics that I know today. It was a great pleasure to work and interact with the former graduate students of our group, who were around at the time when I started: Pablo, Neeraj, Lina, Pam, Xuan, and Dongjoo, and I am very thankful to them for sharing their experiences as graduate students, invaluable experimental tips, and their guidance. I am also very thankful to my colleagues. I couldn't ask for better group members, collaborators and friends as Peter, Jake, and Pam. I am thankful to Pam and Jake for all the helpful discussions, and collaborations in all the experiments related to spectral interferometry. I am especially thankful to Peter for his precious contributions to the double blind PG FROG experiment and for reviewing my thesis several times. I am also thankful to Linda, and the staff at the School of Physics for their assistance in all the financial and general matters.

Finally, there are several people outside of our research group who have helped a great deal in my thesis project. I am thankful to Steve Kane and Jeff Squier for providing us with a grism for experiments and their assistance. I am also thankful to Ed for being a wonderful mentor and being very inspiring all throughout the period of our collaboration with LM. I would also like to thank Del for his contribution in the work done here and ensuring the funding for my research.

TABLE OF CONTENTS

LIST OF FIGURES

LIST OF SYMBOLS

ω	Angular frequency
λ	Wavelength
φ	Spectral phase
τ	Temporal delay
ψ_i	Angle of incidence from surface
ψ_d	Angle of diffraction from surface
Φ	Temporal phase
ρ	Rho parameters
θ, β	Angle of incidence from surface normal
ϕ, γ	Angle of refraction from surface normal
$\Delta\varphi$	Spectral phase difference
n	Refractive index
c	Speed of light
t	time

LIST OF ABBREVIATIONS

CPA	Chirped pulse amplification
SEA TADPOLE	Spatially encoded arrangement for temporal analysis by dispersing a pair of light E-fields
MUD TADPOLE	Multiple Delay for temporal analysis by dispersing a pair of light E-fields
GRENOUILLE	Grating eliminated no-nonsense observation of ultrafast incident laser light E-field
CVBG	Chirped Volume Bragg Grating
SC	Super continuum
FWHM	Full width at half maximum
FWM	Four wave-mixing
FROG	Frequency resolved optical gating
SPIDER	Spectral phase interferometry for direct electric field reconstruction
PG	Polarization gating
XFROG	Cross-correlation frequency resolved optical gating
CCD	Charge coupled device
MSE	Method of single expression

SUMMARY

In this thesis, we introduced novel pulse compressors that are easy to align and which also compensate for higher order dispersion terms. They use a single dispersive element or a combination of dispersive elements in single-element-geometry. They solve the problem of extra-cavity pulse compression, and provide control of the pulse width in almost all of the experiments performed using ultrashort pulses. We performed full spatiotemporal characterization of these compressors and demonstrated their performance. We also introduce a theoretical simulation which is based on a matrix based formalism. It models the full spatiotemporal characteristics of any dispersion control system. We also developed a simple equation, in its most general form, to relate the total dispersion and magnification introduced by an arbitrary sequence of dispersive devices. Pulse compressor characterization was done using interferometric measurements in the experiments presented in this work, but we also developed a method to measure pulses that uses polarization gating FROG for measuring two unknown pulses. In the last part, we briefly discuss the designing of a high energy chirped pulse amplification system.

CHAPTER 1

INTRODUCTION

1.1 Ultrashort pulses and applications

Ultrashort pulses are bursts of electromagnetic radiation which are very short in duration. A typical ultrashort pulse is 10 to 100 fs (1fs = 10^{-15} seconds) in temporal width. The shortest ultrashort pulses are several attoseconds (1 as = 10^{-18} seconds) long, and the longest can be up to a few picoseconds (1ps = 10^{-12} seconds). Owing to their short temporal extent, these pulses, must necessarily have large spectral bandwidths. This can be easily understood using Fourier transform relation between time and frequency domains: creating a short pulse in time requires a coherent superposition of a broad range of frequencies. This bandwidth also depends on the carrier frequency of the pulse envelope. For a given pulse width, the required bandwidth decreases with increasing the carrier frequency. Due to the short durations of these pulses, it is possible to achieve high peak intensities ($\sim 10^{12} W/cm^2$) for relatively low average powers, and study phenomena that occur at very short time scales.

Due to their high peak intensities, these pulses find some interesting applications. One such application is micromachining[1, 2]. The time scale on which material can be ablated using femtosecond pulses is so short that only a small amount of energy is dissipated as heat[3, 4]. This helps overcome the difficulties posed by thermally induced stress that causes cracks and fissures to form, which plague almost every other machining technique. Ultrashort pulses are also used in coherent control experiments in which the

course of a chemical reaction can be changed by shining shaped ultrashort pulses [5-7]on the reactants[8, 9]. This allows directed cleaving of chemical bonds in molecules and thus controls the outcome of a chemical reaction[10]. Medical imaging has had significant recent advancements such as multi-photon imaging[11, 12], CARS (Coherent Anti-Stokes Raman Scattering) microscopy[13] and OCT (Optical Coherence Tomography)[14-16]. Multi-photon microscopy uses detection of second or third harmonic signals generated inside bio-tissue from the pulses centered at longer wavelengths. This allows greater probing depths in the tissue and higher imaging resolution. The signal is generated only at the beam focus and the probe wavelengths, which are long, are scattered less in the tissue, thus, allowing deeper positioning of the focal spot. The whole tissue volume is scanned by the focal spot and the resulting higher harmonic photons are scattered in the tissue and emerge from the surface of the sample where they can be detected, and thus a multilayer topographical image of the biological sample can be created. Another promising application of such pulses is ultrafast telecommunication and all-optical switches[17], which are being widely researched. Ultrashort pulses are also used to generate attosecond pulses or soft x-rays[18], which have helped probe faster time-scale physical phenomena, and to create and study other exotic nonlinear optical effects such as optical beam filamentation[19, 20]. Short laser pulses not only continue to prove important in the advancement of various technologies, but they also provide an excellent tool for studying the physics of the processes occurring on very fast time scales, and there are many more applications of ultrashort pulses than listed here. Therefore, the study and development of pulse measurement techniques, and the methods to manipulate pulse properties, such as pulse compression, pulse shaping,

and dispersion control is indispensable for the improvement of most of the desired applications.

1.2 Generation of Ultrashort pulses

Laser sources can be broadly classified into two types based on their mode of operation: pulsed-lasers, and continuous wave (CW) emitting lasers. Practically, such lasers can be realized in several different systems, such as gas lasers (He-Ne or CO_2), semiconductor lasers (Nd:YAG, Ti:Sapphire), or dye lasers (such as Rhodamine or Malachite green solutions). CW lasers have relatively narrow spectral widths. Generation of laser pulses of temporal widths as low as 10 nanoseconds to 100 nanoseconds can be achieved by using a fast shutter at the output of a CW-laser, e.g. by placing a pockels cell and a linear polarizer in the cavity. A pockels cell acts as a waveplate when the correct voltage is applied across it, and upon passing through it the polarization of light changes from ‘s’ to ‘p’ and it is rejected out from the cavity by the linear polarizer. This method is known as active switching and its speed is limited by the attainable speeds in electronic switching.

A different mechanism for generating pulses is by using a saturable absorber in a cavity. This offers faster switching rates and the resultant pulses are as short as 500 femtoseconds to a few picoseconds. Usually a dye is used as the saturable absorber which absorbs light of low intensity but becomes transparent at intensities that are above a certain saturation threshold. Therefore, for a pulse in the cavity the leading and the trailing edge of the pulse suffer absorptive losses and are suppressed whereas the high intensity region close to the pulse’s center gains more and more strength. This process

shortens the pulse and increases the peak intensity. This mechanism of switching is called passive switching or passive modelocking [21, 22].

Modern lasers use Ti:Sapphire as the laser gain medium. This system can generate pulses that can be as short as a few femtoseconds or few optical cycles in duration to several picoseconds[22]. In these lasers, the Ti:Sapphire crystal is optically pumped using a solid state diode laser, (such as a 5 Watts Nd:YLF Coherent Verdi which pumps the Ti:Sapphire crystal in our lab), and the Ti:S laser cavity can lase over a broad wavelength range from 650nm to 1100nm. The Ti:S material lases in a CW mode, but the cavity can be made to preferentially lase in a pulsed mode. In the cavity, the CW beam and the pulsed beam compete for the energy in the gain medium. To achieve mode-locking (or to generate pulses), the phenomenon of Kerr-lensing is used[23]. In Kerr-lensing, high energy laser beams undergo self-focusing when going through a material due to the nonlinear refractive index change brought about by optical Kerr effect. For a Gaussian beam, the induced refractive index varies across its cross-section and is higher at the beam's center than the edges. The crystal acts as a waveguide for both beams due to thermal lensing (induced by the pump), but for the pulsed beam, the beam width gets further reduced due to Kerr-lensing. This causes the beam spot to be smaller than that of the CW beam on the flat mirrors at the ends of the cavity. In the earlier systems, an aperture was placed before the end mirrors to cut-off the CW beam and favor the pulsed operation. But in the later systems, a soft aperture is used, in which the pump beam is focused to a small beam width in the crystal using a telescope in the cavity and this increases the overlap of the pump with the smaller pulsed beam, which thus experiences much greater gain than the CW beam.

The length of the crystal, for most part, is limited by the group delay dispersion (GDD) added to the pulse. The GDD added by the crystal can be compensated by a prism pair compressor placed inside the cavity or by using chirped mirrors. The repetition rate of the pulses in the pulse train is usually ~90 MHz, depending on the cavity round trip time. The energy per pulse from the laser that we have used in part this work is around ~9 nanojoules per pulse, which is sufficient for exciting a nonlinear process by focusing the beam. Other parts of this work used higher pulse energy, where the pulses from a similar oscillator are used to seed the regenerative amplifier cavity which outputs 3 mJ pulses at a kilohertz repetition rate. The amplified pulses were used in the experiment with PG double blind FROG which uses third order nonlinearity for optical gating, and thus requires high pulse energy.

1.3 Ultrashort pulse measurement

There are several techniques available for the measurement of ultrashort pulses. The complete measurement of the temporal profile of the ultrashort pulses requires a complete knowledge of the pulse intensity, $I(t)$, and phase, $\Phi(t)$. The measurement of intensity and phase is not straight forward, as the temporal waveform cannot be detected even with the use of high bandwidth oscilloscopes. As even the fastest oscilloscopes available today have temporal responses which are tens of thousands time longer than the durations of ultrashort pulses, and hence only the indirect methods, some of which are discussed below, are the ones that can be used.

Pulse measurement can be done alternatively in the spectral domain, i.e. by measuring the spectrum $S(\omega)$, and the spectral phase $\varphi(\omega)$, because the field in the frequency domain is uniquely related to the field in time domain by Fourier transforms.

Pulse measurement, such as spectral interferometry and its several variations, are the linear methods i.e. they do not employ any nonlinear interactions to generate signal. The advantages of using interferometric methods are their high sensitivity, which allows the measurement of very weak pulses (10^{-21} joules ≈ few zeptojoules per pulse), and measuring complex pulses. Spectral interferometry always requires a pre-characterized reference pulse, which is a problem in certain applications. Self-referential techniques require high pulse energies as they use nonlinear interactions to generate the signal. Two basic examples of such techniques are FROG (frequency resolved optical gating), which is a time frequency domain measurement, and SPIDER (Spectral phase interferometry for direct electric field reconstruction).

1.3.1 Frequency Resolved Optical Gating

A FROG signal is a spectrogram also called a FROG trace. Generation of a FROG trace requires spectrally resolving the time gated nonlinear signal generated by the interaction between the same (for self-referenced FROG methods) or different (for methods requiring a reference pulse) pulses in a nonlinear medium, and recording the nonlinear signal on a CCD array. Using a two dimensional CCD array the spectrograms can be recorded on a single shot basis by crossing two large beams (3-5mm beam size) in the nonlinear medium and spectrally resolving the signal in the orthogonal dimension. Retrieving the pulse information from a FROG trace requires the use of a retrieval algorithm. This algorithm starts with a random guess for the pulse electric field and generates a FROG trace from that guess. Next, iteratively using the generalized projection algorithm, the initial field is improved at each step towards minimization of the difference between the measured FROG trace and the reconstructed trace generated

from the current guess. The algorithm returns the final results for the pulse electric-field when the measured and the reconstructed traces difference reaches a minimum.

The quantity that corresponds to the difference is called the G-error and is minimized in the retrieval process. This technique is founded to be very reliable and the convergence can be always achieved for simple to slightly complex pulses, unless there is systematic error present in the measured FROG trace which would result in an unphysical trace and no or poor convergence is achieved. In the cases of extremely complex pulses, sometimes, the FROG algorithm fails to converge.

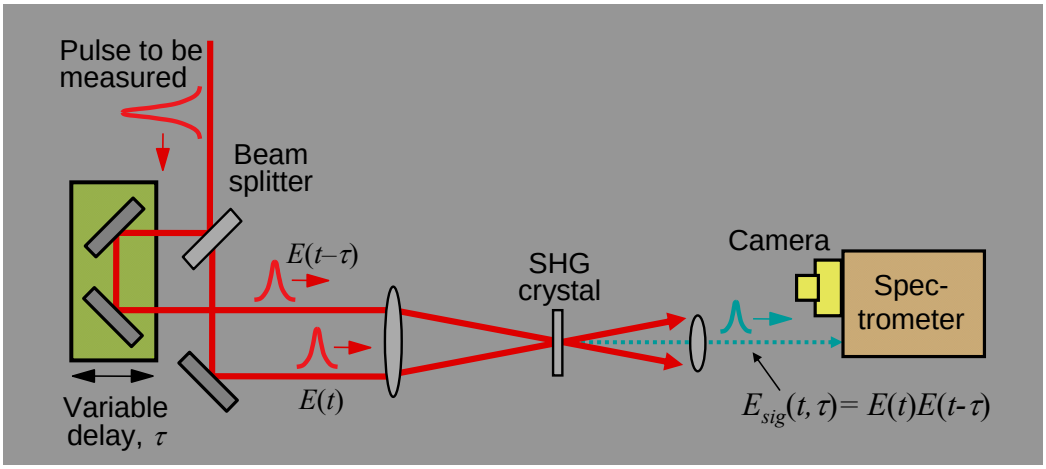

Fig. 1.1: Second harmonic generation FROG (fig. borrowed from Ultrafast Optics lectures).

A FROG measurement can be realized in two different geometries - single shot or multi-shot - and the signal can be generated using a few different nonlinearities e.g. second harmonic generation, sum and difference frequency generation, polarization gating, self-diffraction and transient grating, et cetera. The most sensitive version of FROG is second harmonic generation FROG[24]. SHG FROG is basically spectrally resolved autocorrelation.

SHG FROG has a highly simplified version called GRENOUILLE[25] which uses a Fresnel bi-prism to cross a magnified beam with itself in a thick crystal. A thick crystal only permits a narrow phase-matching bandwidth in a given direction therefore the second harmonic signal generated in the crystal is spectrally resolved by the crystal itself. In all the experiments discussed in this thesis, we used GRENOUILLE to characterize the input pulse whenever it was necessary. The figure below shows the working principle of a GRENOUILLE.

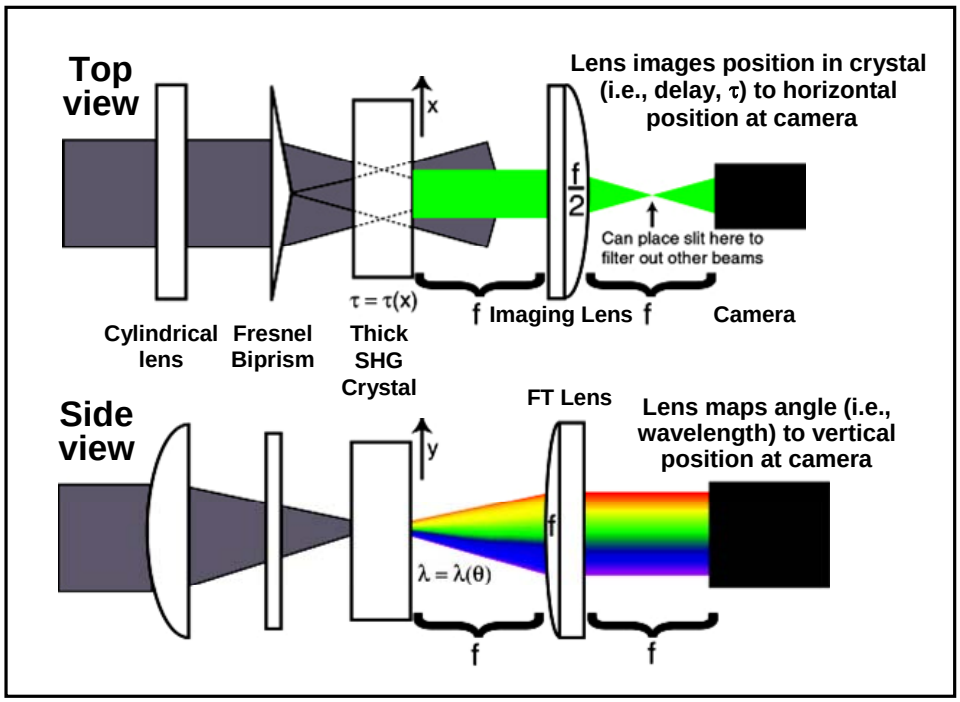

Fig. 1.2: Schematic of GRENOUILLE. Top view shows the back face of the crystal being imaged onto the camera, to map delay to position on the camera. Side view shows the focusing lens that maps the colors in the angularly dispersed signal to position on the vertical axis of the camera (fig. borrowed from Ultrafast Optics lectures).

Although, SHG FROG has several advantages, it also has some trivial ambiguities, such as direction of time. The phase matching requirement for generating second harmonic signal presents a limit to the spectral bandwidth of the pulse that can be measured on a single shot basis. Polarization gating FROG[26], on the other hand, uses a

third order nonlinearity (Kerr effect) and is automatically phase matched for all frequencies. In the last part of this thesis, we discuss the development of a single shot polarization gating 'double blind FROG' with which we can measure two unknown pulses simultaneously by using two FROG traces.

1.3.2 Pulse measurement using interferometry

Spectral interferometry deduces the spectral phase of an ultrashort pulse by combining it interferometrically with a reference pulse in a spectrometer. In spectral interferometry, the unknown and the reference beam are made collinear and sent into a spectrometer. The spectrometer, with sufficiently high resolution, records the spectral fringes due to the interference of the reference and the unknown. The fringe spacing of the recorded spectrum contains the phase-difference information as shown in the two equations below, where $E_{unk}(\omega)$ and $E_{ref}(\omega)$ are the phasors representing the *unknown* and the *reference* complex fields in frequency domain, and are delayed by time τ.

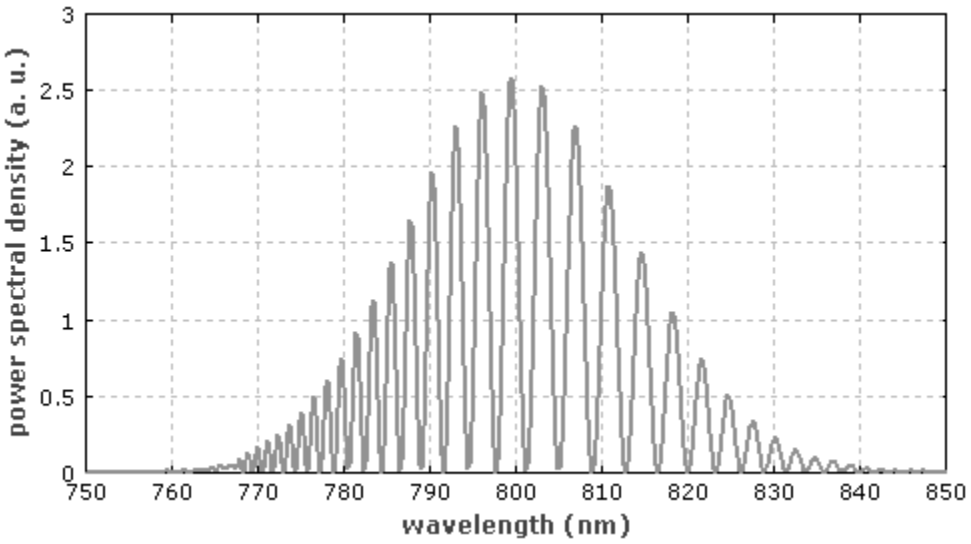

Fig 1.3: Shows the spectrum of two 50 fs femtoseconds pulses delayed by 500fs.

$$S(\omega)=\left|\left|E_{unk}(\omega)\right|e^{i\varphi_{unk}(\omega)}+\left|E_{ref}(\omega)\right|e^{i\varphi_{ref}(\omega)}\,\mathrm{e}^{-i\omega\tau}\right|^2 \tag{1.1}$$

The oscillating term has the phase $\Delta\varphi(\omega)$ which is given by:

$$\Delta\varphi(\omega)=\varphi_{unk}(\omega)-\varphi_{ref}(\omega)+\omega\tau \tag{1.2}$$

There are a few different methods that can be used to extract the phase difference from the measured spectrum of the interferogram. The most commonly used method is the Fourier transform spectral interferometry algorithm (FTSI)[27], in which the measured spectrum is Fourier transformed to time domain[28]. The Fourier transform thus obtained has a peak corresponding to the background intensity and two side bands which correspond to the cross term and its complex conjugate. Either of the side bands can be cropped and zero shifted and then Fourier transformed back to the frequency domain. After dividing out the reference spectrum, both the spectrum and the spectral phase w.r.t. the reference pulse can be obtained.

The alignment is difficult in SI because the two beams have to be exactly collinear. Also, this technique filters in time domain, which prevents us from using the full spectral resolution available in the spectrometer. However, there are variations of SI which get around these issues.

Crossed beam spectral interferometry uses a two dimensional CCD array and records the spatial fringes obtained by crossing two large beams spatially in the dimension orthogonal to the wavelength axis of the spectrometer[29]. It requires the pulses to be at zero delay in order to see the spatial fringes. It uses the full spectral resolution available in the spectrometer by using the second dimension of the camera and

filtering the signal in k-space. SEA TADPOLE[30] is a more useful variation of crossed-beam SI because the unknown and the reference pulse are coupled in to two equal length fibers before a collimating lens, which produce spatially uniform, well-collimated beams that interfere in the spectrometer to generate the interferogram. The use of fibers helps in mode-matching, ease-of-alignment, and reduction of noise that is caused due to spatial deformities in the beams. For the purpose of characterizing the pulse compressors designed in chapters 3 and 4, we used SEA TADPOLE as the pulse measurement technique. The technique of SEA TADPOLE has been extended upon in MUD TADPOLE[31] which provides several orders of magnitude improvement in the achievable spectral resolution in a given spectrometer.

1.3.3 Spectral phase interferometry for direct electric-field reconstruction (SPIDER)

This technique uses spectral–shear interferometry for measuring ultrashort pulses. The pulse to be measured is split into two replicas. One of the replicas is then chirped using a stretcher and the other replica is passed through a Michelson interferometer to produce a double pulse[32]. Thus, each arm of the SPIDER setup has a double pulse and a chirped pulse derived from the original input, which are now mixed in a nonlinear crystal to generate the sum-frequency signal. This signal is detected using a spectrometer and the phase information can be retrieved from the spectral fringes. The advantage of this technique is that the retrieval algorithm uses direct inversion, therefore, is quicker than the iterative methods. However, SPIDER measurement can be experimentally challenging, and the errors in calibration can potentially introduce large errors in the measurement[33, 34].

1.4 *Ultrashort pulses and dispersion control*

Ultrashort pulses generally have large bandwidths, typically around ~50nm, and because different colors travel at different speeds in a dispersive medium, these pulses tend to spread out in time. The stretching of a pulse causes its peak intensity to decrease, which is undesirable in several applications of such pulses. In this section, we talk about certain dispersion control (or pulse compression) methods and their working principles. The electric field of an ultrashort pulse can be completely described in time by specifying its intensity, $I(t)$, and phase, $\phi(t)$, as a function of time.

$$E(t) = \sqrt{I(t)}\exp\{-i\Phi(t)\} \tag{1.3}$$

This is equivalent to the pulse electric field in the frequency domain given by the spectrum, $S(\omega-\omega_0)$, and the spectral phase $\varphi(\omega-\omega_0)$, where ω_0 is the carrier frequency.

$$\tilde{E}(\omega-\omega_0) = \sqrt{S(\omega-\omega_0)}\exp\{-i\varphi(\omega-\omega_0)\} \tag{1.4}$$

When the spectral phase is constant for all frequencies, the pulse width is the minimum permitted by the Fourier transform relation, for the given spectral bandwidth. A nonzero spectral phase causes the pulse to spread in time. A Taylor series expansion of the spectral phase about the center frequency gives the first few important terms that are used as pulse width control parameters.

$$\varphi(\omega-\omega_0)=\varphi_0+\varphi_1(\omega-\omega_0)+\frac{\varphi_2}{2!}(\omega-\omega_0)^2+\frac{\varphi_3}{3!}(\omega-\omega_0)^3+\frac{\varphi_4}{4!}(\omega-\omega_0)^4+\cdots \tag{1.5}$$

The coefficient of the linear term in the above expansion is the group delay, which refers to the arrival time of the colors. The quadratic term or the quadratic spectral phase physically means that the delay varies linearly with frequency, and this is also known as the linear chirp. The coefficient of the quadratic term corresponds to the group delay dispersion (GDD). GDD is positive for all dispersive materials in the normal dispersion regime. To cancel the effect, negative GDD must be added through some means. In fiber optics, dispersion compensating fibers (DCF) can add negative GDD as the fiber material is designed to have anomalous dispersion for the operating wavelength.

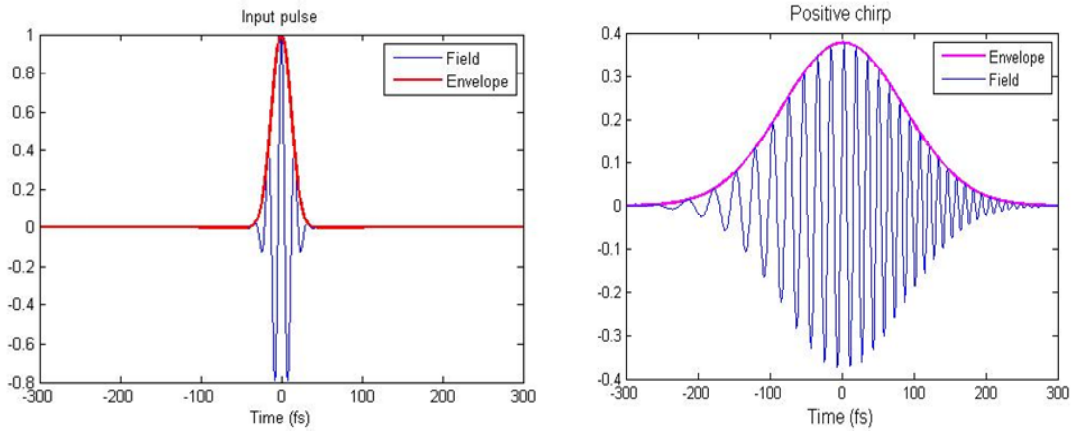

Fig. 1.4: The pulse width increases due to the quadratic phase or the linear chirp. The increase in duration causes the peak intensity to drop.

The third order phase term corresponds to the third order dispersion (TOD) and has an additional interesting effect on the pulses besides stretching it. Due to this term the redder and the bluer colors both arrive either before or after the green color. These colors beat together to cause ringing of the intensity envelope of the pulse, closer to the edges of the pulse. The algebraic sign of the TOD determines if the ringing occurs on the leading edge or the trailing edge of the pulse. Materials add positive TOD, and to compensate for it negative TOD should be added by a pulse compressor.

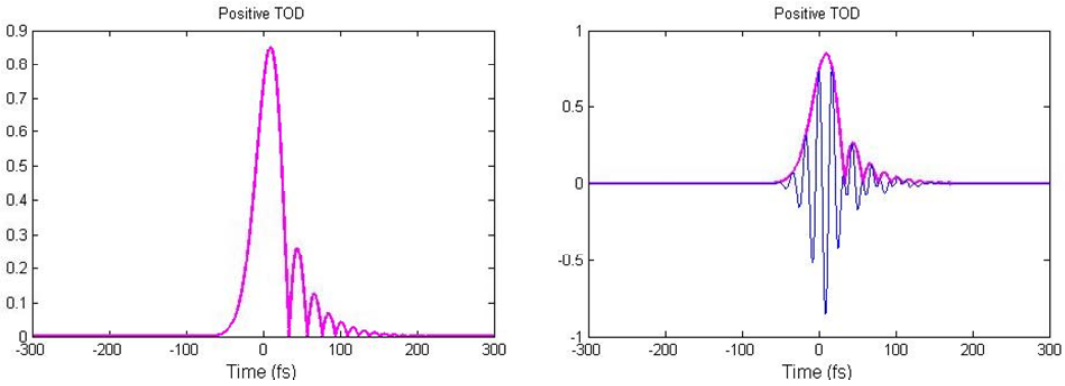

Fig. 1.5: TOD causes ringing in the pulse envelope.

The spectral bandwidth and the spectral phase can also vary along the cross-section of the beam, which is always the case in the presence of spatiotemporal couplings such as spatial chirp, pulse front tilt, and angular dispersion. In these cases the minimum pulse width cannot be obtained at all positions across the beam because the spectral bandwidth at any given position is lower than the full spectral bandwidth of the beam. Also, in presence of the spatiotemporal couplings the beam cannot be focused to its diffraction-limited spot for the given beam size and the lens parameters[35]. The spatial coherence of the laser beam is also of great significance in many applications. The spatial mode quality of a beam is determined by the space bandwidth product, which is just the product of the beam width and the spatial-frequency bandwidth[36]. Similarly, the complexity of the pulse in time domain is given by the time-bandwidth product, which is the product of temporal pulse width and the spectral bandwidth. High values of either the space bandwidth product or the time bandwidth product (or both) is indicative of a poor beam quality and a complex pulse.

A complete mathematical description of the pulse electric fields in space and time is often required, and can be given by the following equations:

$$E(x,y,z,t) = \sqrt{I(x,y,z,t)}\,\exp\{-i\phi(x,y,z,t)\} \tag{1.6}$$

$$\tilde{E}(x,y,z,\omega-\omega_0) = \sqrt{S(x,y,z,\omega-\omega_0)}\,\exp\{-i\varphi(x,y,z,\omega-\omega_0)\} \tag{1.7}$$

1.4.1 Nonlinear methods for pulse compression

There are several nonlinear methods that are used for pulse shaping and pulse compression by exploiting nonlinear interactions. These methods, however, fall outside the scope of the work presented in this thesis, but the nonlinear pulse compression, as a topic, nevertheless, merits a brief discourse for the sake of completeness of the discussion on pulse compression. This section gives a brief overview of a few nonlinear techniques used for pulse compression.

Electro-optic phase modulators can apply an arbitrary spectral phase to produce shaped pulses or a quadratic phase to the pulse to compress or stretch a pulse[37]. Acousto-optic programmable dispersion filters (AOPDF) can be employed for pulse stretching and compression as well as pulse shaping[38]. Pulse compression using tapered photonic crystal fibers have been reported to produce pulses as short as 20fs [39, 40]. Filamentation of the beam also can cause pulses to compress[41]. Analogous to spatial imaging, it is also possible to do temporal imaging because of the space-time duality of Maxwell's equations. And the magnification or demagnification in time domain is equivalent to pulse stretching and compression. Parametric time lensing is a

method that uses four wave mixing process to impart a quadratic temporal phase to the pulse, and has been demonstrated for pulse measurement and dispersion compensation[42]. A broadband pump pulse is linearly chirped by using a fiber and the quadratic phase of the pump is imparted on the four wave-mixing signal. The pulse duration in time lensing acts analogous to an aperture, therefore, a spectrally flat pump pulse is desired to give equal weights to all the temporal components.

1.4.2 Pulse compression using chirped mirrors

Chirped mirrors are made of layers of dielectric coatings which precisely reflect a particular wavelength at a particular depth inside the mirror. The wavelength that is reflected increases linearly with the axial position in the mirror. This adds negative chirp to the pulse by putting the bluer wavelength ahead of the redder wavelengths in the pulse upon a reflection off a chirped mirror. Typically, each bounce off the mirror adds ~200fs^2 of GDD dispersion and several hundred reflections of the pulse are required for dispersion compensation using chirped mirrors in the most cases. Fortunately, at small bandwidths, they have very high reflectance per bounce ~ 99.99%, so the over all losses are not prohibitively high. But as the operating bandwidths are increased, the reflection efficiency of chirped mirrors falls rapidly. They still find application inside the laser cavity where there is a positive gain in the pulse energy on each roundtrip. The angular incidence of a pulse invariably introduces spatial chirp in the beam. So, in the chirped mirror pulse compressors the reflections are paired to minimize the introduced spatial chirp and minimize the introduced wave front aberrations. They are also used to compensate for the higher order dispersion, such as TOD and FOD (fourth order dispersion)[43]. But the only drawback is that once a mirror is synthesized the ratio of the

higher order dispersion to GDD remains fixed and cannot be altered, which narrows the scope of application to only specific problems.

1.4.3 Chirped volume Bragg gratings

Fiber Bragg gratings have found great success in applications for wavelength filters and as chirped FBGs in dispersion compensation, in various fiber optic applications. Volume Bragg gratings are analogous to FBGs, except that they are created in blocks of glass. With the recent advancement in the manufacturing process of Bragg gratings, researchers have succeeded in making such gratings with excellent uniformity over large cross-sectional areas of up to 5mm of clear aperture[44]. In CVBGs the refractive index is modulated along the z-axis of the grating and the period of modulation varies linearly with 'z'. Therefore, the Bragg wavelength or the wavelength that satisfies the Bragg condition for reflection increases along the z-axis of the CVBG. The Bragg reflection itself can be close to 99.99% but the scattering losses have limited the single pass efficiency to ~50%. They are extremely compact in size and add significant amounts of GDD without requiring any multiple reflections. The rest of the features and limitations are identical to chirped mirrors, however, the same CVBG can stretch and compress a pulse when used from both ends.

1.4.4 Pulse compression with angular dispersion

Angular dispersion produces negative GDD, and the pulse compressors based on angular dispersion are the most versatile and most commonly used devices for dispersion compensation. In this work we focus on the spatio temporal modeling of the pulse compressors, to understand their working and their effects on the pulses. We design

the extra cavity pulse compressors that use a single dispersive element, do not add any spatio-temporal distortions, are compact in size, and have easy tunability of the amount of compression added. We extended the single dispersive element idea to use a grating, a grism, and a prism-grating combination to compensate for the higher order dispersion, a problem which is very difficult to solve otherwise for various reasons. A compressor that can control dispersion up to third order is extremely useful for fiber delivery of the ultrashort pulses to the experiments, amongst many other applications. Another significant advantage of these compressors over others is that they can be built with off-the-shelf components.

1.5 Thesis outline

In this thesis, the spatio-temporal modeling of pulse compressors is discussed in chapter 2. This chapter first describes a few applications of pulse stretchers and compressors, briefly describes their working principles and lays down the motivation for modeling pulse compressors both in space and time. It discusses two different matrix based approaches, then describes the modeling of a pulse compressors using Kostenbauder formalism with examples. Chapter 3 explains the working of pulse compressors in general, and introduces single-grating and grism pulse compressors[45], the latter for material dispersion compensation up to third order. It also has the experimental results and the results from simulation for the two. Chapter 4 introduces a prism/grating based compressor to higher order dispersion control[46], describes the results obtained in the experiments and simulations. Chapter 5 introduces a general dispersive law[47] that can be used for calculating the total dispersion and magnification introduced by an arbitrary sequence of dispersive devices. Chapter 6 describes the double

blind polarization gating FROG, a technique that can measure two unknown pulses simultaneously using two PG frog traces obtained from a single shot PG FROG experiment setup.

CHAPTER 2

SPATIO-TEMPORAL MODELING OF PULSE COMPRESSORS

2.1 Introduction

Pulse compressors are essential in all ultrashort-laser-pulse based experiments and applications. All regenerative amplifiers that generate high energy pulses, with the output pulse energies varying from a few millijoules per pulse to several joules per pulse, use the technique of chirped-pulse amplification (CPA). Pulse compressors and stretchers are the most important components of a CPA system. In CPA, a weak femtosecond pulse (nanojoules/pulse) is used as a seed pulse and is stretched in time by using a stretcher by a few orders of magnitude, in the first stage. In the second stage, this several picoseconds long pulse can then be safely amplified in a gain medium, to a few millijoules pulse energy, and thus, the nonlinear damage to the amplifier and to the pulse spatial and temporal profile can be avoided. Finally, in the third stage, this high energy pulse is recompressed to its shortest duration using a pulse compressor, thus obtaining the output pulse with the highest peak intensity. Additionally, there are many applications that rely on the duration of pulses being the shortest, such as multi-photon imaging, micro-machining and optical parametric amplification. Propagation through materials causes the pulses to spread out in time as ultrashort pulses have large bandwidths and different wavelengths of light travel at different speeds through materials. This results in decreased

peak intensity. Therefore, they must be compressed before they can be used in most applications.

This has motivated the development of a new class of extra-cavity pulse compressors that can provide control over the pulse width in any experiment. The stretching and compression of a pulse in a pulse compressor is brought about by introducing angular dispersion by using a dispersive device such as a grating, prism, or grism. Along with the angular dispersion, several other spatio-temporal distortions are introduced, which should subsequently cancel inside the pulse compressor. Ideally, the net effect is only a stretched/compressed pulse in the output. Therefore, modeling of pulse compressors/stretchers is an important task to study the workings of the pulse compressor and the pulse properties at each stage of the compression process.

Most available methods model only the temporal properties of the pulse. Neglecting the full spatio-temporal properties of a pulse can lead to an incorrect/inadequate compressor design, and an incomplete analysis of the functioning of a pulse compressor. Therefore, these methods can present serious limitations. Using our method of simulation, it is easy to model a pulse stretcher/compressor accurately and study the spatio-temporal distortions introduced by it due to minor misalignments. We also studied the evolution of spatio-temporal distortions on propagation, and they were found to worsen on propagation; distorting the pulse even more and thus rendering it useless for almost any application. To our knowledge, we have constructed the most complete method of modeling complete compressor system.

For spatio-temporal modeling, matrix methods prove advantageous for well known reasons of low computational-resource requirement, physical insight that they can

provide, and the ease of implementation. For spatio-temporal modeling of pulse compressors using a matrix approach, there are two methods that can be used, namely, Wigner space-time functions, and the Kostenbauder matrix formalism. In both of these methods, an optical device can be represented by a two dimensional, 4x4, real matrix, and a series of optical components can be modeled as a matrix product; details of these methods are presented in the following section. Solving Maxwell's equations for modeling of all the optical elements can of course provide information about the higher order effects, but this approach is much more computationally intensive and time consuming. It is also much more difficult to implement because specifying boundary conditions becomes increasingly difficult with the increasing complexity of the optical system being modeled. In the following section, we briefly discuss Wigner matrices and Wigner space time functions[48], and then the Kostenbauder matrix[49] approach is discussed in more detail.

2.2 Wigner space-time functions and Wigner matrices

For a given electric field in space and time, Wigner space time function can be calculated as shown in eq. 2.1

$$W^{ST}(x,\omega,\xi,t)=\frac{1}{2\pi}\iint E\left(x+\frac{x'}{2},t+\frac{t'}{2}\right)E^{*}\left(x-\frac{x'}{2},t-\frac{t'}{2}\right)e^{i(-\xi x'+\omega t')}dx'\,dt' \tag{2.1}$$

Where x, t are space and time co-ordinates of the E-field, and ξ, ω are the spatial frequency and the angular frequency, respectively. For example, we consider the case of a transform limited Gaussian pulse (eq. 2.2) and calculate the corresponding Wigner space-time (Wigner ST) function for it, eq. 2.3.

$$E(x,t) = e^{-ax^2 - bt^2} \tag{2.2}$$

$$W^{ST}(x,\omega,\xi,t) = e^{-2ax^2 - 2bt^2} . e^{-\frac{\xi^2}{2a}} . e^{-\frac{\omega^2}{2b}} \tag{2.3}$$

The Wigner ST function has all the information about the spatial, temporal, and spatio-temporal characteristics. To get the field information for a particular domain the marginal of the Wigner function is calculated for that domain. For example, a measure of the spatial chirp distortion is the tilt in the trace of $I(x,\omega)$ in x-ω domain, which can be obtained by calculating the following marginal (eq. 2.4)

$$\left|E(x,\omega)\right|^2 = \iint W^{ST}(x,\omega,\xi,t)\, d\xi\, dt \tag{2.4}$$

Similarly, the spatio-temporal couplings in other domains can be obtained by calculating marginals as shown in eqs 2.5 to 2.7.

$$\left|E(x,t)\right|^2 = \frac{1}{2\pi}\iint W^{ST}(x,\omega,\xi,t)\, d\xi\, d\omega \tag{2.5}$$

$$\left|E(\xi,t)\right|^2 = \frac{1}{4\pi^2}\iint W^{ST}(x,\omega,\xi,t)\, dx\, d\omega \tag{2.6}$$

$$\left|E(\xi,\omega)\right|^2 = \frac{1}{2\pi}\iint W^{ST}(x,\omega,\xi,t)\, dx\, dt \tag{2.7}$$

Once the Wigner space-time function for the input pulse field is calculated, the output field after the optical system can be determined using the Wigner matrix that represents the optical system. The Wigner matrix representing the optical element or a

sequence of first order optical devices is used to scale the coordinates of the input Wigner space-time function. The output Wigner ST function is same as the input Wigner ST function, but evaluated on the scaled co-ordinates. As an example, Wigner matrix for a lens transforms the input co-ordinate vector as shown in eq. 2.8.

$$\begin{bmatrix} x \\ \xi \\ t \\ \omega \end{bmatrix}^{scaled} = \begin{bmatrix} 1 & 0 & 0 & 0 \\ k_0 / f & 1 & 0 & 0 \\ 0 & 0 & 1 & 0 \\ 0 & 0 & 0 & 1 \end{bmatrix} \begin{bmatrix} x \\ \xi \\ t \\ \omega \end{bmatrix} \tag{2.8}$$

The output Wigner function after the lens is given by eq. 2.9, which evaluates the input Wigner ST function on the scaled co-ordinates.

$$W_{out}^{ST} = W_{in}^{ST}(x, \omega, \xi + \frac{k_0 x}{f}, t) \tag{2.9}$$

Similarly, for a series of elements in the beam path, each represented by a Wigner matrix 'M' and a magnification 'm', the output Wigner function is related to the input Wigner function as shown below.

$$W_{out}^{ST} = m_1 m_2 m_3 W_{in}^{ST}(M_1 M_2 M_3 X) \tag{2.10}$$

The output Wigner function can be computed numerically using Matlab and all the information needed to determine the pulse electric field can be obtained. In theory, the approach looks fine, but it poses some serious difficulties in implementation. Numerically implementing this calculation requires calculating and storing a Wigner ST function in four dimensions. Therefore, even for a barely appreciable resolution along

each dimension, the storage size quickly becomes unacceptably high. Secondly, in order to model even modestly complex systems, the numerical implementation fails because each time the Wigner matrix scales the co-ordinates, it causes the number of required dimensions of the variables storing data points to increase. Therefore, one has to resort to a symbolic math programming environment, which itself cannot deal with the calculations for complicated functions. The Wigner matrix method can potentially propagate any field distribution, as opposed to Kostenbauder matrix approach, which only propagates Gaussian field distributions, but the disadvantages of using Wigner matrices far outweigh the advantages. There is a linear transformation that exists between the Wigner matrices and K-matrices, therefore all the systems that can be represented by a Wigner matrix can also be represented by a K-matrix. Therefore, in this work, Kostenbauder matrix formalism was used for performing simulations and spatio-temporal analysis of pulse compressors.

2.3 Kostenbauder matrix formalism

A general Kostenbauder matrix can represent all the essential optical elements, such as lenses, gratings, prisms, mirrors, medium interfaces, and composite elements, such as a grism, up to the first order. A matrix representing each of these devices can be constructed from the device parameters such as grating line density, apex angle of the prism, and refractive index of the material used, et cetera. The matrix for a series of optical elements is given by the matrix product of the individual K-matrices in the same order in which the elements are encountered by the pulse. In a pulse compressor, the angular dispersion introduced in the first pass through the dispersive element is removed

by placing an identical and inverted dispersive element after it or by inverting the beam before the second pass. The latter is the case when a corner cube or a roof mirror is used to achieve inversion.

2.3.1 Ray-pulse vector and Kostenbauder matrix

In this formalism, a ray-pulse vector represents a pulse, it is similar to the ray vector used in the familiar ABCD matrix approach, but unlike ray vectors it has four co-ordinates: x, θ, t and f, each representing the position, slope, time and frequency respectively, of the ray-pulse. These co-ordinates are measured on the reference planes erected perpendicular to the reference axis at arbitrary locations, usually just before and after an optical device as shown in fig. 2.1. The reference axis in standard ABCD matrix approach is taken to be the optic axis of the optical system, but here the reference axis is defined as the path taken by a narrowband, transform limited pulse at the center frequency. The position and slope of any ray-pulse is measured with respect to the reference axis on the reference planes. When passing through a reference plane, the reference pulse sets the clock to zero, and the time co-ordinate of any other ray-pulse is the time given by the clock when it passes that reference plane. Therefore, the time co-ordinate of the ray-pulse under consideration is its delay with respect to the reference pulse. Similarly, the frequency co-ordinate of a reference pulse is the difference of its center-frequency from the frequency of the reference pulse.

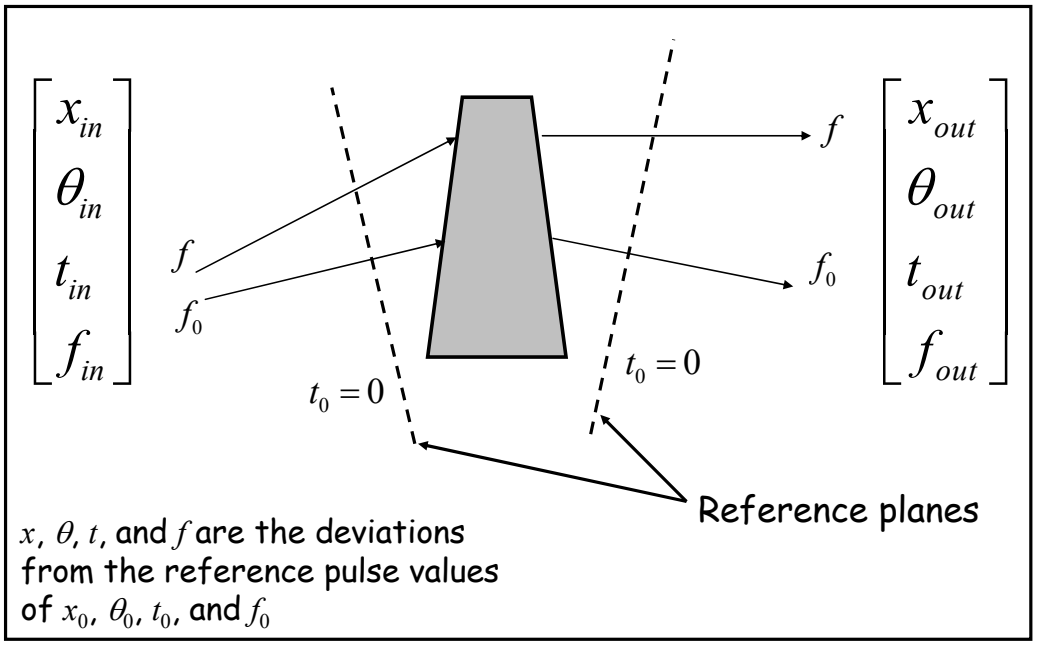

Fig. 2.1: Geometrical construction for the co-ordinates of a ray-pulse vector.

A Kostenbauder matrix relates the input ray pulse vector to the output ray pulse vector as shown in eq. 2.11. In order to construct a K-matrix for a device, the geometrical construction like the one shown in the figure above is used, in conjunction with eq. 2.11. All the derivatives in the eq. 2.11 are evaluated at the center frequency.

$$\begin{bmatrix} \underline{x} \\ \underline{\theta} \\ \underline{t} \\ \underline{f} \end{bmatrix}_{out} = \begin{bmatrix} \frac{\partial x_{out}}{\partial x_{in}} & \frac{\partial x_{out}}{\partial \theta_{in}} & 0 & \frac{\partial x_{out}}{\partial f_{in}} \\ \frac{\partial \theta_{out}}{\partial x_{in}} & \frac{\partial \theta_{out}}{\partial \theta_{in}} & 0 & \frac{\partial \theta_{out}}{\partial f_{in}} \\ \frac{\partial t_{out}}{\partial x_{in}} & \frac{\partial t_{out}}{\partial \theta_{in}} & 1 & \frac{\partial t_{out}}{\partial f_{in}} \\ 0 & 0 & 0 & 1 \end{bmatrix} \begin{bmatrix} \underline{x} \\ \underline{\theta} \\ \underline{t} \\ \underline{f} \end{bmatrix}_{in} \tag{2.11}$$

2.3.2 Beam inversion and the elements of interest in K-matrices

A general Kostenbauder matrix and the effect of beam inversion on it are shown in eq.2.12. This operation is essential in the modeling of pulse compressors. Beam inversion can be attained by using a roof-mirror in the plane of dispersion, by using a corner cube, or by inverting the dispersive element itself.

$$\begin{bmatrix} A & B & 0 & E \\ C & D & 0 & F \\ G & H & 1 & I \\ 0 & 0 & 0 & 1 \end{bmatrix} \xrightarrow{\textit{beam inversion}} \begin{bmatrix} A & B & 0 & -E \\ C & D & 0 & -F \\ -G & -H & 1 & I \\ 0 & 0 & 0 & 1 \end{bmatrix} \tag{2.12}$$

Each element of the general K-matrix represents a different spatio-temporal effect. A and D are magnifications, F is the angular dispersion, C and G are effective focal length and pulse-front tilt, respectively. B denotes position vs. slope. I represents GDD. E represents spatial chirp. H represents time vs. angle.

2.3.3 Propagating Gaussian beams with K-matrices

A Gaussian beam in space and time can be described in terms of 2x2 complex matrices, commonly referred to as 'Q' matrices, eq. 2.13. The complex Q-matrices are anti-symmetric, i.e. $Q_{21}^{-1} = -Q_{12}^{-1}$. Therefore, out of the total eight parameters in the four complex entries of a Q-matrix only six are independent. These six independent parameters can describe a Gaussian beam-pulse completely in space and time up to first order.

$$E(x,t) \propto \exp\left\{-i\frac{\pi}{\lambda}[x,-t]\,Q^{-1}\begin{bmatrix} x \\ t \end{bmatrix}\right\} = \exp\left\{-i\frac{\pi}{\lambda}[x,-t]\begin{bmatrix} Q_{11}^{-1} & Q_{12}^{-1} \\ Q_{21}^{-1} & Q_{22}^{-1} \end{bmatrix}\begin{bmatrix} x \\ t \end{bmatrix}\right\} \tag{2.13}$$

$$E(x,t) = \exp\left\{-i\frac{\pi}{\lambda}[Q_{11}^{-1}x^2 + 2Q_{12}^{-1}xt - Q_{22}^{-1}t^2]\right\} \tag{2.14}$$

The off-diagonal terms in the Q-matrix represent the coupling term in the intensity and phase. To study the coupling in a particular domain, e.g. spatial chirp in x-ω and angular dispersion in k-ω domain, the corresponding Fourier transforms are performed. To measure a particular spatiotemporal coupling, one has to measure it in a domain where it is real or is present in the intensity. For example, the pulse front tilt is a cross term in $\varphi(ax)$ in eq. 2.15, where it cannot be measured directly, but taking a Fourier transform to x-t domain, eq. 2.16, reveals this coupling as a tilt in the two dimensional plot of $I(x,t)$.

$$\tilde{E}(x,y,z,\omega) = \tilde{E}_0(x,y,z,\omega)\, e^{i\gamma(\omega-\omega_0)x} \tag{2.15}$$

$$\Rightarrow E(x,y,z,t) = E_0(x,y,z,t+\gamma x) \tag{2.16}$$

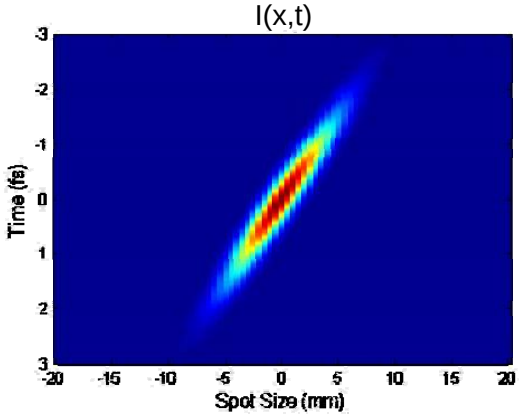

Fig. 2.2: Pulse intensity in x-t domain (red is the max. intensity and blue is zero)

For the Gaussian beams, it is a set of six independent parameters that is sufficient for their complete description up to first order in each domain. The analytical relations

between the parameters in different domains have been worked out in detail[50], so there is no need for performing Fourier transforms of the fields to look at the spatiotemporal information in other domains. Therefore, the complex Q-matrices combined with the Kostenbauder matrix formalism, provide a good basis for modeling pulse compressors.

The propagation of a Gaussian beam through an optical system represented by a Kostenbauder matrix is similar to the inverse-q propagation in the ABCD matrix method. The output Q-matrix is given in terms of the elements of the K-matrix representing the optical system and the input Q-matrix as shown in eq. 2.15.

$$Q_{out} = \frac{\begin{bmatrix} A & 0 \\ G & 1 \end{bmatrix} Q_{in} + \begin{bmatrix} B & E/\lambda \\ H & I/\lambda \end{bmatrix}}{\begin{bmatrix} C & 0 \\ 0 & 0 \end{bmatrix} Q_{in} + \begin{bmatrix} D & F/\lambda \\ 0 & 1 \end{bmatrix}} \tag{2.15}$$

2.4 Modeling of pulse compressors using K-matrices

Pulse compressors that use angular dispersion to stretch or compress pulses, generally use multiple dispersive devices or multiple passes through these devices. The working principle of these pulse compressors are discussed in a greater detail in the following two chapters. To study the complete effect of pulse compressors on ultrashort pulses, we model them using the K-matrix formalism. To elucidate the method, we discuss the example of a diffraction grating pulse compressor in the following subsection. In the final results, we will be able to see the various effects on the output pulse and the effects of the misaligned compressor on propagating the pulse farther. In the subsequent subsection, the construction of a K-matrix for a composite dispersive element, a grism, which is a grating written on the back face of a prism has been described.

2.4.1 Grating pulse compressor

The K-matrix of a reflection grating is determined by the grating line density and the angle of incidence of the beam on to the grating. Knowing the angle of incidence of the input beam from the grating surface, ψ_i, the angle of the diffracted order, ψ_d, is determined for the mth order using the grating equation 2.16, where 'd' is the grating period.

$$\cos\psi_d - \cos\psi_i = \frac{m\lambda_0}{d} \tag{2.16}$$

The K-matrix for the grating is then given as:

$$K_{grating} = \begin{bmatrix} -\frac{\sin\psi_d}{\sin\psi_i} & 0 & 0 & 0 \\ 0 & -\frac{\sin\psi_i}{\sin\psi_d} & 0 & \frac{c(\cos\psi_d - \cos\psi_i)}{\lambda_0 \sin\psi_d} \\ \frac{\cos\psi_i - \cos\psi_d}{c\sin\psi_i} & 0 & 1 & 0 \\ 0 & 0 & 0 & 1 \end{bmatrix} \tag{2.17}$$

To model a standard four grating pulse compressor, the K-matrix for each bounce of the pulse on the gratings is written using the incidence and the diffraction angles of the beam. Then the matrices of the elements are multiplied in the same order as they are visited by the pulse, including the free space propagation in between the gratings. The figure below shows the schematics of a standard four grating pulse compressor and eq. 2.18 gives the final K-matrix for the compressor.

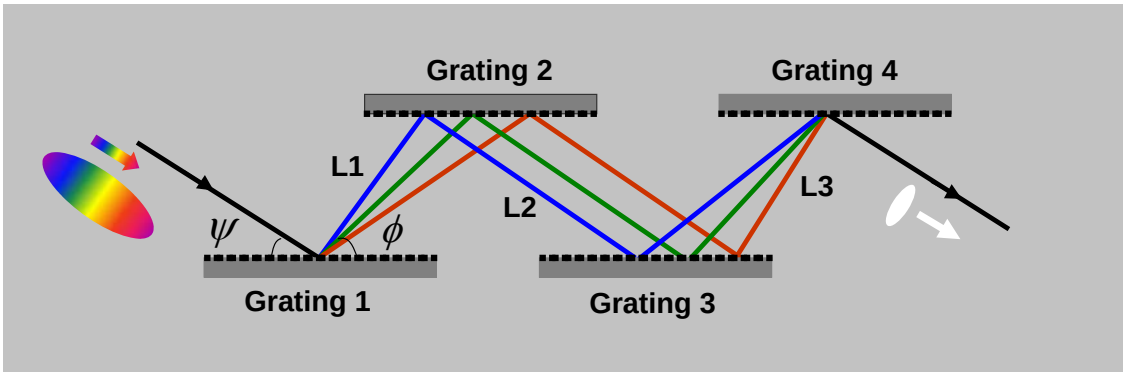

Fig. 2.3: A four grating pulse compressor.

$$K_{compressor} = K_{grating4} K_{L3} K_{grating3} K_{L2} K_{grating2} K_{L1} K_{grating1} \tag{2.18}$$

In the simulation for this compressor, we use 600 lines/mm gratings, separated by a distance of 10 cm. The input beam is incident at an angle of 25 degrees from the surface and the grating pairs are misaligned angularly by 2^{o}. There is also a separation mismatch between the two grating pairs of 0.5 cm. The input to the compressor is a 50 fs transform limited pulse, and the negatively chirped output pulse of ~ 4 ps FWHM pulse width is shown in the figure below. The false colors indicate the position of each wavelength and the brightness shows the pulse intensity in *x*-*t* domain.

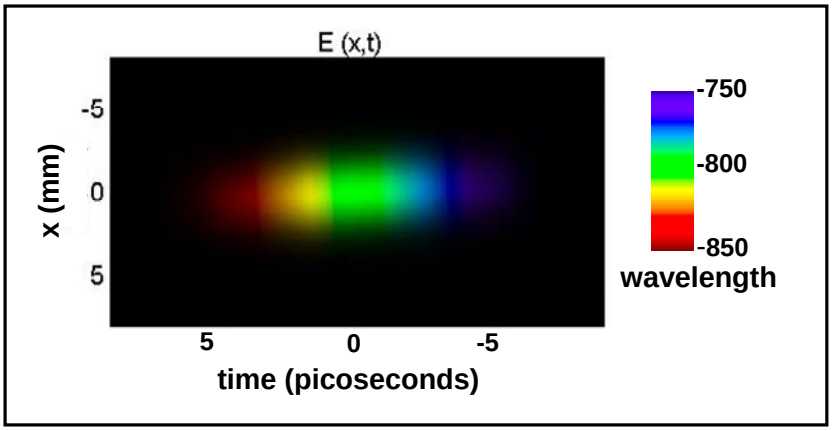

Fig. 2.4: The output pulse of a misaligned four grating compressor.

On propagating the output pulse farther by a distance of 10 meters the spatiotemporal couplings are seen worsen, as angular dispersion generates spatial chirp on propagation.

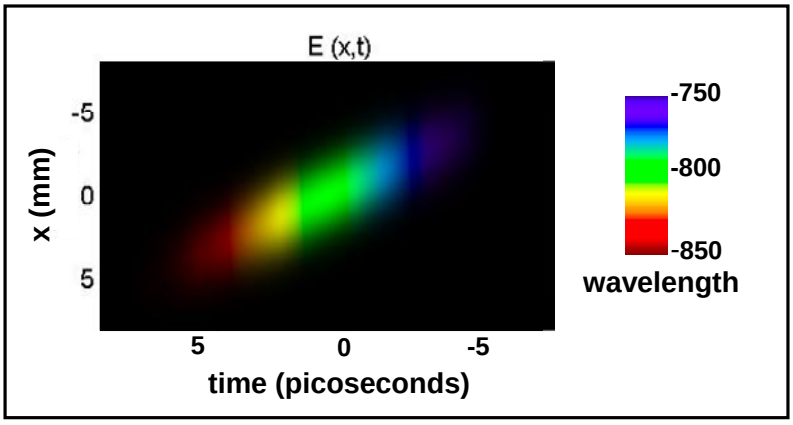

Fig. 2.5: The output of a misaligned compressor on propagation.

A method to quantify the spatiotemporal couplings present in different domains is by using rho parameters introduced by Pablo et. al[51]. A rho parameter can be computed for all the spatiotemporal couplings. Rho parameters vary sharply for small values of the spatiotemporal couplings, therefore, they are really useful for comparisons between different cases. They however are bounded, i.e. $-1 < \rho < 1$, so for comparing large values they are not very useful.

2.4.2 Grism based compressor

A grism is a prism with a grating written onto it or glued to its back face. A grism based compressor can compensate for material dispersion up to third order for almost all the materials, a feat which cannot be achieved by using a prism or a grating compressor alone. In order to model a grism based compressor, we first derive the K-matrix for a

tilted interface between media of different refractive indices. Using a similar geometrical construction as shown in figure above, we obtain the matrix for a tilted interface as in eq. 2.19.

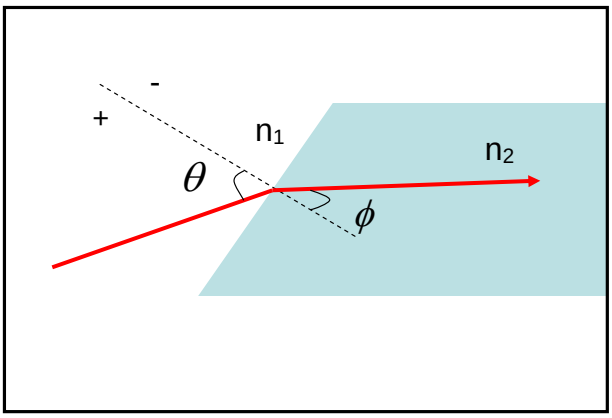

Fig. 2.6: Tilted interface between two dispersive media.

$$K_{interface} = \begin{bmatrix} \frac{\cos\phi}{\cos\theta} & 0 & 0 & 0 \\ 0 & \frac{\cos\theta}{\cos\phi} & 0 & \frac{\frac{dn_1}{df}\sin\theta - \frac{dn_2}{df}\sin\phi}{n_2\cos\phi} \\ \frac{\frac{dn_1}{df}\sin\theta - \frac{dn_2}{df}\sin\phi}{\lambda_0\cos\theta} & 0 & 1 & 0 \\ 0 & 0 & 0 & 1 \end{bmatrix} \quad (2.19)$$

Where, θ, is the angle of incidence measured from the surface normal, and, ϕ, is the angle of refraction. The figure below shows a grism that was used in our experiments. It uses a 600lines/mm grating glued to the back of a 90 degree SF2-glass prism. The beam path inside the grism is shown by a dotted line on the top. The beam goes through the incidence face and then internally reflects from the diagonal face towards the grating.

The first order diffracted beam from the grating then exits the diagonal face. This is considered as a single pass through the grism.

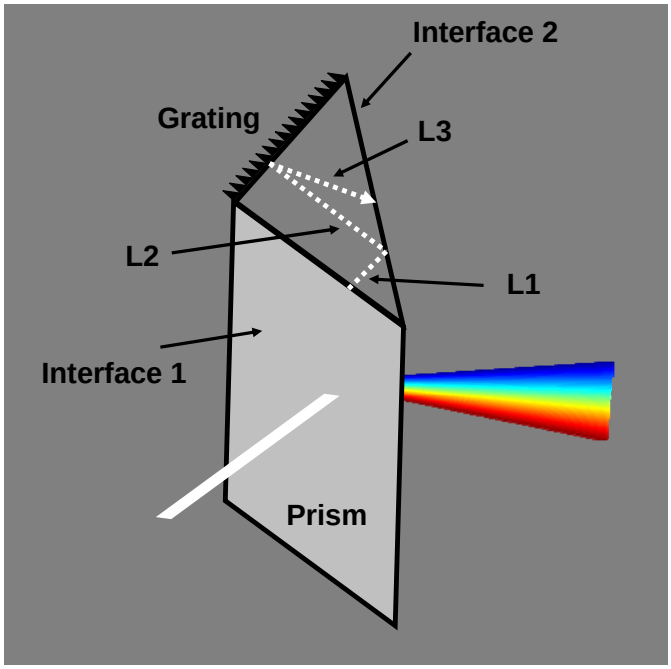

Fig. 2.7: A total internal reflection grism.

The K-matrix for a single pass through a grism is given by eq. 2.20. The K-matrices used for the propagation in glass also account for material dispersion introduced, the only new matrix we needed for this calculation was the matrix for a tilted interface which we have derived on the previous page.

$$K_{grism} = K_{interface2} K_{L3} K_{grating} K_{L2} K_{L1} K_{interface1} \tag{2.20}$$

Finally, a four pass grism pulse compressor can be modeled using this matrix as shown in eq. 3.5

CHAPTER 3

Single-diffraction-grating and grism pulse compressors

3.1 Introduction

An ultrashort pulse lengthens in time as it propagates through a dispersive medium, where lower frequencies of light propagate faster than higher frequencies. This effect, called group-delay dispersion (GDD), is undesirable in most applications, especially micromachining and multi-photon imaging, which thrive on the shortest possible pulses.

Only a few approaches exist for compensating for GDD and hence shortening the pulse to its transform-limit. The most common approach for introducing negative GDD is through angular dispersion. Angular dispersion, irrespective of its sign, always yields negative GDD[52, 53]. Dispersion can be introduced by simply propagating the pulse through a prism[54], a grism (a diffraction grating written on a prism)[55] or diffracting it off a grating. The amount of negative GDD is proportional to the distance traveled by the pulse after the dispersing component and the square of the angular dispersion.

Although angular dispersion introduces the desired negative GDD, angular dispersion itself is undesirable, and it also introduces undesired spatial chirp and pulse-front tilt, and thus is not generally useful by itself[50]. Useful pulse compressors based on angular dispersion necessarily require four identical dispersive components, the first to introduce angular dispersion (and hence negative GDD), the second to compensate for

the angular dispersion, the third and fourth to compensate for the spatial chirp after two prisms. A well-aligned pulse compressor, in principle, introduces negative GDD without the unwanted distortions of residual angular dispersion and spatial chirp and also without other spatio-temporal distortions, such as pulse-front tilt[50], which typically accompany angular dispersion and spatial chirp[56].

Unfortunately, in practice, it is difficult to align—and maintain aligned—many of the commonly used compressors because these multiple dispersive elements must be identical and have identical incidence angles. A simple small variation in the input beam pointing direction is enough to introduce significant amounts of the various spatio-temporal distortions.

Consider a four-element pulse compressor (Fig. 3.1). If aligned correctly, the net result is just the addition of negative GDD to the pulse. However, unless the elements are positioned at precisely the same incidence angles, some residual angular dispersion, spatial chirp, and pulse-front tilt in the output pulse will occur[57]. To adjust the amount of GDD introduced in grating or grism compressors, the separations between the first two and last two elements must be changed and maintained equal. Another undesirable characteristic of compressors is that wavelength tuning requires the adjustment of all four prisms to maintain identical incidence angles. As a result, four-element pulse compressors are prohibitively cumbersome devices to use in practice.

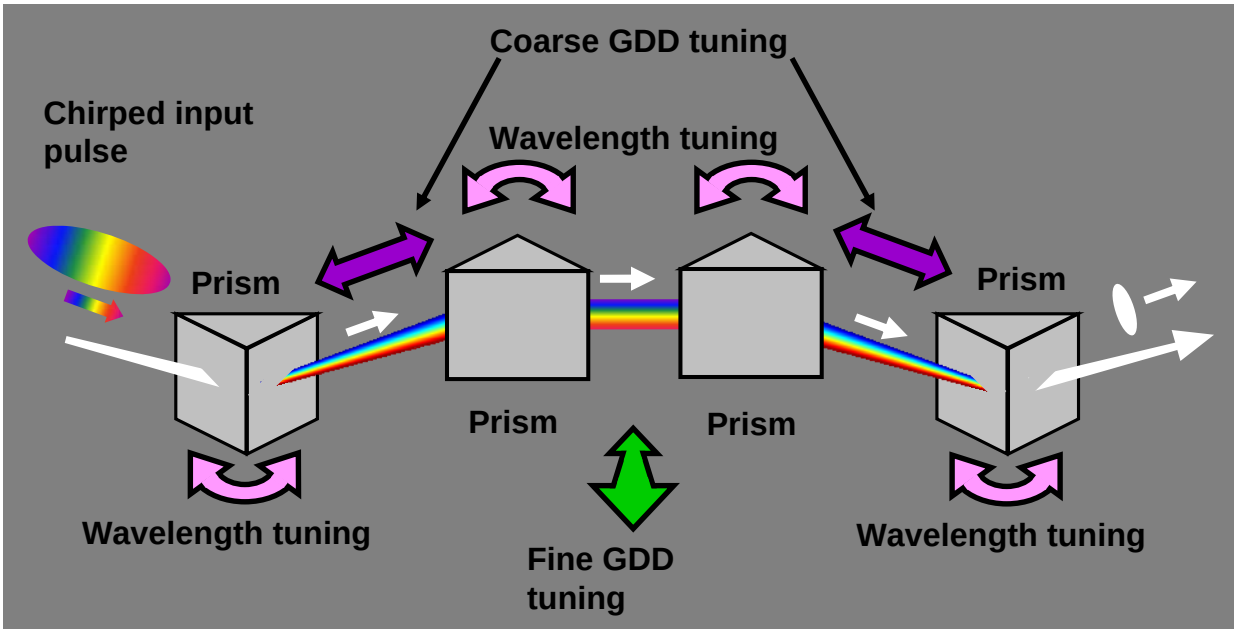

Fig. 3.1. A conventional four-prism pulse compressor (fig. borrowed from Ultrafast Optics lectures: by Rick Trebino).

Compressors have been simplified to two components by placing a periscope after the second element and folding the beam back through the first two elements (see Fig. 3.2). This design halves both the complexity and the size of the four-element design, but the difficulty of maintaining equal angles of the two dispersive elements and the inability to readily tune GDD in grating and grism designs remain problematic.

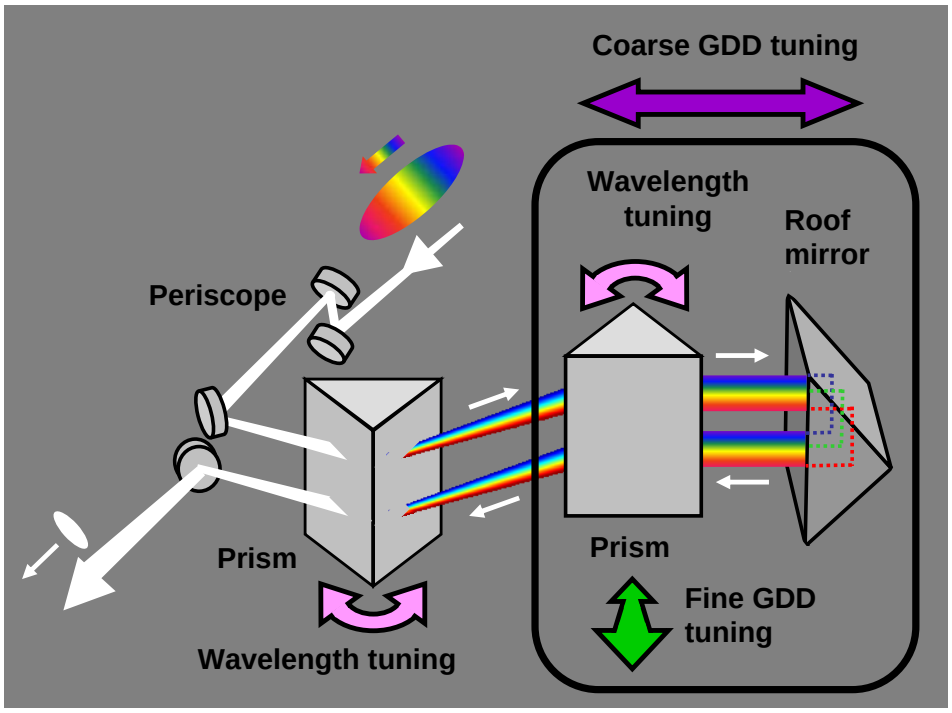

Fig 3.2: A two prism pulse compressor (fig. borrowed from Ultrafast Optics lectures: by Rick Trebino).

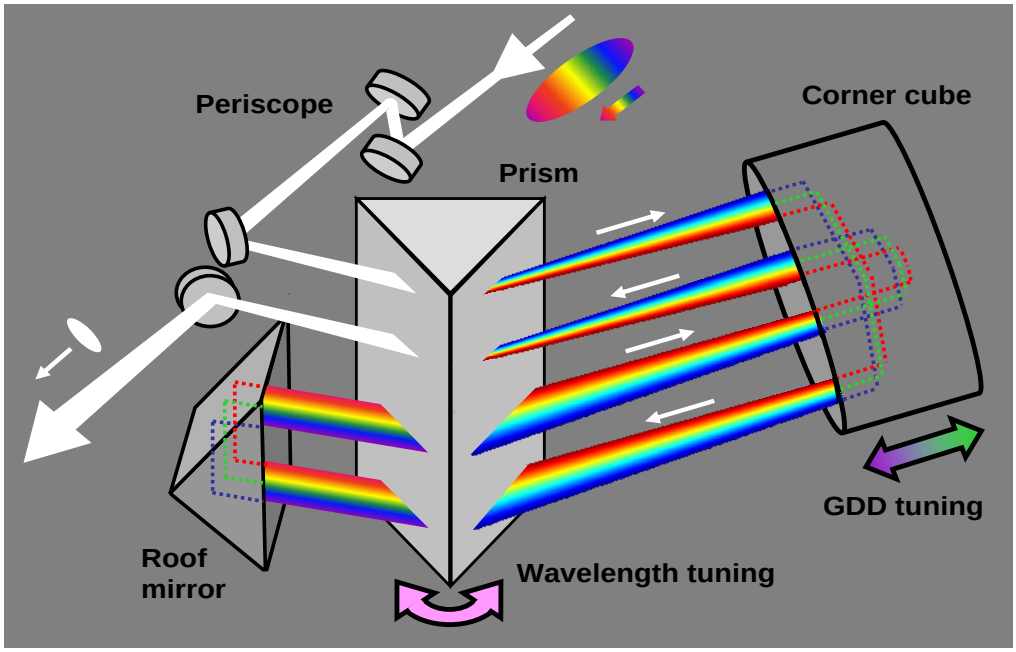

Fig. 3.3: Schematic diagram of a single prism pulse compressor (fig. borrowed from Ultrafast Optics lectures: by Rick Trebino).

A recently introduced single-prism pulse compressor solved all of the alignment issues by reducing the number of dispersive elements to one and permitting easy GDD tuning through the use of a corner cube [58](see Fig. 3.3). It quadruple-passes the prism, using a corner cube to retro-reflect the beam back to the prism and simultaneously invert it (so the prism need not be inverted). Corner cubes are extremely accurately manufactured, so the dispersion added on the second (fourth) pass is identical to that in the first (third) pass. The device continues to use a (less precise) roof mirror between the second and third passes through the prism (i.e., on the other side of it), where beam inversion is not appropriate and alignment is not as critical. Translating the corner cube varies the beam propagation distance between the "prisms" and effectively tunes the GDD over a large range. Because the device tunes by varying the propagation distance between prism passes, it has the additional advantage that it can simultaneously accommodate both large and small bandwidths by simply changing the distance. This is a great advantage over two- and four-prism designs, which must use a fixed prism separation and tune by moving a prism into and out of the beam, and so cannot accommodate large and small bandwidths unless additional re-alignment is performed.

Prism-based compressors, however, have limits on the magnitude of negative GDD that can be introduced. Since diffraction gratings and grisms are much more dispersive than prisms, grating and grism compressors can provide much larger amounts of negative GDD, approximately two orders of magnitude more than prism compressors for the same-size device.

So here we introduce single-grating and single-grism compressors based on this single-dispersive-component/corner-cube design. Single-grating (aberration-free)[59]

compressor designs and devices based on the use of two roof mirrors have been introduced previously, but do not achieve such alignment ease, and the use of corner cubes has not been mentioned in earlier work on grating or grism compressors, to the best of our knowledge. Usually, such compressors are used in chirped pulse amplification, where tuning of group delay dispersion is not as important. Our analysis of spatiotemporal distortions shows, however, that all previous designs are prone to them. After following careful alignment steps, such a compressor or stretcher is best left untouched, and input beam wander must be minimized. It is important to note that the magnitude of the undesired spatiotemporal distortions scales with the amount of GDD added by the compressor. Therefore, conventional compressor designs require even higher alignment precision when a highly dispersive element like a grating or a grism is used.

In our single-dispersive-element/corner-cube design, the use of the corner cube succeeds in achieving the maximum accuracy for cancellation of all first-order spatio-temporal distortions, including angular dispersion and spatial chirp. In our design, tuning the GDD involves simply translating the corner cube, and tuning the wavelength involves simply tuning the grating angle. It also automatically achieves unity beam magnification. In addition, the corner cube causes the input beam to track the output beam; so, even if the compressor is bumped, it remains aligned. And due to the double-passing of the path, it is also half the size of analogous two-grating devices. Finally, unlike current designs, the same device can be used for a much larger bandwidth by simply restricting the corner cube distance.

As mentioned above, nearly all materials exhibit positive GDD and TOD (third order dispersion) at wavelengths near 800 nm. It is well known that prism and grating compressors designed to compensate for a given amount of GDD (second-order dispersion) cannot independently compensate for third-order material dispersion. While materials generally have a positive TOD-to-GDD ratio, grating compressors always have a negative TOD-to-GDD ratio, so compensation of large amounts of dispersion using a grating compressor exacerbates the TOD thus distorting the pulse significantly in time. Prism-based compressors have the correct sign, but they lack ratio tuning and only offer a relatively small amount of dispersion compensation. A grism compressor [60, 61]of conventional design can address this issue, but current designs have the same limitations as conventional grating and prism designs because they consists of multiple dispersive elements and cannot be easily tuned for varying amounts of GDD. A single-grism pulse compressor is automatically aligned for zero spatiotemporal distortions and can compensate for both GDD and TOD simultaneously.

In this work, we also extend this concept to design a single-grism pulse compressor, which also has all of the above advantages, and in addition, can be used to compensate for material dispersion up to third order. And using it, we demonstrate fourth-order-limited dispersion compensation for a 30-nm bandwidth, 800-nm wavelength pulse that has propagated through 10 m of optical fiber.

3.2 Single-diffraction-grating pulse compressor

Our single-diffraction-grating pulse compressor uses only three elements: a reflection grating, a corner cube, and a roof mirror. The input beam diffracts off the reflection grating and impinges on to the corner cube, which retro-reflects this angularly

dispersed beam anti-parallel to the one incident on it, with the spatial order of colors reversed (see Fig. 4). This inverts the beam and causes a sign reversal of angular dispersion introduced by the grating on the second pass. Therefore, after the first two passes, the angular dispersion in the beam compensated, as required. A roof mirror reverses the beam path at a different height while maintaining the same order of colors in the dispersed beam. The last two passes thus remove both the spatial chirp and pulse front tilt, while doubling the magnitude of GDD as required.

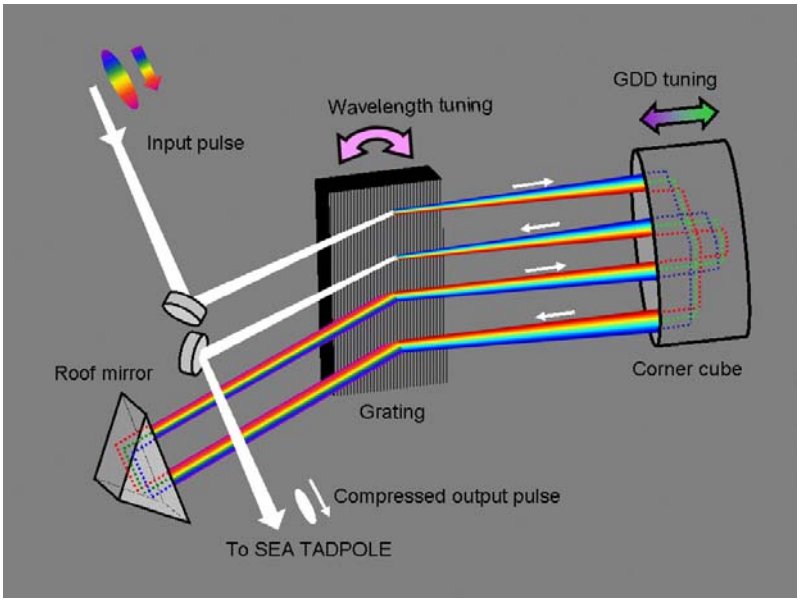

Fig. 3.4. Schematic diagram of single grating pulse compressor.

3.3 Single grism pulse compressor and third order dispersion

The single-grism design follows directly from the earlier single-prism compressor[58], and the single-grating design mentioned in this paper. We replaced the grating in the single-dispersive-element design with a reflection grism as shown in Fig. 5. The grism used in this experiment is a right-angled SF2 glass prism with a 600 groove-per-mm reflection grating glued to its base. The input beam is incident on the face of the

grism, which is orthogonal to the grating. It then undergoes total internal reflection at the diagonal face of the grism and finally exits the diagonal face of the grism after it diffracts off the grating. The beam path in each pass through the grism is depicted on the top of the grism with a dashed line (see Fig. 5). After the first pass, the beam is reflected back onto the grism using a corner cube. As in the single-prism design, the corner cube functions as a retro-reflector and a beam inverter, and the device functions analogously to the single-prism and single-grating designs. At the correct angle of incidence, however, the output pulse thus obtained has negative GDD *and* negative TOD in the correct ratio to cancel out material dispersion to third order, and it has no spatiotemporal distortions.

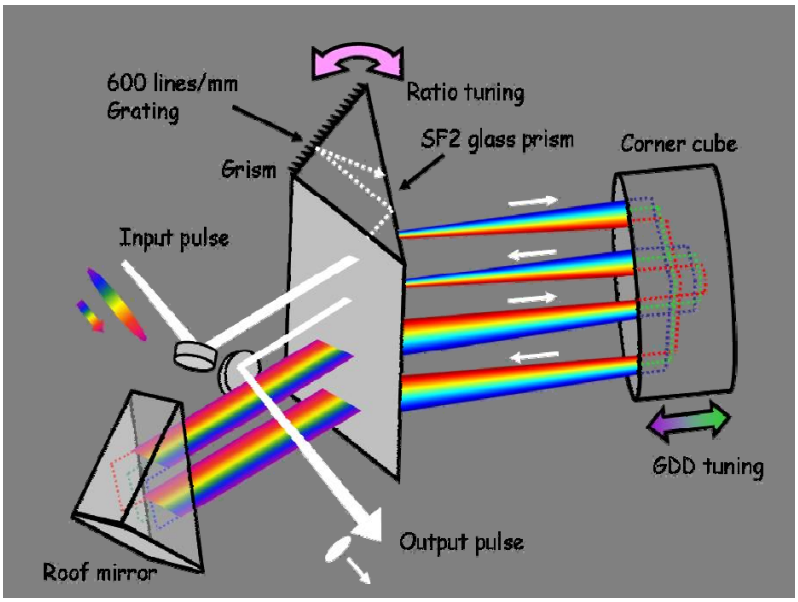

Fig. 3.5: Schematic diagram for a single grism pulse compressor.

3.4 Modeling and simulation

3.4.1 Single-grating pulse compressor

Unity beam magnification

The corner cube very accurately retro-reflects the beam, so the exit angle after the first pass is equal to the incidence angle for the second pass. An analytical calculation using Kostenbauder matrices[49] shows that the spatial magnification of the beam for each pass is:

$$M_1 = -\frac{\sin\psi_d}{\sin\psi_i} = M_3 \quad \text{and} \quad M_2 = -\frac{\sin\psi_i}{\sin\psi_d} = M_4 \tag{2}$$

Where ϕ and ψ are the diffracted and incidence angle of the beam measured from the grating surface (not the normal to it), the definitions of the angles in Kostenbauder's paper. Therefore, total magnification of this device is always unity. The above calculation also applies to angular magnification.

Wavelength tuning of the single grating pulse compressor

Once this device is set up to operate at a particular wavelength, it is easy to tune for other wavelengths. As is evident from the figure (see Fig. 4) shown above, looking from the top, the grating is rotated counter-clockwise if wavelength is decreased and clockwise for longer wavelengths. The beam path in the device does not change in either case. Therefore, this device can be tuned for a different wavelength by rotating just one knob, which rotates the only grating used.

No spatio-temporal distortions

Again, using the Kostenbauder matrix formalism, it is easily deduced that the beam emerging from the single-grating compressor has zero pulse-front tilt, zero spatial

chirp, and zero residual angular dispersion. Since, as mentioned, the corner cube retro-reflects the beam, the exit angle after the first pass is the same as the incidence angle for the second pass. Therefore, the compressor is auto-aligned to introduce zero distortions, independent of the incidence angle of the beam.

$$K = K_{grating} K_{space} K_{grating} K_{mirror} K_{grating} K_{space} K_{grating} \tag{2}$$

The calculated Kostenbauder matrix (Eq. 2) shows that added spatial chirp $K_{1,4}$, angular dispersion $K_{2,4}$, and pulse front tilt $K_{1,3}$ are all zero. The GDD, $K_{3,4}$, is negative.

Negative group delay dispersion

The analytical result for GDD using the Kostenbauder matrix formalism is exactly the same as that obtained by differentiating the phase introduced by a grating compressor (Eq. 3).

$$GDD_{grating} = -\frac{\lambda^3}{2\pi c^2} \frac{b}{d^2 \cos^2 \theta_d}\bigg|_{\lambda_0} \tag{3}$$

where θ_d is diffraction angle measured from the grating normal, b is the path length inside the compressor, and the grating groove spacing is d.

3.4.2 Single-grism pulse compressor

We also used Kostenbauder matrices to model the single-grism pulse compressor. The matrix for each pass through the grism can be obtained by treating it as a composite

optical element composed of a tilted air-glass interface, a reflection grating, and another tilted glass-air interface. Using the matrix for each grism pass, the Kostenbauder matrix for the compressor is given as:

$$K_c = K_{grism} K_{space} K_{grism} K_{mirror} K_{grism} K_{space} K_{grism} \tag{4}$$

The elements of the calculated matrix (Eq. 4) that correspond to spatiotemporal distortions are found to be all zeroes. The calculated Kostenbauder matrix shows that the spatial magnification $K_{c\,1,1}$ and angular magnification $K_{c\,2,2}$ are unity. Spatial chirp $K_{c\,1,4}$, angular dispersion $K_{c\,2,4}$ and pulse front tilt $K_{c\,1,3}$ are all zero. GDD $K_{c\,3,4}$ is negative. This shows that there is no spatial chirp, residual angular dispersion or pulse front tilt in the output of this device. Since the pulse travels equal distances inside the corner cube, the spatial chirp introduced in the first two passes is completely removed in the last two passes in the compressor. Therefore, there is no mismatch in the angle of incidence for the first two and last two passes of the pulse through the grism. This ensures that the angular dispersion is completely cancelled in the compressor.

3.5 Experiment

3.5.1 Group delay dispersion

In our experiments, a transform-limited pulse from a KM Labs Ti:Sapphire oscillator centered at 825 nm with a FWHM bandwidth of 30nm was stretched using the single grating pulse compressor. The corner cube consisted of silver coated mirrors and had an angular tolerance of 3 arc seconds. The angle of incidence of the input beam is 62

degrees from the grating normal. The phase introduced by the compressor was measured using SEA TADPOLE[29, 62] and a polynomial fit returned the GDD for varying separation of the corner cube and the grating (Fig. 6). The measured values of GDD were then plotted with the corner cube separation. The variation was found linear and in very good agreement with the simulations from the previous section.

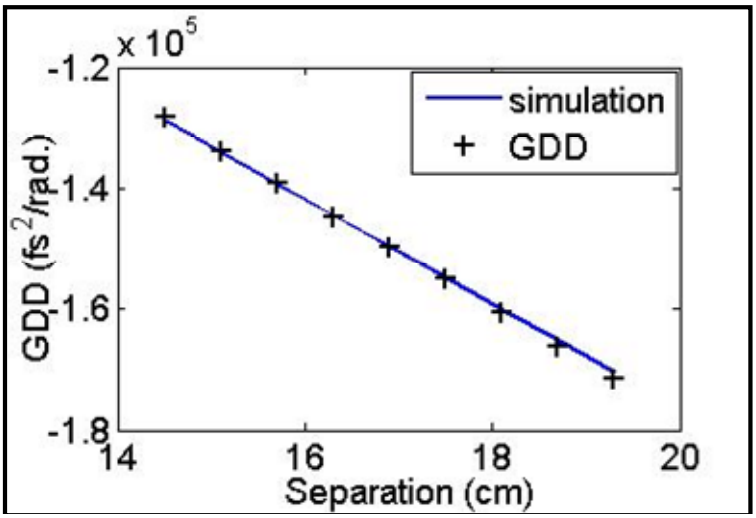

Fig. 3.6: Variation of GDD versus distance in single-grating pulse compressor.

Similarly, the dispersion introduced into the output pulse by the single-grism pulse compressor was also measured using SEA TADPOLE. The input pulse was centered at 800 nm with a bandwidth of 30nm. The incidence angle was fixed at 8.4 degrees from the grism surface normal. The GDD introduced by the compressor at each grism-corner cube separation is plotted below (see fig. 7).

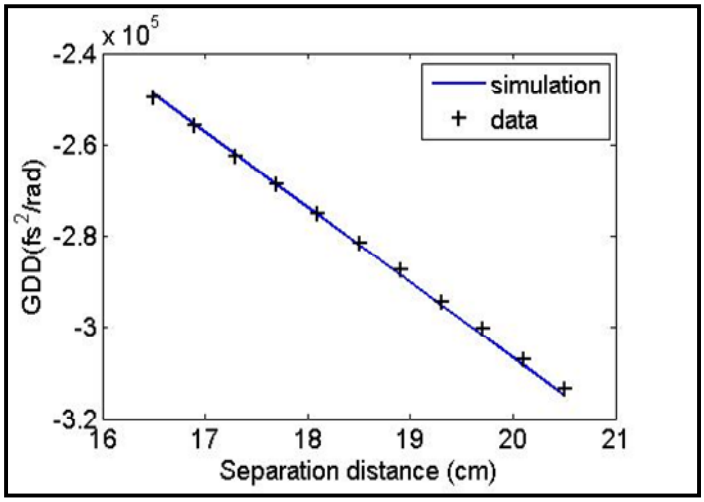

Fig. 3.7: GDD versus distance in the single grism pulse compressor.

3.5.2 Measurement of spatio-temporal distortions:

Spatial chirp:

The spatial chirp in the output pulse from the single grating compressor and the single grism compressor was measured experimentally using an imaging spectrometer[56]. The beam to be examined was dispersed in the direction of one of the beam's spatial co-ordinates, which was orthogonal to the one in which the beam was expected to have some spatial chirp, i.e., the dimension in which angular dispersion is introduced by the grating or the grism. The spatio-spectral plot below shows that there was almost no spatial chirp in the output beam from the single grating pulse compressor. The spatial chirp rho-parameter[51] calculated from the spatio-spectral plot shown (fig. 8) gave a value of 0.05, which is at the detection limit of our device. We obtained the same result for the single-grism pulse compressor.

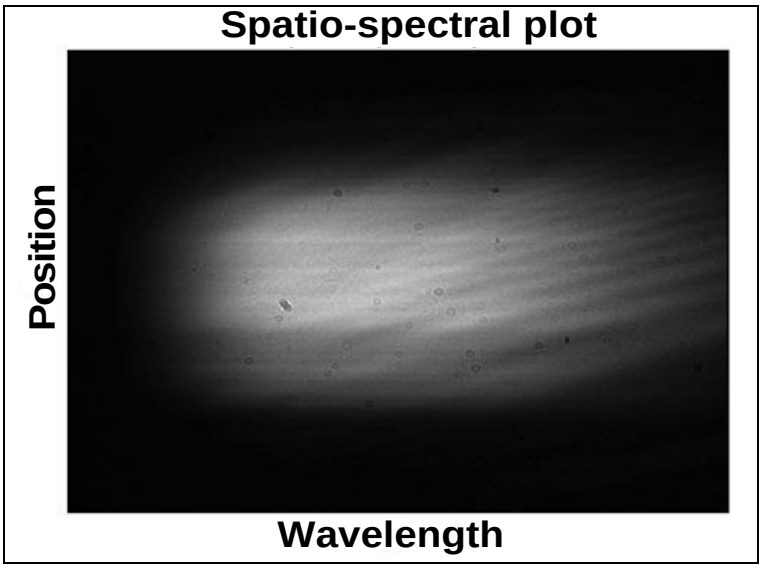

Fig. 3.8: Spatio-spectral plot revealing the lack of spatial chirp in the compressor output after four beam passes, indicated by the lack of tilt in this plot. The minor structure and the fringes at right are due to a stray reflection also entering the spectrometer and hence are of no significance.

Angular dispersion and pulse-front tilt:

The two compressors do not introduce any pulse front tilt or residual angular dispersion in the beam. It can be shown easily that residual angular dispersion, if present in the beam, will cause some spatial chirp to occur after propagating some distance after the compressor. Therefore, for measuring angular dispersion, it is a good check to measure spatial chirp at two different locations on the beam path after the beam exits the pulse compressor. Our measurements confirmed that there was no residual angular dispersion introduced by the two compressors. Absence of angular dispersion and spatial chirp simultaneously, guarantees that there is no pulse-front tilt in the beam either. Therefore, there are no spatiotemporal distortions introduced by the single grating and the single grism pulse compressors.

3.5.3 Third-order-dispersion compensation

To demonstrate third-order-dispersion compensation, a pulse from a Ti: Sapphire oscillator at a center wavelength of 805nm was stretched using a 10m long optical fiber. The input pulse before going through the fiber had a FWHM pulse width of 90fs and a spectral bandwidth of 30nm as measured by a GRENOUILLE. The spectral phase of the pulse after the fiber and before the compressor was also measured using SEA TADPOLE (see fig. 9). A fiber collimator attached to the end of this fused silica optical fiber collimated the beam, which then served as the input to the single-grism pulse compressor. The collimated beam was incident upon the grism at an angle of 8° from the grism surface normal. The curvature of the phase being monitored using SEA TADPOLE decreased as the corner cube was translated further back from the grism. After removing the second-order phase, minor adjustments in the incidence angle and corner-cube position yielded an almost flat-phase output pulse. The measured spectrum and the spectral phase of the output are shown below (Fig. 9). The spectral phase of the output shows that the dispersion introduced by the optical fiber was completely removed up to third order. Additionally, the compressor works for both horizontal and vertical polarizations. Neither the metal corner cube nor the roof mirror rotates the polarization of the beam, so the output beam maintains the same polarization as the input. However, gratings and grisms have different diffraction efficiencies for the two orthogonal polarizations, so use of an intermediate polarization would yield some polarization rotation.

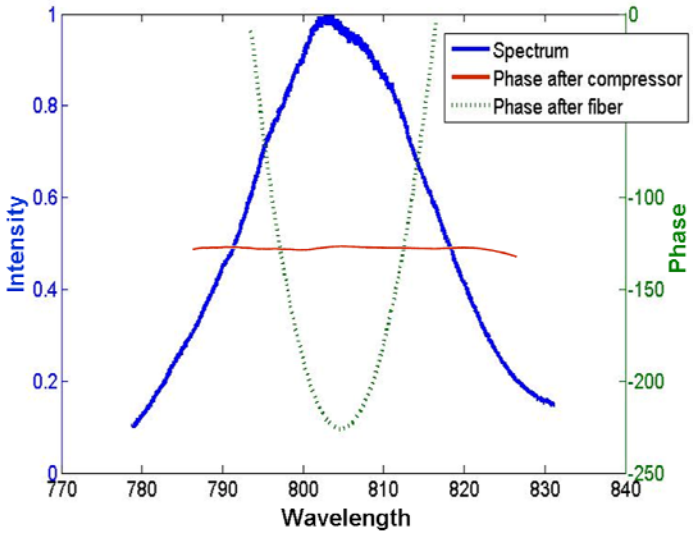

Fig. 3.9: Spectrum and spectral phase before and after the compressor.

3.6 Conclusion

In this work we have demonstrated that single-dispersive-element compressors have numerous advantages. They are easily aligned, automatically distortion free, one fourth or half the size of other equivalent compressors, and they can easily be tuned for varying amounts of GDD, GDD-to-TOD ratio, and the operating wavelength. The use of a grating as the dispersive element improves the ability to compensate for GDD by an order of magnitude compared to any prism compressor, while the single-grism pulse compressor should be of great utility when compensating for large amounts of material dispersion up to third order becomes necessary, for example, in fiber delivery of ultrashort pulses.

CHAPTER 4

Single prism/grating pulse compressor

4.1 Introduction

Due to their large bandwidths, ultrashort laser pulses are prone to numerous distortions, which can be spatial, temporal, or spatio-temporal in nature. Group-delay dispersion (GDD) is a temporal distortion, in which longer wavelengths propagate faster than shorter ones in the visible and near-IR, lengthening the pulse in time and reducing its peak intensity. It is therefore important to compensate for GDD in most applications of ultrashort pulses, such as imaging and micro-machining. Pulse compressors, using prisms or gratings as dispersive elements, can compensate for this effect because angular dispersion always yields negative GDD[53, 63, 64]. Unfortunately, introducing angular dispersion into a pulse also introduces other spatio-temporal distortions[50], such as pulse-front tilt and spatial chirp, which, along with the angular dispersion itself, must all be compensated before using the pulse. As a result, pulse compressors have two or four identical dispersive elements, arranged, not only to introduce negative GDD, but also to then compensate for these additional spatiotemporal distortions (see Fig.3.1).

This latter requirement entails the use of identical dispersive elements, operated at identical angles and identical separations. The traditional designs for pulse compressors are thus bulky and difficult to align for distortion-free output. For example, even in a two-prism pulse compressor (which double-passes a prism pair as shown in Fig. 3.2), the

two prisms must be identical and have identical incidence angles, or the output pulse will have residual angular dispersion, spatial chirp, and pulse-front tilt.

We recently introduced a *single-prism* pulse compressor that solved all of these problems for pulses with small to moderate amounts of GDD[58]. After the first and third passes through the prism, a precisely manufactured corner-cube retro-reflects and inverts the beam, obviating the need for additional prisms, and all these undesired distortions precisely cancel out (see Fig. 3.3). But prism compressors have limited negative GDD, and commonly occurring cases of massive GDD require more negative GDD. Use of a grating as the dispersive element provides up to 100 times more negative GDD for the same size compressor[59, 65]. So we extended the idea to single-grating compressors[45, 66, 67]. However, gratings have a negative ratio of third-order dispersion (TOD) to GDD, whereas all materials introduce a positive ratio, so this device, like other grating compressors, can exacerbate third-order dispersion.

A prism compressor in conjunction with a grating compressor has been shown to be able to compensate for higher-order dispersion, but such a complex apparatus is extremely difficult to align and maintain aligned[64], so this approach is rarely used. Another proposed solution to this problem uses off-axis and/or tilted lenses within a prism or grating compressor[68]. Unfortunately, the required lateral displacement and tilting of the lenses, important for tuning the higher-order dispersion in this design, can cause serious spatial aberrations and distort the beam's spatial profile. Use of a grism (a grating written on a prism) as the dispersive element achieves a variable ratio of third-to-second-order dispersion and so can solve this problem[69, 70]. So we have also extended our single-dispersive-element design to include a grism compressor. But grisms are

expensive, and the choice is restricted to only a very small number of commercially available parameters, which usually do not suit the requirements of the relevant experiments.

4.2 Single prism/grating pulse compressor

Obviously, one could, in principle, simulate a grism using a grating and prism combination and implement a prism/grating-combination compressor using two or four identical prism-grating combinations in a manner analogous to the grism compressor. However, this approach would be extremely difficult to align, so, despite its obviousness, it has not been reported or even attempted, to our knowledge. It becomes much easier to implement such an approach using the single-dispersive-element idea, yielding a pulse compressor that uses a single prism/grating combination. In our device, the prism and the grating are mounted together and they have a fixed relative separation and orientation. For GDD tuning only the corner cube needs to be translated and for ratio tuning the incidence angle of the input beam is varied. Indeed, it is quite trivial to set up and align our single-dispersive-element compressor containing only one grating and one prism.

A compressor using two prism-grating combinations has eight translational and four rotational degrees of freedom for alignment. The angular dispersion introduced by a prim-grating combination is generally more than just the sum of the individual dispersions added by each (see eq. 3). In compressors that use highly dispersive devices, a slight misalignment introduces large distortions. A simple calculation shows that 1-degree of angular mismatch, in a grating pair compressor that uses a pair of 1200 lines/mm gratings, causes a large angular dispersion (~ 0.9) in the pulse at the output and on propagating a few meters, significant spatial chirp (~ 0.5) and pulse front tilt (~ 0.5)

occurs. The value for each distortion was calculated in terms of normalized parameters introduced in[51]. In order to tune GDD and the TOD-to-GDD ratio, the prisms and the gratings have to be rotated and translated while maintaining the alignment, which is nearly impossible to achieve in practice.

Our design uses a roof mirror, a corner cube, a grating, and a dispersive prism. In our design, the beam quadruple-passes both of the dispersive elements and, like our previous single-dispersive-element designs, is automatically aligned for distortion-free output. It provides significantly more GDD than a prism compressor and, unlike a grating compressor, can tune the TOD-to-GDD ratio introduced. Additionally, this design allows the use of all available gratings and prisms, and thereby opens up the concept to an even wider range of applications. In our compressor, the tuning of GDD and the TOD-to-GDD ratio is remarkably easy, so it can compensate for material dispersion up to (and including) third order for a wide range of materials.

Figure 4.1 shows a schematic diagram of an implementation of the device that we built. The dashed line (shown on the top) shows the beam path as it undergoes total internal reflection at the oblique face of the prism and then exits from the face parallel to the reflection grating, kept at a distance of ~5mm from the prism. The first-order diffracted beam from the grating enters the prism again from the same face and finally exits from the oblique face. The beam is vertically displaced and reflected back in the same direction using a corner cube, which also reverses the spatial order of colors and inverts the beam for the second pass. Thus, as in other dispersive compressors, angular dispersion is removed after the first two passes, at which point, the beam only has spatial chirp, negative GDD and some pulse-front tilt. It is then reflected back onto the prism at a

different height using a roof mirror for the final two passes to cancel out the spatial chirp and pulse front tilt. The net effect is the addition of negative GDD and TOD, depending on the corner-cube position and the incidence angle of the beam.

We also performed numerical simulations of the single-prism-grating compressor in Matlab using the Kostenbauder-matrix formalism[49], and ray tracing.

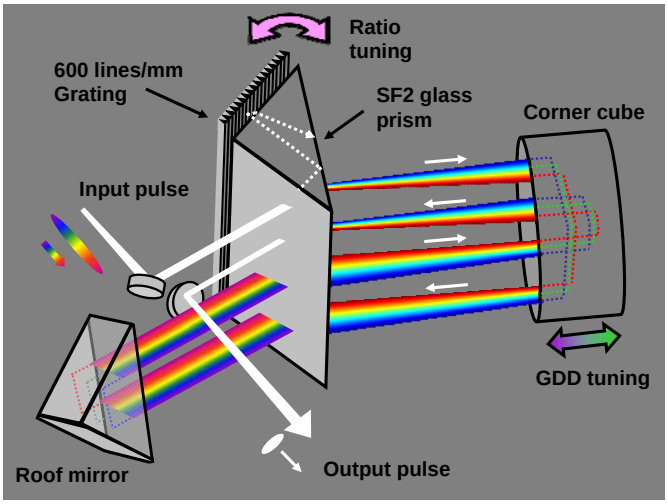

Fig. 4.1. Single prism/grating pulse compressor.

4.3 General characteristics of the compressor design

The GDD is mainly determined by the prism/grating combination and path between the first and second passes as in other grating compressors. Tuning of the TOD-to-GDD ratio is easily achieved by changing the incidence angle of the beam into the prism/grating combination or, equivalently, into the device as a whole. Using ray tracing, we calculated the angle of incidence for the correct TOD-to-GDD ratio. Its value depends on the prism shape, the prism material, and the grating used. Once the beam is aligned into the compressor at the correct angle, the prism-grating combination can then be rotated to fine-tune the ratio to the desired value. In our simulation, we found that, with a

variation of less than 4° in the input incidence angle, the ratio can be tuned from 0 to 1fs/rad (see Fig. 4.2).

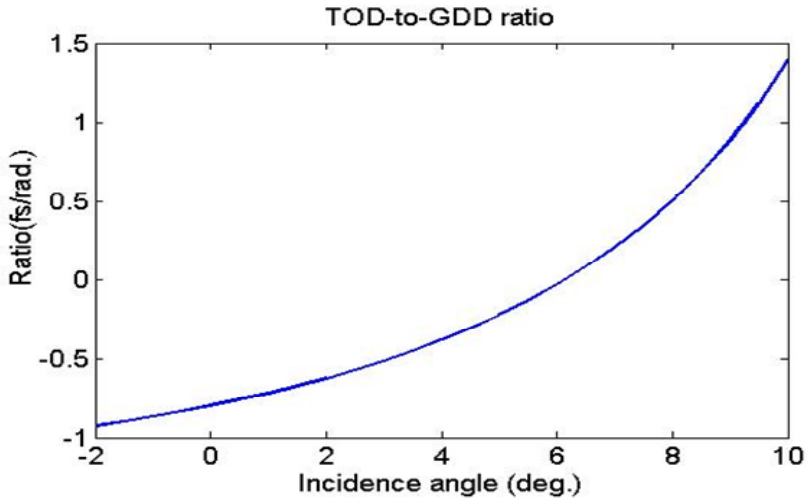

Fig. 4.2. Ratio variation with the incidence angle calculated using ray-tracing.

At 800nm, most materials introduce a ratio of 0.75fs/rad. So our compressor can compensate for dispersion up to third order for essentially all materials.

4.3.1 Beam magnification

Prisms have unity magnification at Brewster's angle incidence, designed to be the incidence angle for minimum deviation (i.e. when the input and output angles are equal). This is almost never in fact the case for any pulse compressor, as this condition is only met at one wavelength. Additionally, for TOD-to-GDD ratio tuning, the angle of incidence must be tuned in the device. Therefore, on the first pass through the prism-grating pair, the beam experiences one-dimensional spatial magnification. However, on the second pass through the two dispersive elements, the beam is reflected back from the corner cube and all the output angles now become the input angles, so it experiences a

demagnification by the same amount. Therefore, the overall beam magnification introduced by this compressor is unity as:

$$M_1 = \frac{1}{M_2} = M_3 = \frac{1}{M_4} \tag{4.1}$$

This result holds for all gratings and prisms. This is confirmed from the Kostenbauder matrix for this compressor, as the matrix elements corresponding to the spatial and angular magnification are both unity.

4.3.2 Spatiotemporal distortions

Propagation of a beam with angular dispersion not only increases the beam spot size in the transverse dimension of the angular dispersion, but also increases the pulse width significantly over a distance of a few meters and generates a large spatial chirp. Even a small misalignment in a compressor that uses a highly dispersive element, such as a grating, can distort the output pulse significantly. However, it is important that the output angular dispersion remain zero as the GDD and/or the TOD-to-GDD ratio is tuned. Because translating the corner cube to vary the GDD will not affect any device angles, it need not be considered—if the dispersion is zero for one value of GDD, it will be for them all. But we must verify that the variation of the incidence angle with ratio-tuning does not cause the output angular dispersion to be nonzero, as it easily can in current pulse compressors. The angular dispersion introduced by a prism-grating pair depends on which direction the beam propagates through it. Each pass through the prism-grating pair can be divided into three parts as the pulse goes through the prism (referred to as prism 1 in the section), the grating, and then the prism again (referred to as prism 2

in this section). The magnification M on each pass is just the product of the three individual magnifications.

$$M = M_{prism1} M_{grating} M_{prism2} \tag{4.2}$$

Let D be the dispersion introduced by a device. The dispersion introduced in the first pass through the prism-grating pair is given by a simple result[71, 72] that gives the total dispersion of an arbitrary sequence of dispersive devices in terms of only their dispersions and magnifications: the total dispersion is the sum of the individual dispersions, each divided by the total magnification that follows it:

$$D = \frac{D_{prism1}}{M_{grating} M_{prism2}} + \frac{D_{grating}}{M_{prism2}} + D_{prism2} \tag{4.3}$$

It is easy to show that, if a prism-grating pair has dispersion D and magnification M in the forward direction, it has dispersion MD in the reverse direction. Thus, after accounting for the beam inversion by the corner cube, the angular dispersion added on each pass through the prism-grating pair is:

$$MD_1 = -D_2 = -MD_3 = D_4 \tag{4.4}$$

To calculate the total dispersion added by the compressor, we again use the same result as in Eq. (3), but this time for a sequence of prism-grating pairs as they are visited by the pulse on each pass.

$$D_{tot} = \frac{D_1}{M_2 M_3 M_4} + \frac{D_2}{M_3 M_4} + \frac{D_3}{M_4} + D_4 \tag{4.5}$$

Substituting values from eqs. (1) and (4), it is seen that the total angular dispersion added by the device is precisely zero for all angles of incidence. Additionally, on constructing the Kostenbauder matrix for this compressor, it is easily seen that the angular dispersion, spatial chirp and pulse front tilt introduced by this compressor are all zero for all possible prisms and gratings.

4.3.3 Other Considerations

Additionally, like other dispersive compressors, this design works for both horizontal and vertical polarizations. Neither the metal corner cube nor the roof mirror rotates the polarization of the beam, so the output beam maintains the same polarization as the input. However, gratings and prisms have different diffraction efficiencies for the two orthogonal polarizations, so use of an intermediate polarization would yield some polarization rotation.

4.4 Experiment

Our prism was composed of SF2 glass and had an apex angle of 90° and an input face 5 cm × 5 cm. The beam angle of incidence on the prism was 8° from the prism normal. The beam underwent the total internal reflection shown in Fig. 4, but this does not change the device properties, and it generated a conveniently located output beam. Our 5-cm long grating was reflective and had 600-lines/mm. The beam incidence angle on the grating was 8° and the (first-order) diffracted beam emerged at 20° from the grating normal. The prism and the grating were mounted together on a rotation stage, and the grating was kept parallel to the prism at a distance of about ~5mm (this value was chosen for experimental convenience and does not alter the TOD-to-GDD ratio). The

corner cube consisted of silver-coated mirrors and had an angular tolerance of 3 arc-seconds. Its diameter was 63.5 mm. It was placed after the prism/grating combination to reflect the diffracted beam back toward it, as in Fig. 4.

Transform-limited pulses from a KM Labs Ti:Sapphire oscillator, centered at 805nm with a FWHM bandwidth of 30nm, were stretched (by down chirping) using our pulse compressor. We measured the phase introduced by the compressor using SEA TADPOLE, and a polynomial fit returned the GDD introduced at each position of the corner cube. The GDD values thus obtained were plotted with the corner cube separation as shown in Fig. 6. The variation was found linear and in very good agreement with the theory.

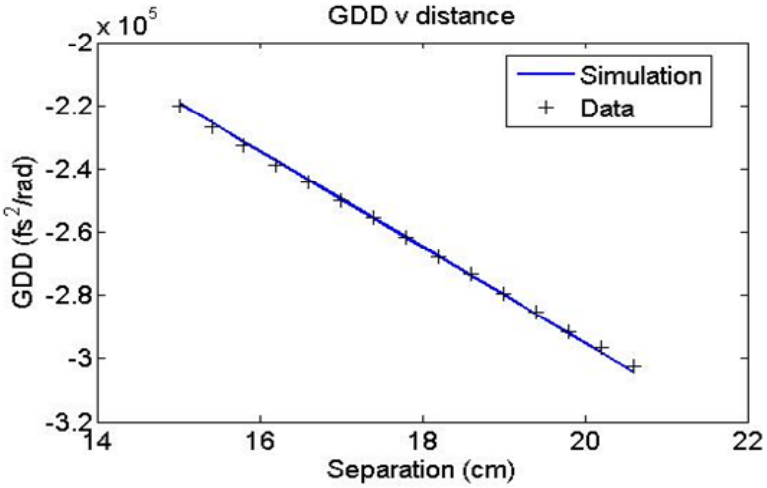

Fig. 4.3. GDD variation with corner cube separation.

In order to verify the lack of spatio-temporal distortions, we examined the output beam by looking at the spatio-spectral plot $I(x,\omega)$ at the output of a spectrometer. Any noticeable tilt in this 2-D plot would be indicative of some spatial chirp[56] in the output, but no tilt was observed in the plot (see Fig. 7). Using this plot, we calculated a dimensionless parameter, ρ, which is a very sensitive measure for spatial chirp at small

values[51]. The spatial chirp measured was <0.02, which is at the detection limit of our measurement.

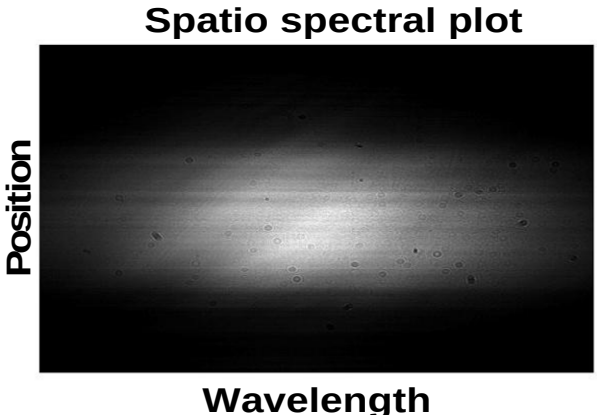

Fig. 4.4. Spatio-spectral plot of the output pulse.

To measure the residual angular dispersion, a lens was introduced in the output beam to map angles to position at the slit of an imaging spectrometer. A similar plot was obtained for $I(k_x,\omega)$, and the ρ-value for angular dispersion was also at the detection limit. In the absence of spatial chirp and angular dispersion, pulse front tilt is also necessarily absent in a beam. We conclude that, as predicted, there were no spatio-temporal distortions in the output beam.

In order to demonstrate third-order dispersion compensation, a pulse from a Ti:Sapphire oscillator at a center wavelength of 805nm was stretched using a 12m long optical fiber. The somewhat chirped input pulse coupled into the fiber had a FWHM pulse width of 90fs and a spectral bandwidth of 30nm, as measured by a Swamp Optics GRENOUILLE(model 8:50 USB)[73]. The input pulse chirp does not interfere with our measurements. Using SEA TADPOLE[29], we measured the phase difference between the stretched pulse after the fiber and the input pulse which is used as the reference. This

tells us the spectral phase added by the optical fiber alone (see fig. 8). After the fiber, the beam was collimated by a fiber collimator and sent into the compressor. The second-order spectral phase of the output pulse after the compressor was monitored using SEA TADPOLE and decreased as the corner cube was translated further from the grating/prism combination. After removing the second-order phase, minor adjustments in the incidence angle and corner-cube position yielded an almost flat phase (see Fig. 8). The spectral phase of the output pulse shows that the dispersion introduced by the optical fiber was completely removed up to and including third order. The residual phase is mostly quartic as is evident from the plot below.

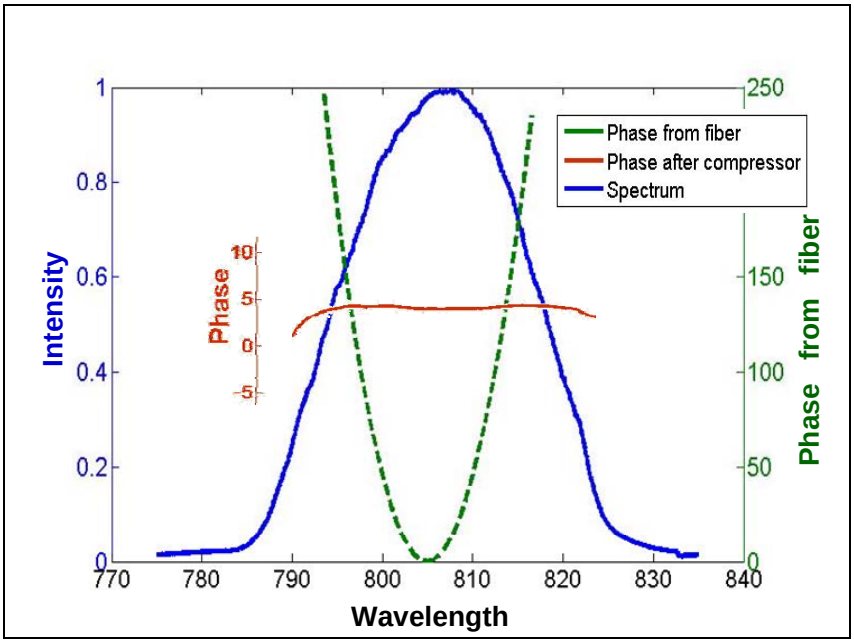

Fig. 4.5. Spectrum of the pulse after going through the fiber and the compressor. The spectral phase shown in green is the phase added to the pulse by 12 meters of fused silica fiber. The pulse after the fiber goes through the compressor which compensates for almost all of the GDD and TOD that was added by the fiber. The phase shown in red is the phase of the final output pulse, after both the compressor and the fiber, with reference to the input pulse.

4.5 Discussion

Because only one set of dispersive components need be aligned in this device, one need not stop at the use of two components in this design. As a result, it paves the way for even higher-order dispersion compensation by adding as many dispersive elements (of any kind and at any angle) as one chooses without a significant increase in complexity. And because the achievable GDD scales as the square of the total dispersion, one could increase the achievable GDD by a large factor by simply adding more easily aligned dispersive elements.

4.5.1 Additional prism/grating combinations

In the prism/grating compressor that we used for performing experiments, the input ray makes an angle of ~8^{o} with the input face normal. At the other incidence angles, within a range of ~2^{o}, the TOD-to-GDD ratio remains positive; this is the range of angles for material dispersion compensation. Outside this range the TOD is either negative or is too high and thus over compensates for material dispersion. Aligning the beam into the compressor is much convenient at a normal incidence. There are some alternative combinations that can be made from off-the-shelf components and have other additional desired properties. One such alternative prism/grating combination is a right angled SF11 prism and 600 lines/mm grating. In simulations, it was found that the compressor with this prism/grating dispersive element has 0^{o} +/- 2^{o} as the range for material dispersion compensation. It should also improve the efficiency as the exit ray angle after one pass through the prism/grating combination equals the Brewster angle, 60^{o} from the normal.

Another prism/grating combination with normal incidence for TOD operation is an equilateral fused silica prism and a 672 lines/mm grating, the beam path is shown below in fig. 4.6. For a lower value of GVD/cm of separation, a 40^{o} SF10 glass prism with a 300 lines/mm grating can be used see the figure below for beam path through the device.

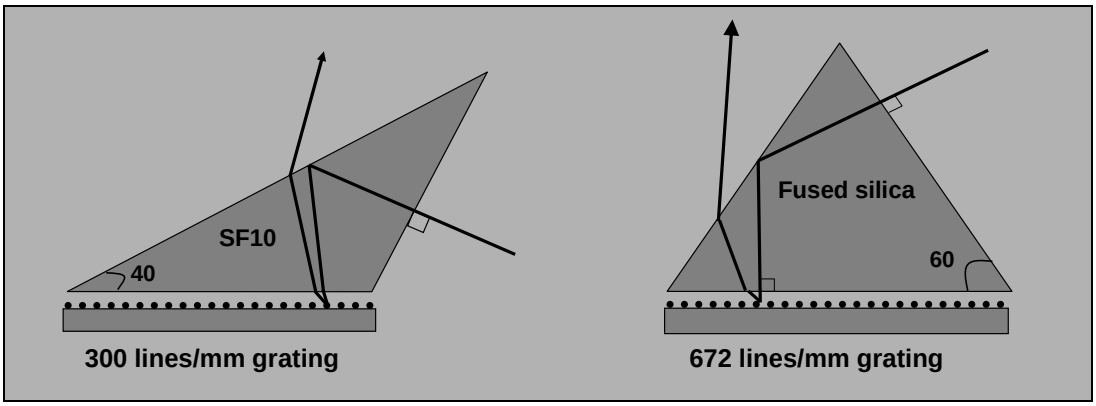

Fig. 4.6: Prism/grating combinations for TOD control.

4.6 Conclusion

In conclusion, we have developed a simple, elegant, and versatile pulse compressor that has all the benefits of a single-grism pulse compressor. It adds significantly more negative GDD than a prism-based compressor and compensates for TOD as well—but avoids the need for difficult-to-obtain grisms. Our design is very easy to tune for TOD-to-GDD ratio and dispersion, and it is very compact—about a fourth or a half the size of previous designs. It automatically yields zero angular dispersion, zero spatial dispersion, zero pulse-front tilt, and unity magnification. It should be useful for many purposes, including pre-compensating for fiber-induced chirp, so that one Ti:Sapphire laser could supply transform-limited pulses through equal-length fibers to multiple experimental set ups in many different rooms.

CHAPTER 5

SIMPLE DISPERSION LAW FOR ARBITRARY SEQUENCES OF DISPERSIVE OPTICS

5.1 Sequences of dispersive elements

Multiple dispersive elements in sequence are commonly used for beam magnification and wavelength tuning in lasers[72, 74-78], ultrashort-laser-pulse compression[45, 55, 58, 63, 64, 79, 80], and applications in which a single element yields too little or too much angular dispersion or magnification. Also, many devices involve the use of multiple passes through a single dispersive element or combinations of elements[45, 55, 58]—effectively the same problem.

Unfortunately, formulae in the literature for modeling these devices are quite complex and unintuitive, and they cannot be generalized to cover all the dispersive elements; see, for example, reference[81].

Here we present a very simple equation for the total angular dispersion introduced by a sequence of arbitrary dispersive elements, such as prisms, gratings, and etalons, in terms of their respective angular dispersions and spatial or angular magnifications, which seems to have escaped notice in the literature and textbooks[82-89]. It is a generalization of a result first obtained by Trebino for a sequence of prisms[72]. We derive this more general result using the Kostenbauder-matrix formalism[49]. In addition, we use it to

model a prism-grating pulse compressor, in which a prism and grating are quadruple-passed—an otherwise prohibitively difficult problem.

5.2 Theory

We first note that the expression for the dispersion, D, of a single general prism is:

$$D = \left[\frac{dn}{d\lambda} \frac{\sin(\phi)}{\cos(\theta)} \Big/ \frac{\cos(\gamma)}{\cos(\beta)} \right] + \frac{dn}{d\lambda} \frac{\sin(\beta)}{\cos(\phi)} \tag{5.1}$$

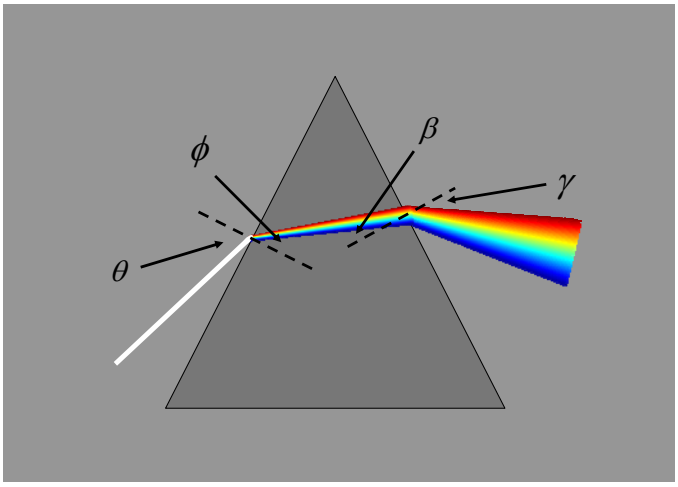

Fig 5.1. A prism, a beam, and their relevant angles; dashed lines are normals to the prism faces.

where n is the refractive index, λ is the wavelength, θ is the incidence angle of the beam at the entrance face, ϕ is the transmitted angle of the beam at the entrance face, β is the incidence angle of the beam at the exit face, and γ is the transmitted angle of the beam at the exit face. Noticing that $\cos(\gamma)/\cos(\beta)$ is the beam spatial magnification at the exit face, and the other quantities are the dispersions at the two individual faces, this expression can be rewritten very simply as the sum of the dispersions at the first (d_1) and

second (d_2) faces, but with that of the first face divided by the spatial magnification that occurs at the second (m_2).

$$D = \frac{d_1}{m_2} + d_2 \tag{5.2}$$

In fact, the same is true for the dispersions and magnifications of sequences of whole prisms, and Trebino has shown (by simplifying an expression in reference written in terms of the angles) that the total dispersion due to a sequence of N prisms is given by:

$$D_{total} = \frac{D_1}{M_2 M_3 \cdots M_N} + \frac{D_2}{M_3 M_4 \cdots M_N} + \cdots + D_N \tag{5.3}$$

where D_i and M_i are the angular dispersion and spatial magnification of the i^{th} prism, respectively. In this expression and in what follows, the dispersion is taken to be negative if the element is inverted.

We can easily generalize this expression to arbitrary numbers of arbitrary dispersive elements. To do so, recall that the propagation of an ultrashort pulse through a sequence of dispersive devices can be modeled using the Kostenbauder matrix (K-matrix) formalism. In this formalism, each of the dispersive elements is represented by a 4×4 ray-pulse matrix, analogous to the well-known 2×2 ray-matrix formalism for geometrical optics, but now including time and frequency, in addition to position and angle. K-matrices also allow for spatio-temporal distortions, such as angular dispersion. An entire optical system consisting of multiple geometrical and dispersive elements can be described by the product of the individual 4×4 K-matrices.

In general, a K-matrix for a linear, time-invariant, and non-focusing dispersive device will have certain elements that are always zero and one, as shown by Kostenbauder. The other matrix elements depend on the device parameters. These matrix elements correspond to the magnification (M), position vs. angle (B), dispersion (D), spatial chirp (E), group-delay dispersion (I), time vs. angle (H), and the pulse-front tilt (DM/λ_0) introduced by the optic.

$$K = \begin{bmatrix} M & B & 0 & E \\ 0 & 1/M & 0 & D \\ DM/\lambda_0 & H & 1 & I \\ 0 & 0 & 0 & 1 \end{bmatrix} \tag{5.4}$$

Consider first a grating as the dispersive element. The beam magnification by the grating is given in terms of the incidence angle, ψ_i, and the diffraction angle, ψ_d, both measured from the surface normal.

$$M = -\frac{\cos\psi_d}{\cos\psi_i} \tag{5.5}$$

The angular dispersion introduced by a grating is given by

$$D = \frac{\sin\psi_d - \sin\psi_i}{f_0 \cos\psi_d} \tag{5.6}$$

where f_0 is the center frequency of the pulse in cycles per second.

In terms of these quantities, the K-matrix for a grating is:

$$K_{grating} = \begin{bmatrix} M & 0 & 0 & 0 \\ 0 & 1/M & 0 & D \\ DM/\lambda_0 & 0 & 1 & 0 \\ 0 & 0 & 0 & 1 \end{bmatrix} \tag{5.7}$$

Now consider a pulse diffracted by N gratings sequentially. In the following, we omit the K-matrices representing free-space propagation because they add no angular dispersion or magnification, and therefore contribute nothing to the quantities of interest. The K-matrix representing this system is obtained by multiplying together the matrices of each individual grating:

$$\begin{bmatrix} M_N & 0 & 0 & 0 \\ 0 & 1/M_N & 0 & D_N \\ D_N M_N/\lambda_0 & 0 & 1 & 0 \\ 0 & 0 & 0 & 1 \end{bmatrix} \cdots \begin{bmatrix} M_1 & 0 & 0 & 0 \\ 0 & 1/M_1 & 0 & D_1 \\ D_1 M_1/\lambda_0 & 0 & 1 & 0 \\ 0 & 0 & 0 & 1 \end{bmatrix} =$$

$$\begin{bmatrix} \prod_{n=1}^{N} M_n & 0 & 0 & 0 \\ 0 & 1/\prod_{n=1}^{N} M_n & 0 & \sum_{n=1}^{N} D_n / \prod_{p=n+1}^{N} M_p \\ \sum_{n=1}^{N} D_n \prod_{p=1}^{n} M_p / \lambda_0 & 0 & 1 & 0 \\ 0 & 0 & 0 & 1 \end{bmatrix} \tag{5.8}$$

This expression can easily be proven using mathematical induction.

From the above K-matrix for the system of gratings, the total dispersion is given as

$$D_{total} = \sum_{n=1}^{N} \frac{D_n}{\prod_{p=n+1}^{N} M_p} \tag{5.9}$$

which is the dispersion expression for multiple prisms first derived by Trebino.

Next, we generalize this result to an arbitrary sequence of potentially different dispersive devices (see Fig. 2), including arbitrary prisms, reflection or transmission gratings, tilted interfaces, or etalons.

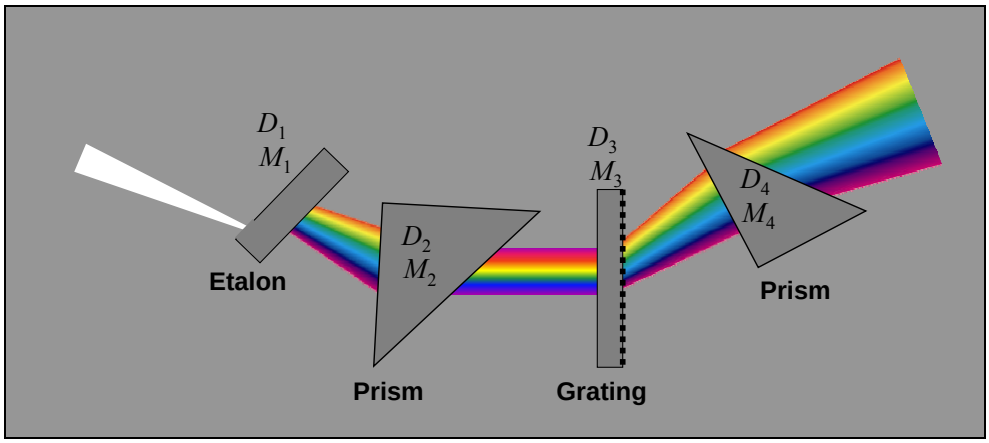

Fig. 5.2. A sequence of dispersive optics with their respective dispersions and magnifications

As before, the K-matrix for the entire system of dispersive elements is given by the product of the K-matrices of each individual element. In this product, we again ignore the free-space propagation between the elements because it does not contribute any dispersion or magnification. This calculation is shown below, and as before it can be proven by mathematical induction.

$$\begin{bmatrix} M_N & B_N & 0 & E_N \\ 0 & 1/M_N & 0 & D_N \\ D_N M_N/\lambda_0 & H_N & 1 & I_N \\ 0 & 0 & 0 & 1 \end{bmatrix} \cdots \begin{bmatrix} M_1 & B_1 & 0 & E_1 \\ 0 & 1/M_1 & 0 & D_1 \\ D_1 M_1/\lambda_0 & H_1 & 1 & I_1 \\ 0 & 0 & 0 & 1 \end{bmatrix} =$$

$$\begin{bmatrix} \prod_{n=1}^{N} M_n & B_{total} & 0 & E_{total} \\ 0 & 1/\prod_{n=1}^{N} M_n & 0 & \sum_{n=1}^{N} D_n / \prod_{p=n+1}^{N} M_p \\ \sum_{n=1}^{N} D_n \prod_{p=1}^{n} M_p / \lambda_0 & H_{total} & 1 & I_{total} \\ 0 & 0 & 0 & 1 \end{bmatrix} \tag{5.10}$$

Examining the elements of the above matrix, we see that the total magnification and angular dispersion of the system are given by:

$$M_{total} = M_1 M_2 M_3 \cdots M_N \tag{5.11}$$

and

$$D_{total} = \frac{D_1}{M_2 M_3 \cdots M_N} + \frac{D_2}{M_3 M_4 \cdots M_N} + \cdots + D_N \tag{5.12}$$

Finally, we note that the beam *angular* magnification, $\mu_i = 1/M_i$, is the reciprocal of the spatial magnification, so this expression can be written perhaps even more simply and intuitively in terms of this latter quantity as:

$$D_{total} = D_1 \mu_2 \mu_3 \cdots \mu_N + D_2 \mu_3 \mu_4 \cdots \mu_N + \cdots + D_N \tag{5.13}$$

This is quite intuitive, since the angular dispersion undergoes angular magnification at the later elements. We caution the reader that other elements of the combined system cannot be obtained from our analysis (Eq. (10)) unless they do not depend on the separations between the elements, as we have neglected the relevant propagation matrices between the elements.

5.3 Example: Modeling of single-prism-grating pulse compressor

As an example, we can use eqs. (11) and (12) to determine the magnification and angular dispersion introduced by a recently developed pulse compressor that involves quadruple-passing a prism and grating. See Fig. 4.1.

A single-prism-grating compressor uses a combination of a prism and a reflection grating as the dispersive element. After the first pass through both of these elements, the beam is reflected precisely back using a corner cube, which inverts the beam and displaces it vertically for the second pass. After the first two passes, a roof mirror returns the beam for its final two passes in the same fashion. In all, the device involves four passes through the grating and eight though the prism. Each pass through the prism-grating pair can be divided into three parts as the pulse goes through the prism (referred to as prism 1 in this section), the grating, and then the prism again (referred to as prism 2 in this section). The magnification M on each pass is just the product of the three individual magnifications.

To perform this calculation, we note that inverting the beam or inverting the dispersive device induces sign reversals of certain elements in the corresponding

Kostenbauder matrix, including those for the added spatial chirp, angular dispersion, pulse-front tilt and time vs. angle.

$$\begin{bmatrix} M & B & 0 & E \\ 0 & 1/M & 0 & D \\ DM/\lambda_0 & H & 1 & I \\ 0 & 0 & 0 & 1 \end{bmatrix} \rightarrow \begin{bmatrix} M & B & 0 & -E \\ 0 & 1/M & 0 & -D \\ -DM/\lambda_0 & -H & 1 & I \\ 0 & 0 & 0 & 1 \end{bmatrix} \tag{5.14}$$

From Eq. (11) the magnification of each prism-grating combination is given by

$$M = M_{prism1} M_{grating} M_{prism2} \tag{5.15}$$

The angular dispersion D introduced on the first pass through the prism-grating pair is given by the dispersion equation, Eq. (12), which yields

$$D = \frac{D_{prism1}}{M_{grating} M_{prism2}} + \frac{D_{grating}}{M_{prism2}} + D_{prism2} \tag{5.16}$$

Please refer to section 4.3.2 of the previous chapter, equation 4.1 through 4.5 for the remaining steps in the derivation.

5.4 Conclusions

In conclusion, we have shown that the total angular dispersion due to multiple dispersive elements is the sum of the individual dispersions, with each divided by the total magnification occurring afterward (or multiplied by the total angular dispersion occurring afterward). This simple result yields a more intuitive understanding of the

dispersive properties of several dispersive elements when used together and should greatly simplify the modeling of devices containing such elements.

CHAPTER 6

SIMULTANEOUSLY RETRIEVING TWO PULSES FROM SINGLE-SHOT PG-XFROG

6.1 Introduction:

Often in ultrafast-optical experiments, simultaneous characterization of two pulses is necessary. For example, in the characterization of materials, both input and output pulses must be known to measure the desired material properties. Also, measuring exotic-wavelength pulses usually requires a well-characterized reference pulse at a different wavelength, thus also yielding a two-pulse-measurement problem. The same is true for very complex pulses (such as continuum), which are best measured using a previously characterized simple reference pulse. As a result, a technique that can simultaneously measure two different pulses (of potentially different wavelengths) would be very useful. A method has been proposed, in which the two unknown pulses gate each other in a nonlinear medium and the spectrally resolved signal pulse generates a FROG trace in the usual manner, called Blind FROG (in reference to its mathematical background involving "blind deconvolution"). Blind FROG attempts to retrieve two pulses from a single FROG trace, and an additional measurement of spectrum is required to achieve convergence. But due to the two different unknown pulses, there are many nontrivial ambiguities [90, 91] and so Blind FROG is not generally useful.

Here we show that a technique, originally proposed by Trebino[92], but never considered, which we call Double-Blind FROG, does in fact nicely solve this problem. Unlike other FROG variants, in which only one FROG spectrogram is measured, in Double-Blind FROG *two* traces are measured, one in which one pulse gates the other, and another in which the other pulse gates the one. The generation of two signal pulses, and hence two different traces, is straightforward in the polarization-gating (PG) and self-diffraction versions of FROG, and no modifications to the standard FROG algorithm are required. Even better, it operates on a single-shot basis.

6.2 Double-Blind PG FROG

The double-blind technique implemented with PG FORG inherits all the advantages of PG FROG, which has the most intuitive FROG traces out of all of the FROG techniques, and it has many other desirable qualities. First, and most importantly, there are no ambiguities in PG FROG. Thus, PG FROG determines the complete and non-ambiguous pulse intensity and phase in all known cases. A second advantage of PG FROG is that the nonlinear-optical process is automatically phase-matched, which allows for large crossing angle leading to large delay ranges in a single shot geometry. The second advantage results in two consequences: (1) alignment is easy; and (2) PG FROG is capable to measure pulses with extremely large bandwidth and/or very complex pulses. But some disadvantages exist too. For example, PG FROG requires high-quality polarizers to get a high extinction ratio of at least $1{:}10^{-5}$, and these are often thick, so they introduce some material dispersion and change the pulse parameters. However, this is usually not a serious problem if pulse being measured has a center frequency in the

visible or near IR region, and finally, the effect of polarizers can be taken into account at the end of the experiment and the pulse can be simply back-propagated to get the input pulse.

A Double-Blind PG FROG experimental setup is similar to a PG XFROG setup, except for the second imaging spectrometer and an additional -45° polarizer. The two unknown pulses gate each other in a $\chi^{(3)}$ nonlinear medium, such as fused silica. Pulse 2 is 0°-polarized and pulse 1 is 45°-polarized, with respect to the horizontal plane. The induced refractive index change in fused silica by pulse 1 is seen as induced birefringence by pulse 2, which causes time-gated polarization rotation in it. By the same mechanism, pulse 2 causes a time-gated polarization rotation in pulse 1. Mathematically, the two traces in Double-Blind PG FROG are:

$$I_1(\omega,\tau) = \left| \int E_1(t) \left| E_2(t-\tau) \right|^2 e^{-i\omega t}\, dt \right|^2 \tag{1}$$

And

$$I_2(\omega,\tau) = \left| \int E_2(t) \left| E_1(t-\tau) \right|^2 e^{-i\omega t}\, dt \right|^2 \tag{2}$$

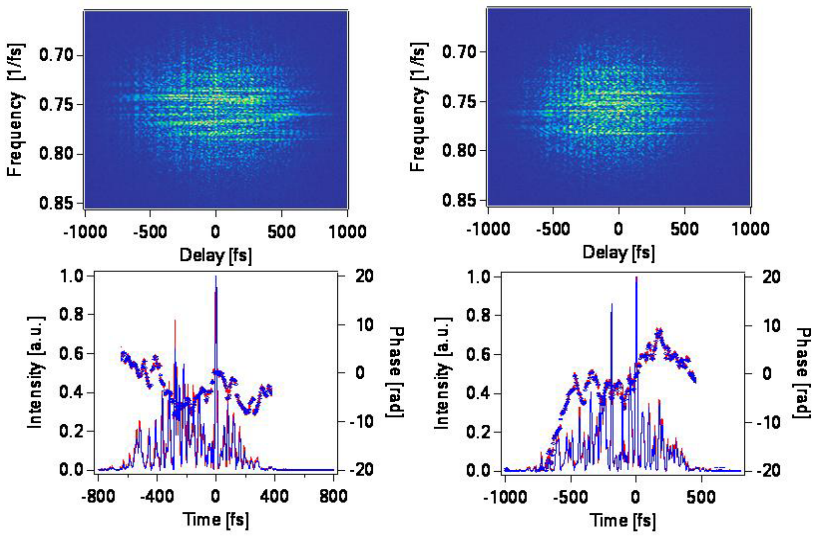

Fig. 6.1. Double-Blind Polarization-gate FROG traces (above) and pulses corresponding to them (bottom, blue) in a simulation using two complex pulses. In this simulation, 1% additive noise has been added to the traces, and convergence still occurs. The bottom figures also show the retrieved pulse in time and frequency (red). Note the excellent agreement, despite the complexity. So far, we have not found a case in which convergence does not occur for Double-Blind PG FROG, even in the presence of such noise (fig. borrowed from measurement of complex ultrashort laser pulses using frequency resolved optical gating).

Next, the standard generalized-projections XFROG iterative phase-retrieval program (in which one pulse is assumed to be known) is used to retrieve full intensity-and-phase information, alternately for $E_1(t)$ assuming that $E_2(t)$ is known and then vice versa. Only a few iterations are performed in each cycle. In each cycle, generalized projection XFROG is used to find a better estimate for $E_1(t)$ using trace 1, i.e. $I_1(\omega,\tau)$. Then after a few iterations, a better guess for $E_2(t)$ is obtained using trace 2, i.e. $I_2(\omega,\tau)$. The results for $E_1(t)$ and $E_2(t)$ thus obtained are used as initial guesses for the next cycle. This process is repeated in our algorithm until the resulting PG double-blind FROG traces match the experimentally measured trace or the minimum error is reached. Before running the algorithm on the traces we perform standard noise deduction steps and background subtraction. The convergence of the algorithm is defined using FROG errors, just like in other FROG techniques.

Fig. 6.2: Each cycle during pulse retrieval in Double-blind PG FROG.

We found this process to be remarkably reliable. In simulation, we were able to retrieve two extremely complex pulses from two PG XFROG traces generated using them. We also added 1% Poisson noise to this case.

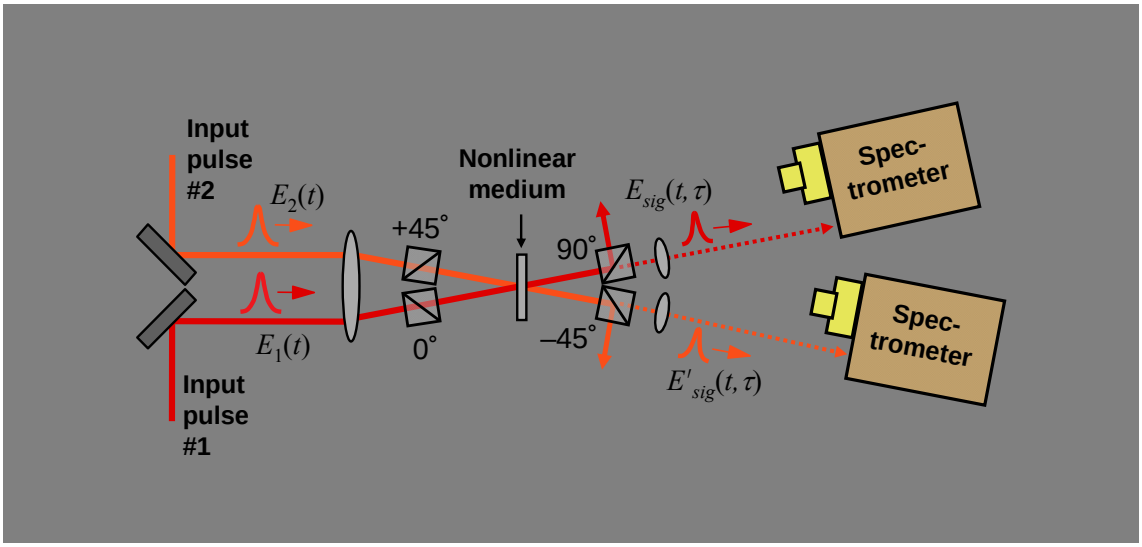

Fig. 6.3: The schematics of a single shot double-blind PG FROG (fig. borrowed from Ultrafast Optics lectures: by Rick Trebino).

6.3 Experiment

In this experiment two 5mm-wide beams with 100 fs pulse trains centered at 805 nm from a regenerative amplifier (*Coherent Legend*) are crossed at an angle of 6^{o} in a fused silica glass plate of 250um thickness. This crossing angle and the beam diameter correspond to a total delay range of 1.5ps. In single shot geometry, like the one being used in our experiment, there is always some temporal broadening of the signal associated with the thickness of the nonlinear medium used, so a thinner glass plate is better. But the signal yield decreases on decreasing the thickness of the nonlinear medium, so thicker glass plates are better for this reason. We found that the use of 250um fused silica plate provided a high enough signal yield and not so significant trace broadening of ~10 fs. Figure 3 describes the schematics of PG-Double-Blind FROG setup.

Beam 1 goes through a 0^{o} polarizer and is focused to a line using a cylindrical lens of 100mm focal length, in the glass plate. This beam is then collimated using another identical cylindrical lens, and then blocked by a 90^{o} polarizer. Similarly, beam 2 passes through a 45^{o} polarizer and is focused using the same cylindrical lens in the glass plate where it spatially overlaps with beam 1 and crosses with it in the horizontal plane at an angle of 6^{o}. This beam, after going through the same collimating lens as beam 1, is blocked by a -45^{o} polarizer. In the absence of temporal overlap of the pulses from the two beams, no signal can be obtained. We use a delay stage in one of the beam path to obtain temporal overlap between the crossing pulses, and there upon the cross-correlation signal beam appears behind the cross-Polarizers in both of the beam paths. For the experimental

convenience, we rotate the transverse spatial co-ordinates of the beams by 90^{o} after the cross polarizers in both the beams using a periscope, thus the signal now has the delay-axis pointing in vertical direction. Cylindrical lenses of 300mm focal length each are used in both of the signal beams to image the delay-axis in the glass plate on to the camera. After the imaging lens, a 600 lines/mm grating and a 100mm cylindrical lens, spectrally resolve the cross-correlation signal, and two PG XFROG traces are obtained on the two cameras.

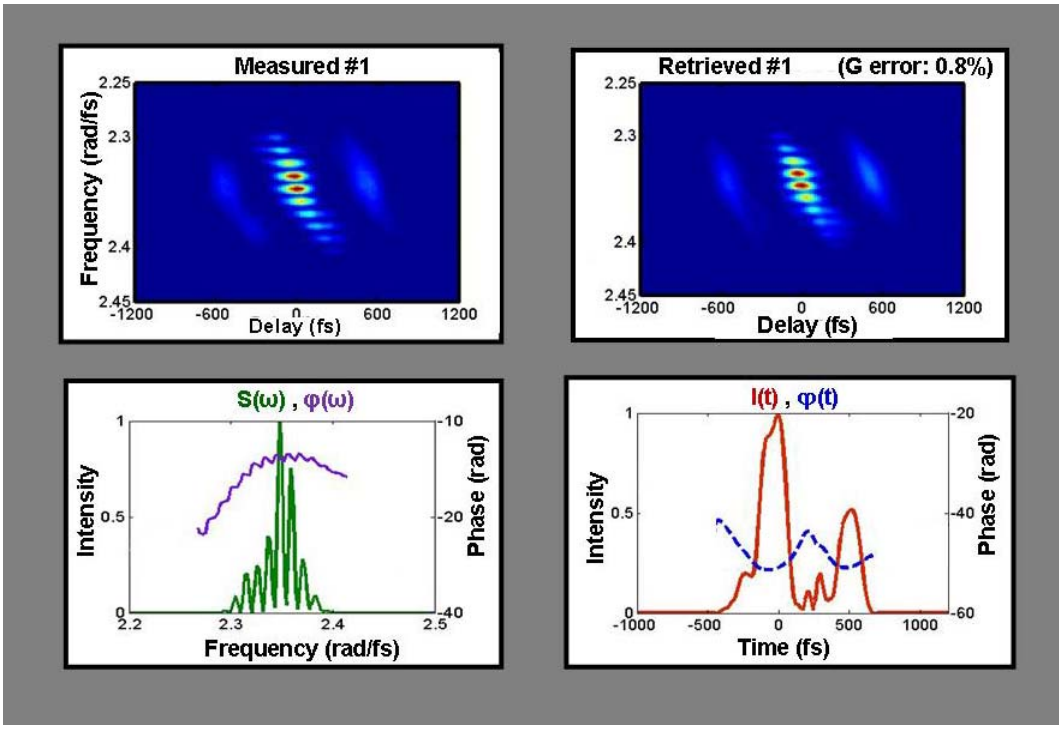

Fig. 6.4: Clockwise from top left: Measured trace 1 for the double pulse, the reconstructed trace, the intensity and phase in time, and the spectrum and spectral phase for pulse1.

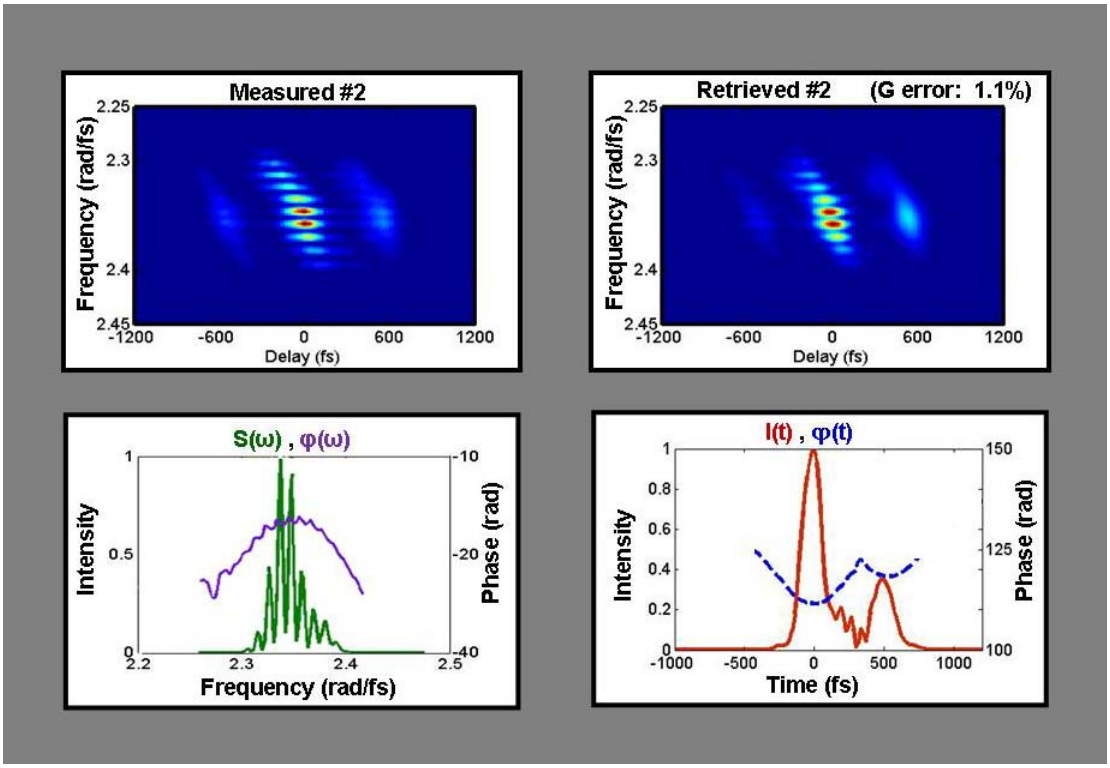

Fig. 6.5: Clockwise from top left: Measured trace 1 for the double pulse, the reconstructed trace, the intensity and phase in time, and the spectrum and spectral phase for pulse2.

Using the two traces and the above algorithm, we were able to retrieve both pulses (see Figs. 6.4 and 6.5). The separation between the peaks was 526 fs in double pulse 1 and 518 fs in double pulse 2. Using an ocean optics spectrometer the temporal separation was found to be 516 fs. The discrepancy lies well within the error margins due to calibration errors. Figure 6.6, and 6.7 show the measurement of two pulses which were chirped by different amounts. One of the pulses goes through a 2cm thick window of SF11 additionally. The pulses were measured as 248fs and 180fs respectively.

6.4 Conclusion

We have demonstrated single shot and simultaneous retrieval of two different pulses. This method should find use in numerous applications.

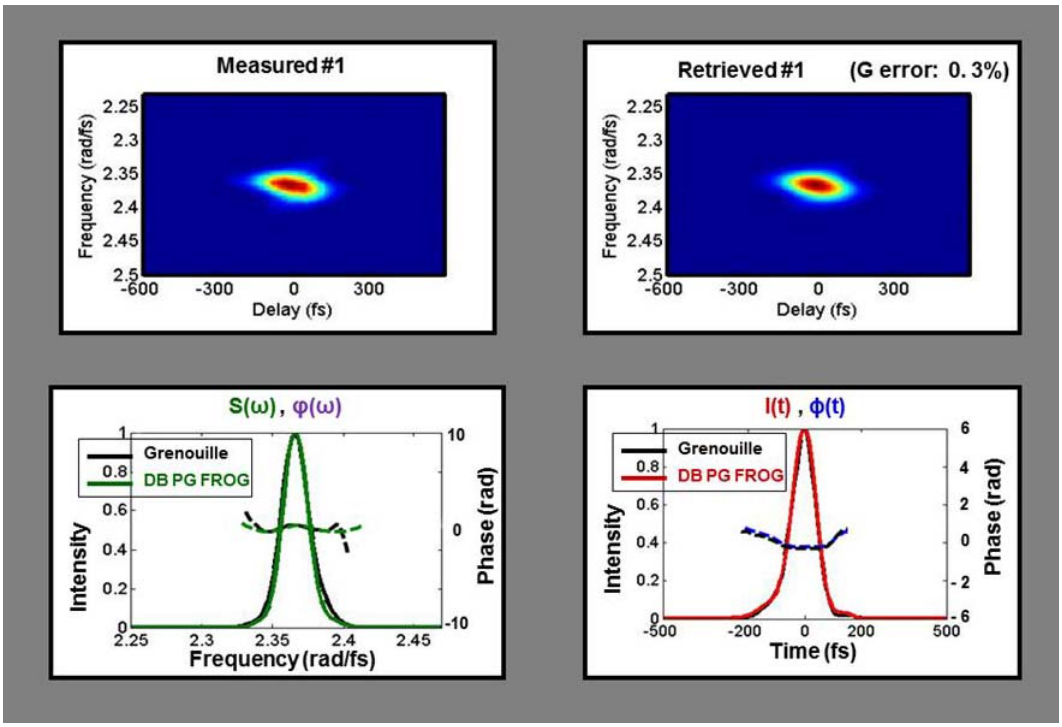

Fig.6.6. Clockwise from top left: The measured Double-Blind PG FROG trace for the less chirped pulse, the reconstructed trace, intensity and phase in time, and the spectrum and the spectral phase for E_1.

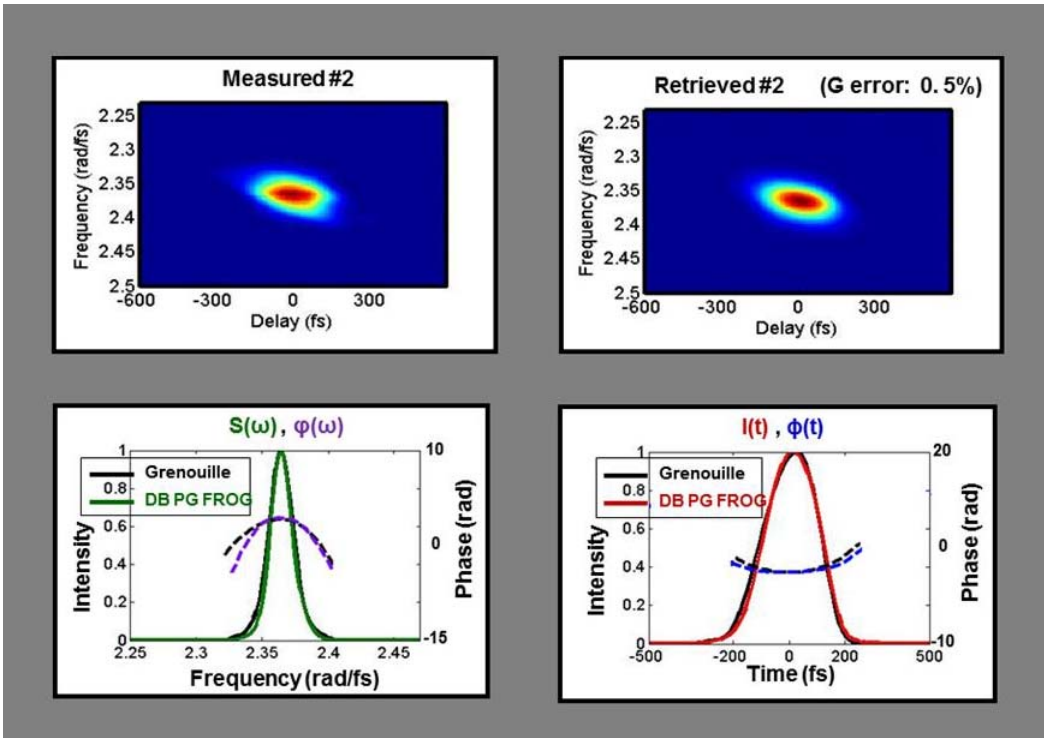

Fig.6.7. Clockwise from top left: The measured Double-Blind PG FROG trace for the chirped pulse, the reconstructed trace, intensity and phase in time, and the spectrum and the spectral phase for E_2

CHAPTER 7

DESIGN OF STABLE DISPERSION CONTROL SYSTEM FOR HIGH ENERGY CPA SYSTEMS

7.1 Introduction

The contents of this chapter focus on some of the work done in collaboration with Lockeed Martin for the development of high energy lasers. We considered various aspects of laser design, but focused mainly on the dispersion management in high energy CPA, see fig. 7.2. In order to compensate for higher order dispersion in the gain medium and maintain high energy at the output, we analyzed the use of several different hybrid stretcher/compressor systems to achieve our goals. In the later part, the possibility of using chirped volume Bragg gratings (CVBGs) for stretching and compressing the pulses was also explored, because recent developments have given hope for manufacturing of large aperture(10cm x 10cm) CVBGs . A later section describes the modeling of volume Bragg gratings to work out the design parameters for different operating wavelengths, bandwidths, and pulse energies. In the last part, we found that accumulated B-integral in the Bragg grating can be used for long range focusing of high energy beams with large modal area.

7.2 Stretching pulses up to a few nanoseconds

Grating based stretchers are commonly used in CPA. For designing a CPA to produce even higher pulse energies, it is required to stretch a pulse to a few nanoseconds.

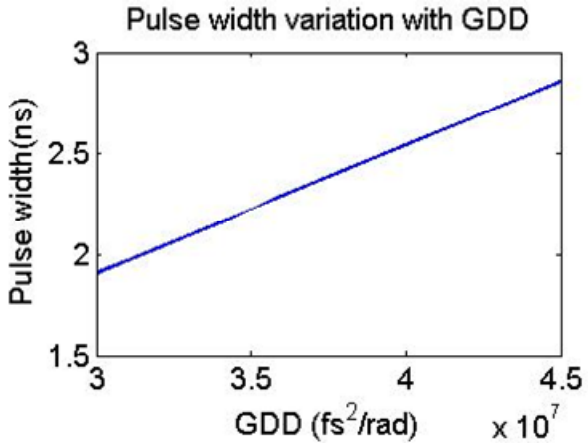

Fig 7.1 Pulse width variation with GDD.

For stretching transform limited pulses with 50 nm bandwidth to a few nanoseconds, see fig. 7.1, very large amounts of GDD is required. The grating compressors required to add the amounts of GDD in this range are large in size too. They use large gratings (can be up to 1 meter wide), with high line density (in this context ~ 1480 lines/mm to 2000 lines/mm), and large grating separations (2 – 2.5 meters!). However, with careful alignment we should be able to cancel the effect of a stretcher completely by the compressor.

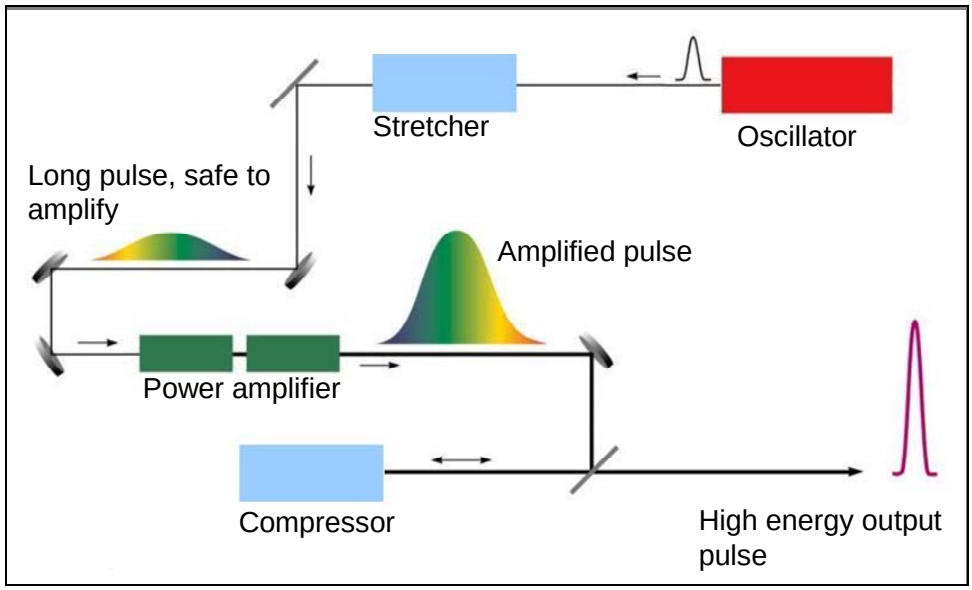

Fig. 7.2: A chirped pulse amplification system showing the three stages of the process: stretching, amplification, and compression.

If the gratings in the stretcher and compressor are kept at identical separation and the beam is aligned into them at identical angles, the dispersion introduced by the stretcher can be completely removed by the compressor. However, the GDD and TOD picked up by the pulse from the gain medium (or transmission through any other dispersive medium) during the amplification step remains uncompensated and this causes the output pulse to be longer. This problem can be addressed, at least for GDD, by using a mismatched separation between the gratings in the stretcher and the compressor. For higher order dispersion, we would like to use grism based compressors, but for high energy beams with ~100 mJ pulse energy for ~50fs pulses, no material can be used in the compression stage to avoid nonlinear damage to the material from the beam. So in the final stage of high energy CPA, we use reflection grating compressors only.

7.2.1 Three bounce compressor

The efficiency of the grating compressor depends on the diffraction efficiency of the gratings and the absorption losses suffered upon each bounce of the pulse off the grating. It is important to have high efficiency for the compressor because after going to great length for pulse amplification we doo not want to lose a lot of energy in the compression stage. The diffraction efficiency for each bounce can be improved to over ~98 % by using gratings which are blazed to couple maximum light into a particular diffraction order. For the absorption losses there is little that has been done so far, as in all the grating compressors the pulse undergoes four bounces off the gratings in the compression process. However, if we use a pair of gratings with different grating periods then we can design a compressor that uses three bounces instead of four to compress a pulse, and thus, has a higher efficiency.

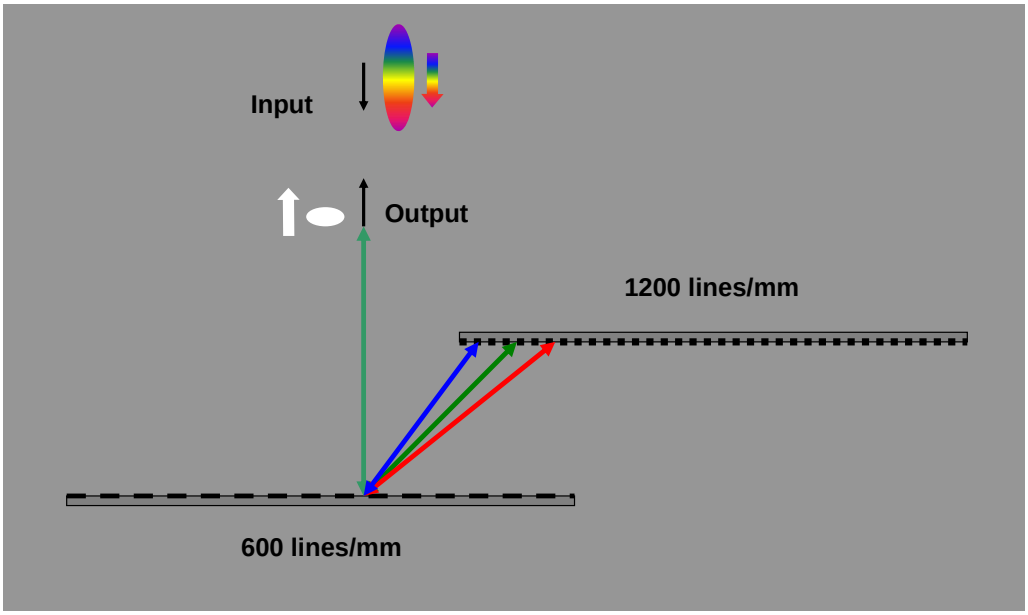

Fig. 7.3: Three bounce grating compressor.

The three bounce compressor design uses two diffraction gratings that are matched and aligned such that the input beam will travel into and out of the system along the same path, only the output is shifted slightly above (out of the plane) the input in order to facilitate beam extraction. The first grating in the beam has twice the grating period of the second grating, which is kept parallel to it at some distance. In this arrangement the first diffracted order from the first grating is reflected back along the same direction from the second grating (see fig. 7.3, notice the bi-directional colored arrows). The working principle can be understood from the following two equations. The grating equation for the first grating is given by eq. 7.1

$$\cos\psi_{d_1} - \cos\psi_{i_1} = \lambda / d \tag{7.1}$$

And the grating equation for the second grating which has half the period of the first one is given by eq. 7.2

$$\cos\psi_{d_2} - \cos\psi_{i_2} = -2\lambda / d \tag{7.2}$$

When the gratings are parallel and the beam has normal incidence on to the first grating, $\psi_{i_1} = 90^0, \psi_{d_1} = \psi_{i_2}$, substituting these in the above two equations give $\psi_{d_2} = \pi - \psi_{d_1}$ Therefore, the second grating sends the beam back in the same direction, so the output beam is overlapped with the input beam. There are no spatio-temporal distortions in the output, the Kostenbauder matrix for the compressor, eq. 7.3, confirms it (notice all the elements that correspond to spatiotemporal distortions are zero), and the compressor is easy to align. We used this compressor to generate long pulses measured by MUD TADPOLE in[31]

$$K = \begin{bmatrix} -1 & \dfrac{-2L}{\sin^2 \psi_d} & 0 & 0 \\ 0 & -1 & 0 & 0 \\ 0 & 0 & 1 & \dfrac{-2L\cos^2 \psi_d}{cf_0 \sin^2 \psi_d} \\ 0 & 0 & 0 & 1 \end{bmatrix} \tag{7.3}$$

7.2.2 Grism based stretcher

A grism based compressor can solve the problem of TOD compensation, as explained in chapter 3, but the high energy pulse at the output can cause damage to the grism material. The pulse will under go self phase modulation and accumulate high B-integrals. So we cannot use a grism compressor at the output. Using a grism stretcher and precompensating for the GDD and TOD introduced by the gain medium should solve this problem. We proposed a grism stretcher design that uses a single grism and quadruple passes it, and therefore should be auto-aligned for zero spatio-temporal distortions, fig. 7.4. It uses a cylindrical achromatic lens doublet (to avoid spatial and chromatic aberrations introduced by the lens), and can add tunable amount of TOD and GDD.

The beam after the first pass through the grism is reflected back onto it using a roof mirror as shown in fig. 7.4. A cylindrical lens is placed between the grism and roof mirror at a precise distance from the roof mirror such that the pulse travels a distance ,$2f$, before returning back to the lens after going through the roof mirror, where, f, is the focal length of the cylindrical lens. The lens and the roof mirror are mounted together on a translation stage maintaining the above mentioned separation. To tune the GDD the lens-roof mirror assembly is translated closer to or farther from the grism (the dashed square

highlights the assembly in fig. 7.4). The distance of the grism from the cylindrical lens also determines the sign of the GDD added by this stretcher. If separation between the grism and the lens is more than the focal length, *f*, then the GDD is positive, zero when the grism is at the front focal plane of the lens, and negative when the distance between the grism and the lens is less than the focal length of the lens. For tuning the TOD-to-GDD ratio, the angle of incidence of the beam into the compressor can be tuned.

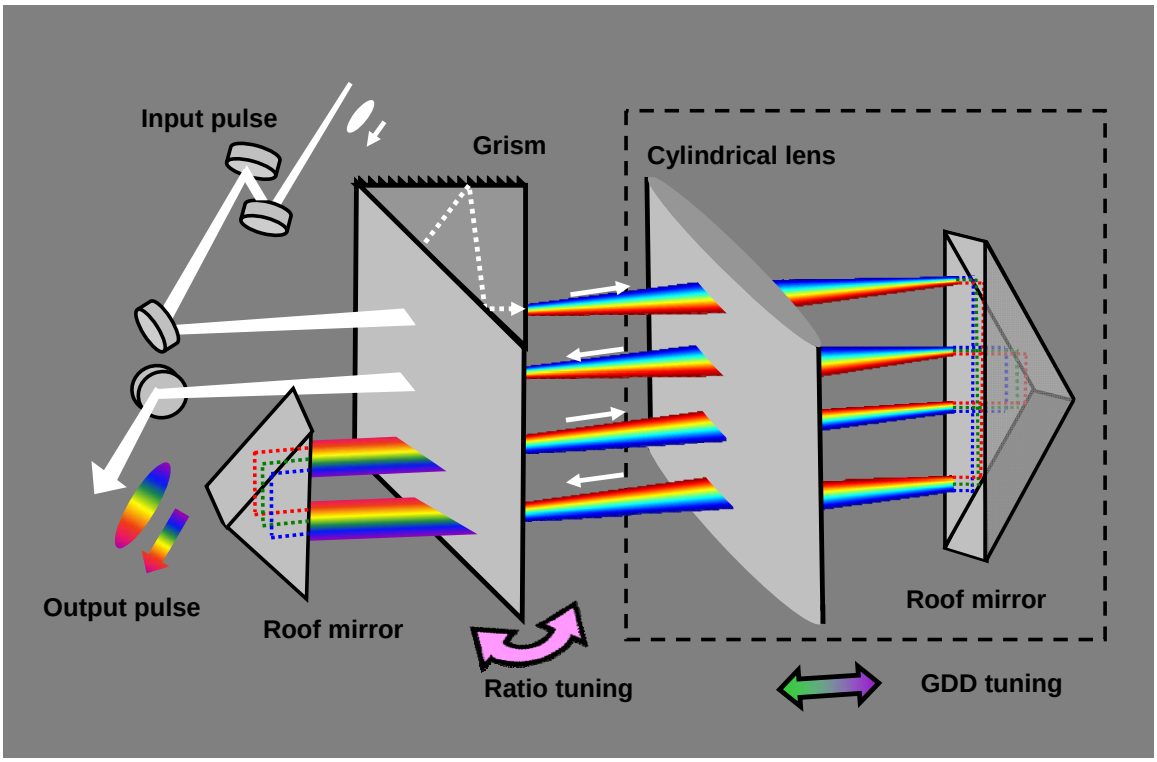

Fig. 7.4: Single grism pulse stretcher.

We worked out a few different hybrid stretcher systems, which can precompensate for the GDD and TOD introduced by both the gain medium, and the grating compressor in the last stage. We used 500 meters of optical fiber in conjunction with the grating stretcher (with a 2000 lines/mm grating) to stretch the pulses before amplification, and were able to optimize the parameters such that the stretcher could

remove both TOD and GDD after the compression in the grating compressor (with a 1480 lines/mm grating). Another solution that we found was to use a grism *compressor* with a 1000 meter long quartz fiber to *stretch* the pulses. In this system, the grism is tuned to give a large positive TOD-to-GDD ratio of > 10. The net result of fiber and the grism compressor is a pulse that was stretched by positive GDD and negative TOD. The parameters in the stretcher are varied such that the pulse after the amplification stage still has positive GDD and negative TOD in a ratio that matches that of the grating compressor.

7.3 Chirped volume Bragg gratings

Chirped volume Bragg gratings can provide the most compact systems possible for stretchers/compressors. Volume Bragg gratings (VBG) have proven useful as high-Q wavelength filters, in distributed feedback lasers, and as compressors and stretchers for ultrashort pulses. A VBG has periodically varying refractive index in a rectangular block of glass. The medium used for VBG is a photo thermo refractive glass (PTR) glass, which is basically fused silica, but is also doped with additional dopants added to give it the desired thermo-refractive properties. The fiber Bragg gratings have been around for quite some time and have been very successful in fiber optics. For VBGs, on the other hand, the requisite technology for manufacturing them correctly was developed only recently, and there is still work being done to advance these efforts[44, 93]. The challenging problem in the manufacturing of VBG is that the clear aperture in VBGs is much bigger than the FBGs (so that VBGs can support much larger spatial modes). It was difficult earlier to precisely create the index modulation uniformly across the entire cross

section, one primary reason for which was the limited penetration depths for the UV light in glass. But now researchers have been able to demonstrate working VBGs with 3-5 mm of clear aperture. To manufacture a CVBG, a PTR glass block of the right dimensions is heated up to 350 degree centigrade. Two large counter propagating beams of UV light illuminate the glass block from both ends. One of the beams is well collimated and the other beam has diverging wave fronts. This causes the spatial fringes to form in the entire region where the beams overlap, and also, the fringe periodicity varies linearly along the longitudinal axis of the glass substrate. This gives rise to a modulation of refractive index in the glass substrate, which also has a linearly varying periodicity from one end to the other of the glass substrate. Upon cooling, thus written pattern freezes in the glass substrate.

To determine the suitable parameters we modeled the VBGs using the transfer matrix method, and we also used the method of single expression (MSE) for modeling the Bragg gratings.

7.3.1 Method of single expression

The method of single expression uses numerical integration to find the solution to Helmholtz equation inside and outside the VBG. In this method, the Helmholtz equation is parameterized and reformulated as four coupled *linear* differential equations. The integration of these equations can provide the complete electric field at each point in the periodic medium, and the power flow density. The phase of the solution field can be differentiated w.r.t. wavelength to obtain time delay spectra, which gives the pulse widths

of the output from the chirped volume Bragg gratings. In this method, the solution to the wave equation is assumed to be of the form

$$E(z,t) = A(z)\cos(\omega t - S(z)) \tag{7.4}$$

Where A(z) is the amplitude of the field and 'S(z)' is the phase of the field inside the Bragg grating. For the general case of any periodic medium the above solution is substituted in the Helmholtz equation with the z-dependent permittivity term, given by eq. 7.5, the imaginary part of the complex permittivity corresponds to the gain or absorption in the Bragg grating, and the real part of the permittivity is given by eq. 7.6,

$$\varepsilon(z) = \varepsilon'(z) + i\varepsilon''(z) \tag{7.5}$$

$$\varepsilon'(z) = \varepsilon'\left(1 + U(z)\cdot M \cdot \sin\left(2\pi \frac{z}{\Lambda(z)}\right)\right) \tag{7.6}$$

Where 'U' is the apodization function, 'M' is the modulation strength and Λ(z) is the grating period. The details of the method can be found in the original article[94]. In this simulation, the effect on the output can be studied by varying modulation strength, detuning from the Bragg wavelength, gain or absorption in the medium, and the chirp parameter.

Volume Bragg grating with the fixed period

The results from a Bragg grating for 1500nm wavelength light are shown in this section fig.7.5. The medium is taken as fused silica with refractive index (R.I.) of 1.44 at 1.5 um. The grating considered is 300 grating periods long which corresponds to a length

of 0.162 mm. The modulation strength or the amplitude of the R.I. variation is taken as 0.01 (which is very close to the actual value in the Bragg gratings).

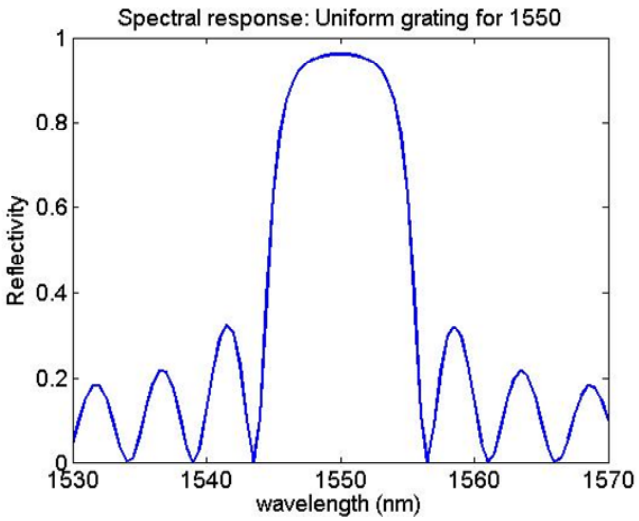

Fig. 7.5: Spectral response of a uniform grating.

Chirped Bragg grating

For modeling a chirped grating, a chirp parameter 'α' is introduced. The grating can be divided into 'N' number of grating periods which vary linearly from the input face of the grating to the back face. The grating period is determined from the wavelength of incident light in free space that satisfies Bragg condition inside the grating medium, $\Lambda = \frac{\lambda}{2n_0}$. In a chirped Bragg grating the grating period varies linearly, and during the integration of differential equations, the program determines what the grating period is at a particular z-location. For a chirped grating the grating period varies as

$$\Lambda_k = \Lambda_{\min} + \left(\frac{\Lambda_{\max} - \Lambda_{\min}}{N} \right) k \quad \text{and } k = 0,1,2...N \tag{7.7}$$

And the chirp parameter is given by $\alpha = \frac{\Lambda_{\max} - \Lambda_{\min}}{N}$. The time delay introduced by the grating is directly proportional to the grating length, which depends on the number of grating periods N. Therefore, for a given time delay, α determines the width of the spectral response. The power spectrum reflected back from the grating also depends on the amplitude of the R.I. modulation, M. These parameters are varied till we get the desired output from the grating, and at that point, the values of these parameters give the design parameters for the grating.

Correction of ringing in spectral response

To suppress the ringing in the spectral response an apodization function is used. The purpose of using apodization is to reduce the modulation amplitude gradually toward the two ends of the grating. Commonly used apodization functions are Gaussian apodization and the raised cosine apodization. The figure below (fig. 7.6) shows the grating response after including a Gaussian apodization and it also includes the absorption in the grating

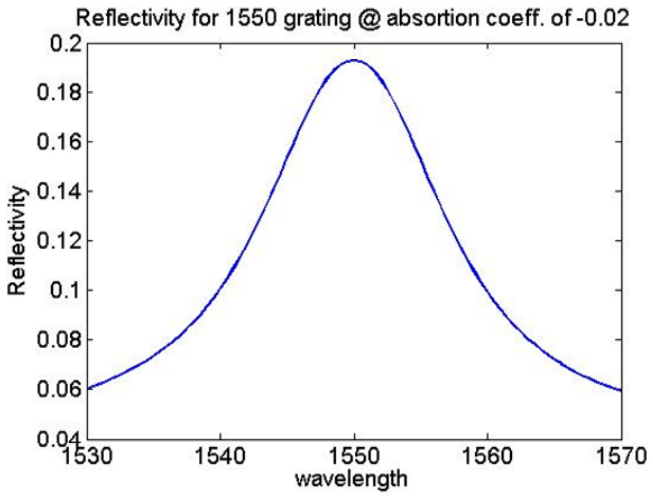

Fig. 7.6: The absence of ringing in a Gaussian apodized grating

Limitations

This model is quite useful as it allows varying the design parameters of the grating directly in the simulations. However, as the grating length is increased, the step-size-induced errors become more and more detrimental for the integration module of the program. So we had to use Runge-Kutta fourth and fifth order routines for the numerical integration and reduce the step size for the stability of the integration routine. This makes this method very time consuming, and therefore unfit for our application. However, we borrowed certain features from it and used them to define parameters in the transfer matrix method discussed below.

7.3.2 Transfer matrix method:

The Transfer Matrix Method is a commonly used technique to model Bragg gratings for time delay and spectral analyses. The couple wave theory decomposes the

Helmholtz equation inside the Bragg grating into two coupled, linear differential equations by assuming that the solution inside the periodic medium can be written as a sum of forward and backward propagating modes[95]. The grating periodicity, and the modulation amplitude, causes the coupling of the energy between the two contra-directional propagating modes in the grating medium. One method of obtaining solutions to the coupled wave equations is by direct numerical integration using Riccati differential equations, but this method faces the same problems due to numerical integration, as the method of single expression. The coupled wave equations can also be solved by the transfer matrix method[95], which is the method we used in the rest of this work, in this method the grating is divided into N parts and each has a constant grating period for it. Each part of the grating can be represented by a two dimensional transfer matrix which relates the input field and its slope before the section to the output field and slope on the other side. The basic coupled waves for a uniform grating with a gain 'g' are given by

$$\frac{dA}{dz} = \kappa \exp\left[i(2\Delta\beta z - \phi)\right] B + g A \tag{7.8}$$

$$\frac{dB}{dz} = \kappa \exp\left[-i(2\Delta\beta z - \phi)\right] A - g B \tag{7.9}$$

Where $\Delta\beta = \beta - \frac{\pi}{\Lambda}$ is the difference in the propagation constant and the Bragg frequency. A and B are the complex amplitudes of the forward and backward propagating waves. These two equations lead to the transfer matrix for this grating. The transfer matrix for the entire grating can be obtained by multiplication of the transfer matrices for each individual section of the grating. To model chirped volume Bragg grating using this

method, the grating is divided into N different sections. Each section has a different grating period and is exactly one grating period long. Multiplying together the matrices for all the sections gives the output transfer matrix, F. The reflection coefficient is given by $r = \frac{F_{21}}{F_{11}}$ and the phase of the reflected wavelength is given by $\phi_\lambda = A\mathrm{rg}(r)$. Using this method we modeled the reflectivity for a VBG (operating center wavelength of 1550 nm) with a constant period (see fig. 7.7), and a chirped volume Bragg grating (see fig. 7.8).

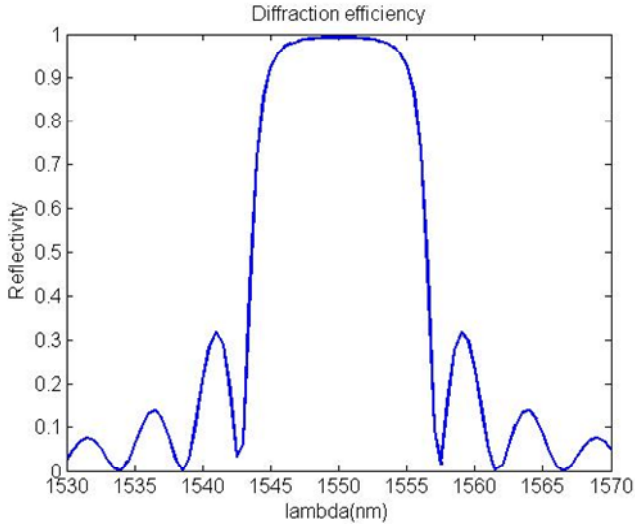

Fig. 7.7: The reflectivity spectrum of a constant period grating.

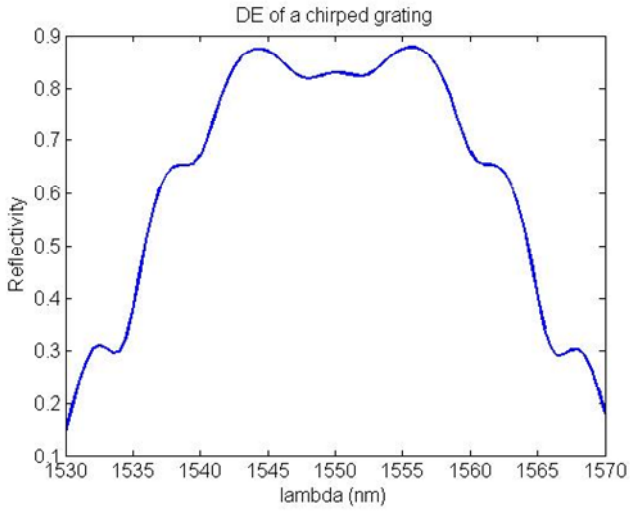

Fig. 7.8: The reflectivity spectrum of a CVBG.

Group-delay ripple correction through apodization

The group delay is obtained by taking derivative of the phase with respect to wavelength. For Gaussian spectra, one third of the total group delay equals the FWHM pulse width for the output pulse from the CVBG. The apodization is needed in CVBGs also, although the effect is negligible in the spectral response but the group delay has characteristic ripples or fluctuations which can be minimized by the use of apodization in CVBGs. The two figures below show the group delay ripple correction by apodizing the gratings. The simulation results shown are for a grating of length L with 3nm FWHM spectral response centered at 800nm. Use of Gaussian apodization, eq. 7.10 reduced the ripples in group-delay plot (see fig. 7.9).

$$U(z) = e^{-\left[(z - L/2)^2 / \alpha L^2\right]} \tag{7.10}$$

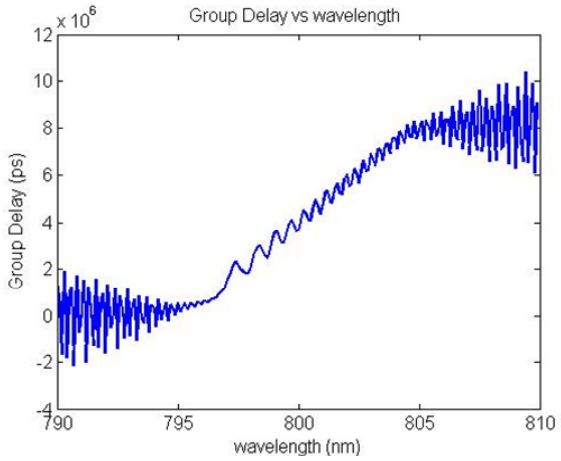

Fig. 7.9: Group-delay has reduced amplitude of oscillations after Gaussian apodization

And a raised cosine apodization, eq. 7.11 resulted in the group delay shown in the figure below (fig. 7.10).

$$U(z) = \alpha_0 \left[1 + \cos(\pi(z - ½)/L\right] \tag{7.11}$$

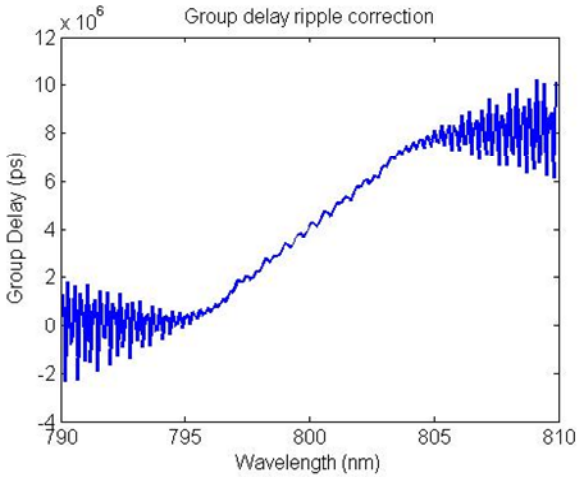

Fig. 7.10: Group-delay has much less ripples after raised cosine apodization.

CVBG for a 1ns output

Using the transfer matrix method the design parameters for a CVBG that can stretch a pulse to a FWHM of 1 nanosecond were determined. The input pulse is a transform limited pulse with 36 nm of spectral bandwidth and is centered at 1550nm. The input spectrum (in red) and the spectral response of the grating are shown in the plot below (fig. 7.11).

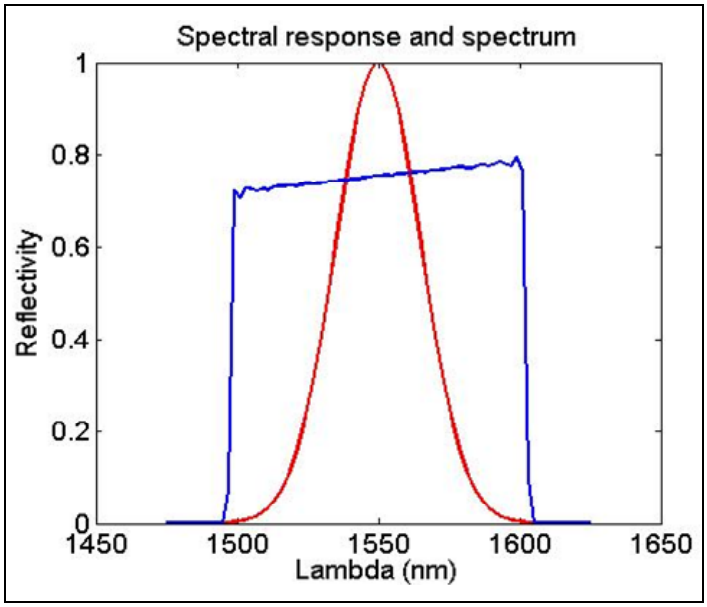

Fig. 7.11: The spectral response of the CVBG that can stretch a ~30 fs long pulse to 1 ns. The red plot shows the spectrum of the input pulse and the blue plot is the gratings reflectivity at each wavelength. The reflectivity can be increased by using a higher value for index modulation amplitude.

Gaussian apodization was used in this calculation and the resulting modulation amplitude at each z-position inside the grating is plotted below in fig. 7.12.

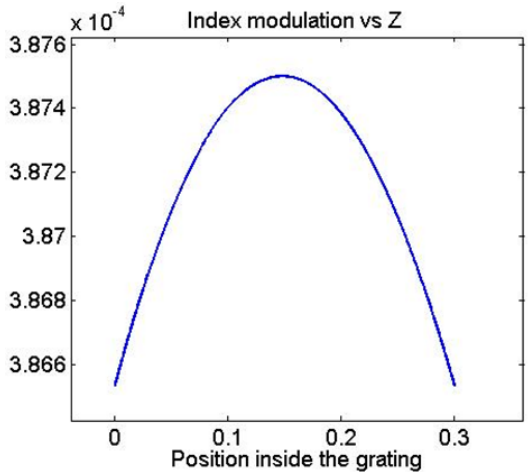

Fig. 7.12: R.I. modulation amplitude with position inside the grating, on using a Gaussian apodization, the amplitude decreases towards the grating ends.

The grating parameters were determined to be: Chirp parameter, α = 0.034, Number of grating periods, N = 580640, and the total grating length = 30cm R.I. modulation amplitude, M = 3.875 x 10^{-4}

7.4 The effect of B-integral on CVBG output

In this calculation, we consider a CVBG of a clear aperture of 10cm x 10 cm and calculate the local b-integral accumulated in the beam at each point on the beam's spatial profile. The b-integral is calculated using the following equation

$$Bint(x,y) = \frac{2\pi n_2 I_0(x,y) L}{\lambda} \tag{2.5}$$

Where n_2 is the nonlinear coefficient, $I_0(x,y)$ is the peak intensity of the pulse at each position in the beam, λ is picked as the minimum wavelength in the pulse spectrum (for the worst case analysis), and L in the grating length. During the final pass, pulse width decreases linearly inside the grating, which can be accounted for in the simulations. We

also assumed that the pulse energy decreases linearly inside the grating due to scattering losses, and up to 50% of the input energy is lost up to the output. The pulse energies chosen for the simulations were such that they would allow a maximum b-integral of up to ~5 radians. One such calculation where the b-integral varies with the radial position in a Gaussian beam is shown in the figure below (fig. 7.13). The output pulse energy is 77 mJ and the output pulse duration is 50 fs, centered at 1550 nm (the stretched and amplified pulse duration is 1ns).

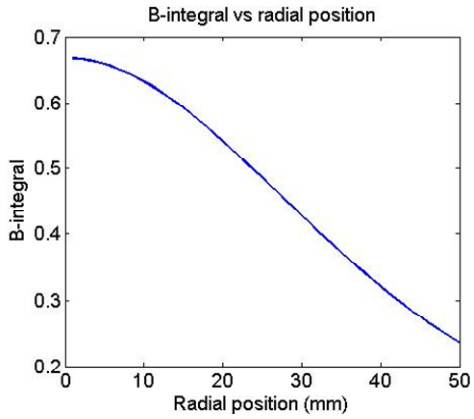

Fig. 7.13: The B-integral variation with the position in the output beam. The more intense center of the Gaussian beam induces more nonlinear R.I. therefore the positions toward the beam center accumulate higher b-integral

The variation in the value of b-integral across the beam cross-section can add a lens-like phase and cause the beam to focus at large distances. We used Fresnel propagation to propagate a beam down range and study the effect on the beam spot size. A well collimated Gaussian beam at the output of the CVBG diverges on propagation, but if it has the nonlinear phase added to it, then the beam spot goes through a minimum after propagating some distance. The location of the focal plane of this 'lens' and the beam spot size at focus can be controlled by changing the input spot size and the pulse energy both. In the figure below the input beam diameter is same for the two 1ps long

pulses but they have different pulse energies, so they accumulate different b-integrals. The maximum value of the b-integral at the beam center is 0.76 radians and 2.3 radians respectively. In the first case, the beam focuses to a spot of 49.44 mm (FWHM) at a distance of 2150 meters, see fig. 7.14. In the second case, the beam focuses to a spot of 31.84 mm (FWHM) width at a distance of 1600 meters from the source. The b-integral is different for different wavelengths in the pulse bandwidth, so this inherently introduces chromatic aberration, which is not significant for the cases with relatively lower bandwidths (for example: 1ps output pulses)

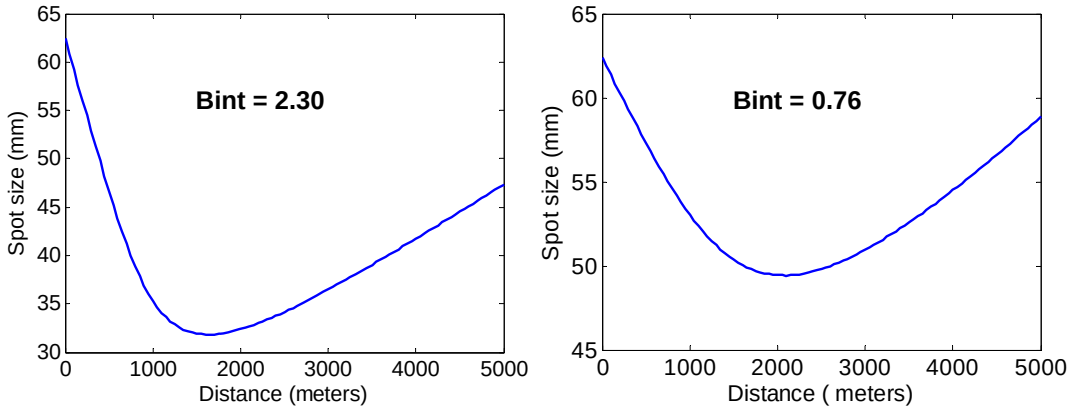

Fig. 7.14: The figure shows the FWHM spot of the collimated output beam from the Bragg grating as it propagates. The beams initially have ~62mm spot size, and then the nonlinear phase added due to the b-integral, causes the beams to focus. The beam with the lower maximum b-integral of 0.76 (B-int = 0.76 radians) focuses at a longer distance and has a larger focal spot size of ~49mm. The beam with the higher maximum b-integral of 2.3 (B-int = 2.3 radians) focuses at a shorter distance and has the smaller focal spot size of ~32mm.

REFERENCES

[1]. C. B. Schaffer, A. Brodeur, J. F. García, and E. Mazur, "Micromachining bulk glass by use of femtosecond laser pulses with nanojoule energy," Opt. Lett. **26**, 93-95 (2001).

[2]. R. R. Gattass and E. Mazur, "Femtosecond laser micromachining in transparent materials," Nat Photon **2**, 219-225 (2008).

[3]. B. N. Chichkov, C. Momma, S. Nolte, F. vonAlvensleben, and A. Tunnermann, "Femtosecond, picosecond and nanosecond laser ablation of solids," Appl Phys A-Mater **63**, 109-115 (1996).

[4]. E. G. Gamaly, A. V. Rode, B. Luther-Davies, and V. T. Tikhonchuk, "Ablation of solids by femtosecond lasers: Ablation mechanism and ablation thresholds for metals and dielectrics," Phys. Plasmas **9**, 949-957 (2002).

[5]. T. Brixner and G. Gerber, "Femtosecond polarization pulse shaping," Opt. Lett. **26**, 557-559 (2001).

[6]. T. Brixner, N. H. Damrauer, G. Krampert, P. Niklaus, and G. Gerber, "Adaptive shaping of femtosecond polarization profiles," J. Opt. Soc. Am. B **20**, 878-881 (2003).

[7]. M. Plewicki, F. Weise, S. M. Weber, and A. Lindinger, "Phase, amplitude, and polarization shaping with a pulse shaper in a Mach-Zehnder interferometer," Appl. Opt. **45**, 8354-8359 (2006).

[8]. A. Assion, T. Baumert, M. Bergt, T. Brixner, B. Kiefer, V. Seyfried, M. Strehle, and G. Gerber, "Control of Chemical Reactions by Feedback-Optimized Phase-Shaped Femtosecond Laser Pulses," Science **282**, 919-922 (1998).

[9]. I. Pastirk, E. J. Brown, Q. Zhang, and M. Dantus, "Quantum Control of the Yield of a Chemical Reaction," J. of Chem. Phys. **108**, 4375-4378 (1998).

[10]. R. Levis, Gerahun Menkir, Herschel Rabitz, "Selective Bond Dissociation and Rearrangement with Optimally Tailored, Strong-Field Laser Pulse," Science **292**, 709-713 (2001).

[11]. W. Denk, J. Strickler, and W. Webb, "Two-photon laser scanning fluorescence microscopy," Science **248**, 73-76 (1990).

[12]. M. Fricke and T. Nielsen, "Two-dimensional imaging without scanning by multifocal multiphoton microscopy," Appl. Opt. **44**, 2984-2988 (2005).

[13]. C. L. Evans and X. S. Xie, "Coherent Anti-Stokes Raman Scattering Microscopy: Chemical Imaging for Biology and Medicine," Annual Review of Analytical Chemistry **1**, 883-909 (2008).

[14]. M. R. Hee, J. A. Izatt, J. M. Jacobson, J. G. Fujimoto, and E. A. Swanson, "Femtosecond transillumination optical coherence tomography," Optics Letters **18**, 950-952 (1993).

[15]. I. Hartl, X. D. Li, C. Chudoba, R. K. Hganta, T. H. Ko, J. G. Fujimoto, J. K. Ranka, and R. S. Windeler, "Ultrahigh-resolution optical coherence tomography using continuum generation in an air-silica microstructure optical fiber," Opt. Lett. **26**, 608-610 (2001).

[16]. G. J. Tearney, B. E. Bouma, S. A. Boppart, B. Golubovic, E. A. Swanson, and J. G. Fujimoto, "Rapid acquisition of in vivo biological images by use of optical coherence tomography," Opt. Lett. **21**, 1408-1410 (1996).

[17]. R. A. Vilson, A. B. Carlos, R. P. Roberto, L. Michal, A. F. Mark, G. O. Dimitre, and L. G. Alexander, "All-optical switch on a Silicon chip," in Technical Digest (CD) (Optical Society of America, 2004), CTuFF3.

[18]. Z. Chang, A. Rundquist, H. Wang, H. C. Kapteyn, and M. M. Murnane, "Generation of Coherent Soft-X-Rays at 2.7nm using High Harmonics," Physical Review Letters **79**, 2967 (1997).

[19]. A. Braun, G. Korn, D. Du, J. Squier, and G. Mourou, "Self-Channeling of High-Peak-Power Femtosecond Laser Pulses in Air," Opt. Lett. **20**, 73-75 (1995).

[20]. P. E. Young and P. R. Bolton, "Propagation of subpicosecond laser pulses through a fully ionized plasma," Physical Review Letters **77**, 4556-4559 (1996).

[21]. R. Paschotta and U. Keller, "Passive mode locking with slow saturable absorbers," Applied Physics B: Lasers and Optics **73**, 653-662 (2001).

[22]. J. D. Kafka, M. L. Watts, and J. W. J. Pieterse, "Picosecond and femtosecond pulse generation in a regeneratively mode-locked Ti:sapphire laser," Quantum Electronics, IEEE Journal of **28**, 2151-2162 (1992).

[23]. J. Herrmann, "Theory of Kerr-lens mode locking: role of self-focusing and radially varying gain," J. Opt. Soc. Am. B **11**, 498-512 (1994).

[24]. K. W. DeLong, R. Trebino, J. Hunter, and W. E. White, "Frequency-resolved optical gating with the use of second-harmonic generation," J. Opt. Soc. Am. B **11**, 2206-2215 (1994).

[25]. S. Akturk, M. Kimmel, P. O'Shea, and R. Trebino, "Extremely simple device for measuring 20-fs pulses," Opt. Lett. **29**, 1025-1027 (2004).

[26]. K. W. DeLong, R. Trebino, and D. J. Kane, "Comparison of ultrashort-pulse frequency-resolved-optical-gating traces for three common beam geometries," J. Opt. Soc. Am. B **11**, 1595-1608 (1994).

[27]. M. Takeda, H. Ina, and S. Kobayashi, "Fourier-transform method of fringe-pattern analysis for computer-based topography and interferometry," J. Opt. Soc. Am. **72**, 156-160 (1982).

[28]. C. Dorrer, N. Belabas, J.-P. Likforman, and M. Joffre, "Spectral resolution and sampling issues in Fourier-transform spectral interferometry," J. Opt. Soc. Am. B **17**, 1795-1802 (2000).

[29]. P. Bowlan, P. Gabolde, A. Schreenath, K. McGresham, and R. Trebino, "Crossed-beam spectral interferometry: a simple, high-spectral-resolution method for completely characterizing complex ultrashort pulses in real time," Optics Express **14**, 11892-11900 (2006).

[30]. P. Bowlan, P. Gabolde, M. A. Coughlan, R. Trebino, and R. J. Levis, "Measuring the spatiotemporal electric field of ultrashort pulses with high spatial and spectral resolution," J. Opt. Soc. Am. B **25**, A81-A92 (2008).

[31]. J. Cohen, P. Bowlan, V. Chauhan, and R. Trebino, "Measuring temporally complex ultrashort pulses using multiple-delay crossed-beam spectral interferometry," Opt. Express **18**, 6583-6597 (2010).

[32]. C. Iaconis and I. A. Walmsley, "Spectral phase interferometry for direct electric-field reconstruction of ultrashort optical pulses," Opt. Lett. **23**, 792-794 (1998).

[33]. C. Dorrer and I. A. Walmsley, "Accuracy criterion for ultrashort pulse characterization techniques: application to spectral phase interferometry for direct electric field reconstruction," J. Opt. Soc. Am. B **19**, 1019-1029 (2002).

[34]. M. Hirasawa, N. Nakagawa, K. Yamamoto, R. Morita, H. Shigekawa, and M. Yamashita, "Sensitivity improvement of spectral phase interferometry for direct electric-field reconstruction for the characterization of low-intensity femtosecond pulses," Applied Physics B: Lasers and Optics **74**, s225-s229 (2002).

[35]. P. Bowlan, P. Gabolde, and R. Trebino, "Directly Measuring the Spatio-Temporal Electric Field of Ultrashort Pulses in and near a Focus," in OSA Technical Digest Series (CD) (Optical Society of America, 2007), CFO3.

[36]. A. E. Siegman, "Defining, measuring, and optimizing laser beam quality," in (SPIE, 1993), 2-12.

[37]. V. R. Supradeepa, E. L. Daniel, and M. W. Andrew, "Fourier Pulse Shaping with Enhanced Spectral Control Using a 2-D VIPA Grating Pulse Shaper," in OSA Technical Digest (CD) (Optical Society of America, 2008), CThDD6.

[38]. F. Verluise, V. Laude, Z. Cheng, C. Spielmann, and P. Tournois, "Amplitude and phase control of ultrashort pulses by use of an acousto-optic programmable dispersive filter: pulse compression and shaping," Opt. Lett. **25**, 575-577 (2000).

[39]. J. C. Travers, J. M. Stone, A. B. Rulkov, B. A. Cumberland, A. K. George, S. V. Popov, J. C. Knight, and J. R. Taylor, "Optical pulse compression in dispersion decreasing photonic crystal fiber," Opt. Express **15**, 13203-13211 (2007).

[40]. F. Druon and P. Georges, "Pulse-compression down to 20 fs using a photonic crystal fiber seeded by a diode-pumped Yb:SYS laser at 1070 nm," Opt. Express **12**, 3383-3396 (2004).

[41]. T. V. Luat, B. L.-M. Rodrigo, P. H. Christoph, A. F. Mark, L. H. Anne, R. Thierry, and L. G. Alexander, "Optimal Pulse Compression via Sequential Filamentation," in OSA Technical Digest Series (CD) (Optical Society of America, 2007), JWE1.

[42]. M. A. Foster, R. Salem, D. F. Geraghty, A. C. Turner-Foster, M. Lipson, and A. L. Gaeta, "Silicon-chip-based ultrafast optical oscilloscope," Nature **456**, 81-84 (2008).

[43]. H. Daniel, V. Laszlo, T. Franz, S. Karl, T. Raphael, B. Alexander, P. Vladimir, and K. Ferenc, "Generation of 8 fs, 125 mJ Pulses through Optical Parametric Chirped Pulse Amplification," in OSA Technical Digest Series (CD) (Optical Society of America, 2009), WA3.

[44]. K.-H. Liao, M.-Y. Cheng, E. Flecher, V. I. Smirnov, L. B. Glebov, and A. Galvanauskas, "Large-aperture chirped volume Bragg grating based fiber CPA system," Opt. Express **15**, 4876-4882 (2007).

[45]. V. Chauhan, P. Bowlan, J. Cohen, and R. Trebino, "Single-diffraction-grating and grism pulse compressors," J. Opt. Soc. Am. B **27**, 619-624.

[46]. V. Chauhan, P. Bowlan, J. Cohen, V. Peter, and R. Trebino, "Single prism/grating pulse compressor," IEEE J. of Quant. Elect. (2010).

[47]. V. Chauhan, J. Cohen, and R. Trebino, "Simple dispersion law for arbitrary sequences of dispersive optics," Appl. Opt. (2010).

[48]. J. Paye and A. Migus, "Space time Wigner functions and their application to the analysis of a pulse shaper," J. Opt. Soc. Am. B **12**, 1480-1490 (1995).

[49]. A. G. Kostenbauder, "Ray-Pulse Matrices: A Rational Treatment for Dispersive Optical Systems," IEEE J. Quant. Electron. **26**, 1148-1157 (1990).

[50]. S. Akturk, X. Gu, P. Gabolde, and R. Trebino, "The general theory of first-order spatio-temporal distortions of Gaussian pulses and beams," Optics Express **13**, 8642-8661 (2005).

[51]. P. Gabolde, D. Lee, S. Akturk, and R. Trebino, "Describing first-order spatio-temporal distortions in ultrashort pulses using normalized parameters," Optics Express **15**, 242-251 (2007).

[52]. R. L. Fork, O. E. Martinez, and J. P. Gordon, "Negative dispersion using pairs of prisms," Optics Letters **9**, 150-152 (1984).

[53]. O. E. Martinez, J. P. Gordon, and R. L. Fork, "Negative group-velocity dispersion using refraction," J. Opt. Soc. Am. A **1**, 1003-1006 (1984).

[54]. Z. Bor and B. Racz, "Group Velocity Dispersion in Prisms and Its Application to Pulse Compression and Travelling-Wave Excitation," OC **54**, 165-170 (1985).

[55]. S. Kane and J. Squier, "Grism-pair stretcher-compressor system for simultaneous secind and third-order dispersion compensation in chirped-pulse amplification," Journal of the Optical Society of America B **14**(1997).

[56]. X. Gu, S. Akturk, and R. Trebino, "Spatial Chirp in Ultrafast Optics," Opt. Comm. **242**, 599-604 (2004).

[57]. K. Osvay, A. P. Kovacs, Z. Heiner, G. Kurdi, J. Klebniczki, and M. Csatari, "Angular dispersion and temporal change of femtosecond pulses from misaligned pulse compressors," Selected Topics in Quantum Electronics, IEEE Journal of **10**, 213-220 (2004).

[58]. S. Akturk, X. Gu, M. Kimmel, and R. Trebino, "Extremely simple single-prism ultrashort- pulse compressor," Opt. Express **14**, 10101-10108 (2006).

[59]. M. Lai, S. T. Lai, and C. Swinger, "Single-grating laser pulse stretcher and compressor," Applied Optics **33**, 6985-6987 (1994).

[60]. J. J. Field, C. G. Durfee, J. A. Squier, and S. Kane, "Quartic-phase limited grism-based ultrashort pulse shaper," Optics Letters (2007).

[61]. E. A. Gibson, D. M. Gaudiosi, H. C. Kapteyn, R. Jimenez, S. Kane, R. Huff, C. Durfee, and J. Squier, "Efficient reflection grisms for pulse compression and dispersion compensation of femtosecond pulses," Opt. Lett. **31**, 3363-3365 (2006).

[62]. P. Bowlan, P. Gabolde, A. Schreenath, K. McGresham, S. Akturk, and R. Trebino, "Spatially Resolved Spectral interferometry," in *Conference on Light and Electroptics*, 2006),

[63]. W. Dietel, J. J. Fontaine, and J. C. Diels, "Intracavity pulse compression with glass: a new method of generating pulses shorter than 60 fsec," Opt. Lett. **8**, 4-6 (1983).

[64]. R. L. Fork, C. H. B. Cruz, P. C. Becker, and C. V. Shank, "Compression of optical pulses to six femtoseconds by using cubic phase compensation," Opt. Lett. **12**, 483-485 (1987).

[65]. G. Cheriaux, P. Rousseau, F. Salin, J. P. Chambaret, B. Walker, and L. F. Dimauro, "Aberration-free stretcher design for ultrashort-pulse amplification," Opt. Lett. **21**, 414-416 (1996).

[66]. V. Chauhan, P. Bowlan, J. Cohen, and R. Trebino, "Single-grating and single-grism pulse compressors," in *Conference on Lasers and Electro-Optics/International Quantum Electronics Conference*, OSA Technical Digest (CD) (Optical Society of America, 2009), CMLL7.

[67]. V. Chauhan, J. Cohen, P. Bowlan, and R. Trebino, "single grating and grism pulse compressors," (Georgia Institute of Technology, Atlanta, 2009).

[68]. W. E. White, F. G. Patterson, R. L. Combs, D. F. Price, and R. L. Shepherd, "Compensation of higher-order frequency-dependent phase terms in chirped-pulse amplification systems," Opt. Lett. **18**, 1343-1345 (1993).

[69]. E. A. Gibson, D. M. Gaudiosi, H. C. Kapteyn, R. Jimenez, S. Kane, R. Huff, and C. G. Durfee, "Efficient reflection grisms for pulse compression and dispersion compensation of femtosecond pulses," Opt. Lett. **31**, 3363-3365 (2006).

[70]. S. Kane and J. Squier, "Grism-pair stretcher-compressor system for simultaneous second and third-order dispersion compensation in chirped-pulse amplification," Journal of the Optical Society of America B **14**(1997).

[71]. S. o. P. V. Chauhan, Georgia Institute of Technology, 837 State Street NW, Atlanta, GA 30332, J. Cohen and R. Trebino are preparing a manuscript to be called "Dispersion law for an arbitrary sequence of dispersive devices". (2010).

[72]. R. Trebino, "Achromatic N-Prism Beam Expanders: Optimal Configurations," Appl. Opt. **24**, 1130 (1985).

[73]. S. Akturk, M. Kimmel, P. O'Shea, and R. Trebino, "Extremely simple device for measurement of 20-fs pulses," in *Conference on Lasers and Electro-Optics*, 2003),

[74]. R. J. Niefer and J. B. Atkinson, "The design of achromatic prism beam expanders for pulsed dye lasers," Optics Communications **67**, 139-143 (1988).

[75]. D. C. Hanna, P. A. Kärkkäinen, and R. Wyatt, "A simple beam expander for frequency narrowing of dye lasers," Optical and Quantum Electronics **7**, 115-119 (1975).

[76]. I. Shoshan and U. P. Oppenheim, "The use of a diffraction grating as a beam expander in a dye laser cavity," Optics Communications **25**, 375-378 (1978).

[77]. F. J. Duarte, "Solid-state multiple-prism grating dye-laser oscillators," Appl. Opt. **33**, 3857-3860 (1994).

[78]. F. J. Duarte and J. A. Piper, "Prism preexpanded grazing-incidence grating cavity for pulsed dye lasers," Appl. Opt. **20**, 2113-2116 (1981).

[79]. R. L. Fork, O. E. Martinez, and J. P. Gordon, "Negative dispersion using paris of prisms," Optics Letters **9**, 150-152 (1984).

[80]. O. Martinez, "3000 times grating compressor with positive group velocity dispersion: Application to fiber compensation in 1.3-1.6 micron region," Quantum Electronics, IEEE Journal of **23**, 59-64 (1987).

[81]. F. J. Duarte and J. A. Piper, "Dispersion theory of multiple-prism beam expanders for pulsed dye lasers," Optics Communications **43**, 303-307 (1982).

[82]. F. A. Jenkins and H. E. White, *Fundamentals of Optics,* III ed. (Mc Graw Hill Book Company, 1957).

[83]. G. Chartier, *Introduction to Optics* (Springer, 2005).

[84]. M. Born and E. Wolf, *Principles of Optics,* 7 ed. (Cambridge University Press, New York, 1999).

[85]. I. R. Kenyon, *Light Fantastic* (Oxford University Press, USA, 2008), p. 640.

[86]. J. K. Robertson and *Introduction to physical optics,* III ed., University physics series (N.Y. : Van Nostrand, 1941).

[87]. G. S. Monk, *Light: Principles and Experiments,* II ed. (Dover Publications Inc., 2000).

[88]. J. R. Meyer-Arendt, *Introduction to Classical and Modern Optics,* IV ed. (Benjamin Cummings, 1994), p. 480.

[89]. R. S. Longhurst, *Geometrical and Physical Optics* III ed. (Longman Group United Kingdom, 1974), p. 677.

[90]. K. W. DeLong, R. Trebino, and W. E. White, "Simultaneous Recovery of Two Ultrashort Laser Pulses from a Single Spectrogram," J. Opt. Soc. Am. B **12**, 2463-2466 (1995).

[91]. D. J. Kane, G. Rodriguez, A. J. Taylor, and T. S. Clement, "Simultaneous measurement of two ultrashort laser pulses from a single spectrogram in a single shot," Journal of the Optical Society of America B (Optical Physics) **14**, 935-943 (1997).

[92]. R. Trebino, *Frequency-Resolved Optical Gating: The Measurement of Ultrashort Laser Pulses* (Kluwer Academic Publishers, Boston, 2002).

[93]. A. Galvanauskas, A. Heaney, T. Erdogan, and D. Harter, "Use of volume chirped Bragg gratings for compact high-energy chirped pulse amplification circuits," in *Lasers and Electro-Optics, 1998. CLEO 98. Technical Digest. Summaries of papers presented at the Conference on*, 1998), 362.

[94]. H. V. Baghdasaryan and T. M. Knyazyan, "Modelling of linearly chirped fiber Bragg gratings by the method of single expression," Optical and Quantum Electronics **34**, 481-492 (2002).

[95]. M. Yamada and K. Sakuda, "Analysis of almost-periodic distributed feedback slab waveguides via a fundamental matrix approach," Appl. Opt. **26**, 3474-3478 (1987).